SOLUTION-BASED SYNTHETIC STRATEGIES, CHARACTERIZATIONS, AND APPLICATIONS OF NANOPARTICLES

By

YI-WEI WANG

Bachelor of Science in Chemistry

Sun Yat-sen University

Guangdong, China

2013

Submitted to the Faculty of the
Graduate College of the
Oklahoma State University
in partial fulfillment of
the requirements for
the Degree of
DOCTOR OF PHILOSOPHY
May, 2019

SOLUTION-BASED SYNTHETIC STRATEGIES, CHARACTERIZATIONS, AND APPLICATIONS OF NANOPARTICLES

Dissertation Approved:

Dr. Yolanda Vasquez

Thesis Adviser

Dr. Allen Apblett

Dr. Frank Blum

Dr. Laleh Tahsini

Dr. Josh Ramsey

ACKNOWLEDGEMENTS

I would first like to express my deep gratitude to my graduate research advisor, Dr. Yolanda Vasquez, for her professional guidance and valuable support. I would also like to extend my sincere appreciation to my graduate committee members, Dr. Allen Apblett, Dr. Frank Blum, Dr. Laleh Tahsini and Dr. Josh Ramsey, for their valuable suggestions and positive feedback.

I gratefully acknowledge the help provided by Dr. Reza Latifi and Dr. Alexei Grigoriev on performing XRD tests and analyzing data. I would also like to recognize the assistance that I received from Ms. Lisa Whitworth and Mr. Brent Johnson with use of electron microscopes. Additionally, I am grateful to Dr. Qingsheng Wang and Prof. Rob Agnew for their useful and constructive recommendations on carrying out flame retardancy tests and data analysis.

I wish to thank my fellow labmates with whom I have had the pleasure to work, Dr. Deshani Fernando, Dr. Hasani Jayasinghe, Dr. Ujith Madduma Bandarage, Mrs. Menuka Adhikari, and Ms. Shoukath Sulthana for lab technical training, stimulating discussions, kind encouragement and company, and all the fun we have had in the last few years.

I must express my very profound gratitude to my parents, my grandparents, and my fiancée, Ben Champlin for providing me with great patience, continuous love and unfailing support throughout the process of researching and writing this dissertation.

Lastly, I would like to give special thank to Tom W. Hiddleston, a high profile British actor with an excellent education background. During the process of writing this dissertation, his works and performance have always been able to ease my stress and depression; his working attitude and professional dedication have always inspired me to overcome difficulties and keep challenging myself in many ways.

Name: YI-WEI WANG

Date of Degree: MAY, 2O19

Title of Study: SOLUTION-BASED SYNTHETIC STRATEGIES, CHARACTERIZATIONS, AND APPLICATIONS OF NANOPARTICLES

Major Field: Chemistry

Abstract:

Nanomaterials have attracted great attention in the past decades due to their unique properties. Up to the present time, various nanoparticles with tunable size and shape have been produced using solution-based synthetic methods. The highly diversified sizes and shapes make nanoparticles suitable for a wide range of applications. The following chapters will focus on solution-based synthesis and conversion of metal nanoparticles and semiconductor nanoparticles. Fabrication of ZnO and ZnO/ZnS nanorods coated cotton fabrics will be introduced, and their promising flame retardant properties will also be presented. In addition to direct synthesis, shape-controllable conversion of nanoscaled Zn_3P_2 to ZnS and gold nanorods to Au_3Ni intermetallic nanorods will be demonstrated.

TABLE OF CONTENTS

Chapter Page

LIST OF TABLES

LIST OF FIGURES

Page

CHAPTER I

SOLUTION-BASED SYNTHESIS, CHARARTERIZATION, AND APPLICATIONS OF NANOMATERIALS

Introduction

The concept "nanotechnology and nanomaterials" was firstly predicted by Feynman in 1959.[1] Solid materials can be confined to an extremely small dimension and these "small materials" may possess interesting properties.[2] In 1980s, electron microscopy techniques were invented that provided reliable tools that allowed direct human observation and manipulation of atoms.[3-4] Since then, the pace of development of nanotechnology has been significantly accelerated and a great number of studies were carried out.[5-7] Nanomaterials are considered the foundation of nanotechnology and have been a hot topic since the beginning of 21 century.[8-12] According to the most widely accepted definition provided by the Nanocale Sciences, Engineering and Technology (NSET) group in 2000, materials with dimensions ranging from 1-100 nm that possess unique features and functionalities, which differ from their bulk analogies are identified as nanomaterials.[13-15]

Semiconductor nanoparticles are classic examples of nanomaterials. They have been playing an increasingly important role and widely investigated in the past few decades due to the unique band gap.[16] Transition metal oxides (TMOs) are an important semiconductors and have drawn considerable attention due to the abundance in the earth's crust of these materials as well as their size- dependent optical and electrical properties and multi-functionality suitable for diverse applications.[17-18] ZnO, one of the most well-studied transition metal oxide, is classified as a group II-IV semiconductor with a large band gap (3.4 eV), high bond energy (60 meV) and high chemical and mechanical stability.[19] So far, ZnO nanomaterials can be obtained in one- (1D), two- (2D), and three- (3D) dimensional structures.[20] One- dimensional (1D) structures include nanorods, nanobelts, nanowires, nanoneedles, etc. Two- dimensional (2D) ZnO nanomaterials could have shapes of sheets and plates. ZnO can also be generated in three- dimensional (3D) structures such as nanofilms and nanoflowers. To grow ZnO nanomaterials with different morphologies, various synthetic procedures were established.[21] The sol-gel method[22] and hydrothermal method[23] are both widely used to synthesize ZnO nanoparticles, due to low cost, simplicity, ease of scaling, and high degree of crystallinity of the products.[24] Another popular method is controlled precipitation, which requires the presence of a surfactant and can be done at room temperature.[25] In addition, ZnO nanoparticles can be further modified to improve chemical and physical properties that could be crucial for certain applications. For example, ZnO nanoparticles (core) can be coated by materials with larger band gaps (shell) such as ZnS, CdS, and TiO_2, to generate core/shell structures.[26-27] Its piezo-, pyro-, and optical-electric properties make ZnO a multifunctional material that can be used as sensors,[28] energy convertors and generators,[29] and catalysts.[30] The high biocompatibility and biodegradability along with low toxicity give ZnO potential to

be used in the biomedical field.[31] Besides, the low heat conductivity and high thermal stability of ZnO also make it a great candidate for flame retardant coatings. In recent years, ZnO has been coupled with other organic flame retardant materials and used as coatings on fabrics surface to improve flame retardancy. In chapter 2, we report a unique multi-step hydrothermal method to grow ZnO nanorods on the surface of cotton fabrics. ZnO/ZnS core/shell nanorods were obtained after a sulfidation. A cone calorimeter was used to test the flame retardancy of the coatings. The results show significant reduction on heat and smoke release and suppression of flame growth and spreading.

Transition metal chalcogenides (MX) are another widely studied class of semiconductors, which consists of d-transition metals (M = Fe, Co, Zn, etc), and chalcogen atoms (X = S, Se).[32] ZnS is a typical example. It has a large band gap: 3.72 eV for the cubic (zinc blende) structure and 3.77 eV for the hexagonal (wurtzite) structure, which make it an excellent candidate for visible-blind ultraviolet (UV) light based optoelectronics or electroluminescence devices, such as light-emitting diodes (LEDs), photodetectors, biosensors, and infrared windows.[33-34] Up to the present time, numerous synthetic strategies to generate ZnS nanomaterials with different shapes and sizes have been published, including chemical vapor deposition, hydrothermal methods, and wet chemical methods, etc.[35] Compared with sulfides, transition metal phosphides (M_3P_2) are a more recently discovered semiconductor which has higher photocatalytic activity due to the more promising electronic properties and an electron-rich metal surface.[36-37] Zinc phosphide (Zn_3P_2) has a perfect band gap (1.5 eV) that matches with the theoretical optimum for solar energy conversion, as well as a large absorption (10^4 cm^{-1}) and long minority diffusion length (5-10 μm).[38] These features make Zn_3P_2 a promising candidate material for photovoltaic applications.[39] However,

because of the severe synthetic reaction conditions and the use of flammable phosphorous sources, developments of these materials and applications are somewhat restricted.[40] In chapter III, we proposed to synthesize a new semiconductor material, zinc sulfophosphide ($ZnPS_3$) using anion exchange and diffusion reactions. Two strategies were applied. One starts with ZnS nanoparticles as templates that react with trioctylphosphine as a phosphorous source. By doing this, we wish to incorporate phosphorous atoms into ZnS structure and eventually generate $ZnPS_3$. However, no formation of $ZnPS_3$ was observed under any conditions. Another strategy is to use Zn_3P_2 nanoparticles as a template which react with elemental sulfur in oleylamine. From the results, we found that instead of generating $ZnPS_3$ as we planned, the original Zn_3P_2 structure was converted to ZnS structure by H_2S that was released by sulfur and oleylamine complex.

Another popular and well-studied class of nanomaterials are metal nanoparticles. When the dimension of a metal solid is confined to the nanoscale, the effect of absorption of photons by the metal is amplified enough to cause oscillations of the electron cloud on the surface.[41] The collection of oscillations is called a "plasmon", which gives them unique and interesting optical properties.[42,43] Typical examples of this property are gold nanorods, which have attracted a great deal of attention and have been studied intensively due to their anisotropic shape and the ease to functionalize the surface.[44] Additionally, metal nanoparticles may also contain multiple types of metals. Intermetallic nanoparticles, consist of two different metal atoms and possess the properties of both metals. One of the most common intermetallic nanoparticle is gold-based, AuM(M = transition metal), such as Au_3Fe, Au_3Ni, $AuNi_3$, and AuFe. So far, gold-based intermetallic nanoparticles are synthesized by solution based in-situ reactions at high temperature, which make it difficult to control the shapes and sizes as well

as avoiding agglomerations. Chapter IV reports a novel procedure using *ex-situ* reaction to make Au_3Ni nanorods. Gold nanorods were synthesized using a previously published method with minor modification, followed by surface functionalization with oleylamine by a phase-transfer ligand exchange method. The resultant gold nanorods reacted with nickel precursor and yield Au_3Ni nanorods with no significant change in size and shape.

CHAPTER II

ZINC OXIDE MICROSTRUCTURES AS FLAME RETARDANT COATINGS ON COTTON FABRICS

Note: This chapter was published in *ACS Omega, **2018**, 3 (6), pp 6330–6338.* DOI: 10.1021/acsomega.8b00371, and reprinted with permission.

ABSTRACT

In this study, we report a unique strategy that utilizes ZnO and ZnS microparticles and rods as fire retardant materials when coated onto cotton fabrics. ZnO and ZnO/ZnS microparticles or rods were grown or adsorbed to the surface of cotton fibers. Properties such as heat release rate, total smoke release and mass loss rate of the materials were tested using a cone calorimeter. ZnO and ZnO/ZnS rods were able to reduce the heat release rate and total smoke release from 118 kW/m^2 and 18.3 m^2/m^2 to about 70.0 kW/m^2 and 6.00 m^2/m^2, respectively. The maximum average rate of heat emission (MARHE) and fire growth rate (FIGRA) index, which evaluate the fire spread rate, the size of the fire, and the propensity of fire development, are significantly improved with these coatings and indicate that there are potential applications of these materials as fire retardants. Vertical flame test was carried out and showed reduction in burning rate.

Introduction

Cotton fabrics have played an important role in the manufacturing of clothing and furniture in

the military and civilian sectors due to their desirable properties such as biodegradability, water absorbency breathability, and the vast availability of the raw materials for large-scaleproduction.[45-46] Cotton fabrics, however, can be easily ignited and pose a high risk for fires because cellulosic fibers have a low limiting oxygen index (LOI), a onset ignition temperature (360-425°C), and provide a rich source of hydrocarbon fuels during combustion that makes these materials highly flammable.[47-51] According to recent statistics, fires cause approximately 1.3 million accidents annually that result in more than three thousand deaths, fifteen thousand injuries, and an estimated $11.6 billion in direct property losses.[52] Home fires, where the main fire hazard is the combustion of textiles, are responsible for 80% of civilian fire deaths. [53]

The most widely used flame retardant strategy for cotton fabrics includes weaving or coating the cellulose fibers with a flame retardant polymer or compound to form a composite material.[54-60] Cotton fabrics can be directly coated with halogenated, nitrogen-containing or phosphorus-containing additives to improve their fire resistant properties but many of these compounds are limited in use because of their demonstrated toxicity. Halogenated flame retardants react with oxygen or hydroxyl radicals in the gas phase to effectively interrupt combustion.[50] However, toxic species released from the combustion of halogenated flame retardants are hazardous to human health and to the environment.[61-64]

Due to these concerns, the use of halogenated flame retardant materials has been rigorously restricted.[65-66] In addition to the gas phase flame retardant mechanism, nitrogen and phosphorus-containing compounds also exhibit flame retardant action in the condensed phase which is attributed to the formation of a ceramic-like char during thermal degradation that provides a layer of insulation to the underlying polymer.[50, 67, 68] Char forming compounds such as ammonium polyphosphate (APP), tetrakishydroxymethyl phosphonium chloride (THPC), sodium hypophosphite (SHP) and spirocyclic pentaerythritol diphosphoryl chloride (SPDPC) have been widely used as effective and durable flame retardant coatings for cotton fabrics.[69-70] Nevertheless,

studies suggest that phosphorus containing compounds produce large amounts of smoke, may be toxic, potential mutagens, or pose unwanted risks to human health and the environment.[47, 71-74]

New flame retardant strategies are based on incorporating insulating inorganic materials into cotton fabrics, a strategy that mimics the formation of a char layer of nitrogen and phosphorous containing compounds. Silicate nanoclays and ZnO nanoparticles have been introduced into phosphorus based polymeric flame retardants using the sol-gel method,[55] dual-cure processes,[57] and layer by layer assembly.[75] Lam and co-workers combined N-methylol dimethylphosphono propionamide (MDPA) with nano and micro scaled ZnO particles and showed that ZnO can act as co-catalyst to promote the formation of a char layer to enhance the flame retardant action of cotton fabrics.[76-77] Sharaf's group also observed better flame retardancy when they combined nano-ZnO with polycarboxylic acids and sodium hypophosphite with cotton fabrics.[47]

Based on these promising reports and work previously performed by our co-workers,[78] we investigated the combustion properties of cotton treated with spherical and rod shaped particles of ZnO and ZnS, as potential fire retardants, using cone calorimetry. To the best of our knowledge, no studies have investigated the flame retardant properties of these ZnO based coatings on cotton surfaces alone without the aid of other, usually harmful, flame retardant additives. The designed Zn-based microparticle coatings were expected to act as a protective layer of insulation[78, 79] and as smoke suppressants since zinc salts have been shown to reduce the production of smoke during burning.[80-82] ZnO and ZnO/ZnS rods were grown on cotton fabrics using a hydrothermal method previously published by our group.[83 84] In this paper, we show that even loosely adsorbed spherical microparticles of ZnO and ZnS can have a fire retardant effect on cotton fabrics independent of an organic flame retardant. For comparison, ZnO short rods with a similar mass loading as microparticles were grown on cotton fabrics and showed better performance in flame retardancy tests. We also show that the uniform protective coating of ZnO and ZnO/ZnS rods on the cotton surface results in a lower peak heat release rate (PkHRR), a lower fire growth rate

index (FIGRA), a lower maximum average rate of heat emission (MARHE), and a lower specific excitation area (SEA) compared to cotton alone.[68, 85]

Materials

Sodium hydroxide (ACS reagent, ≥ 97.0%, pellets), Triton X-100 (Bioxtra), zinc acetate dihydrate (ACS reagent, ≥ 98%), triethylamine (≥ 99%), zinc nitrate hexahydrate (≥ 99.0%, crystallized), hexamethylenetetramine (ACS reagent, ≥ 99.0%), zinc oxide (ACS reagent, ≥ 99.0%, powder) and zinc sulfide (10 µm, 99.99%, powder) were purchased from Sigma-Aldrich (St. Louis, MO). Citric acid (ACS reagent, ≥ 99.0%, crystal) was purchased from Spectrum Chemical Mfg. Corp. (New Brunswick, NJ). Sodium sulfide (nonahydrate, ≥ 99.0%) was purchased from Fisher Science Education (Nazareth, PA). Isopropyl alcohol (ACS reagent, ≥ 99%) and ethyl alcohol 200 proof (absolute, anhydrous, and ACS/USP grade) were purchased from Pharmco-AAPER (Shelbyville, KY). Bleached, desized cotton fabric (400) was purchased from Test Fabrics (West Pittston, PA). Polytetrafluoroethylene (PTFE) sheets (1/8" thick, 6 × 6"), Nylon 6/6 black wing nuts and Nylon off-white with shoulder screws (0.75" length) were purchased from McMaster-Carr (Douglasville, GA). Square PTFE frames were machined using an Epilog Mini 24 Laser Cutting System (40W) at the Oklahoma State University Visual Resource Center with a thickness of 1/8", outer dimensions of 6" × 6", and inner dimensions of 4" × 4" (empty space).

Procedures

Pre-treatment of cotton fabric. The cotton scouring solution was prepared by dissolving 2.50 g of NaOH, 0.75 g of Triton X-100, and 0.38 g of citric acid in 250 mL of high purity nanopure water (18 Ω/cm). Five cotton swatches (7" × 7") were placed in a 500 mL round bottom flask containing 250 mL of the scouring solution. The mixture was stirred at 100 °C for 1 h. The

scoured swatches were removed from the solution, rinsed thoroughly with high purity water (18 Ω/cm), and dried under ambient conditions.

Synthesis of ZnO rods on cotton fabric. ZnO rods were grown on the cotton surface using a previously published protocol by Athauda *et. al*.[83] A 50 mM solution of ZnO seeds was prepared by dissolving 2.75 g $Zn(CH_3COO)_2 \bullet 2H_2O$ in 250.0 mL of isopropanol. The resulting solution was stirred vigorously (300 rpm) at 85 °C for 20 min. Then, 1.745 mL of triethylamine was added drop-wise to the solution and stirred at 85 °C for an additional 15 min. This seed solution was allowed to cool to room temperature. Pre-treated cotton swatches were submerged in the seed solution for 15 min. and dried in a furnace (Binder®) at 120 °C for 1 h.

A 100 mM growth solution was made by dissolving 12.61 g of hexamethylenetetramine in 900 mL of high purity water (18 Ω/cm). Then, 26.77 g of $Zn(NO_3)_2 \bullet 6H_2O$ were added and the resulting solution was stirred for 24 h at room temperature. The ZnO growth solution was filtered (Whatman®, 150 mm) prior to use. Cotton treated with the ZnO seed solution was mounted onto a Teflon frame and submerged in 2.7 L of growth solution in a 4-L glass tank, and kept in a furnace at 95 °C for 5 h and 24 h to generate cotton coated with ZnO short rods (13% mass loading) and long rods (85% mass loading). The cotton was then rinsed with deionized water and dried under ambient conditions.

Preparation of the ZnO/ZnS rod- coated cotton samples. A 200 mM Na_2S solution was made by dissolving 43.23 g of Na_2S in 900 mL deionized water while stirring over night at room temperature. Precipitates were removed using filter paper (Whatman®, 150 mm). The Na_2S

solution (2,700 mL) was added into a 4000-mL glass jar. The cotton swatches functionalized with ZnO rods with 85% mass loading were mounted in a PTFE frame and submerged in the filtered Na_2S solution at 60 °C for 4 h. The cotton was then rinsed with deionized water and dried in air.

Preparation of the ZnO & ZnO/ZnS microparticle coated cotton samples. Suspensions of commercially available ZnO (24.41 g/L) and ZnS (19.49 g/L) microparticles were prepared in ethyl alcohol and stirred at room temperature overnight. The cleaned cotton swatches were soaked in a dispersion of colloids while stirring for 1 h followed by drying in an oven at 120 °C for 1 h. For samples containing ZnO + ZnS microparticles, cotton swatches was first soaked in the suspension of ZnO and, subsequently, in a suspension of ZnS.

Characterization

The morphology of the ZnO/ZnS structures as well as their attachment to the surface of the cotton samples was verified using a scanning electron microscope with beam voltage of 25 kV (FEI Quanta 600 FE-ESEM equipped with an EVEX Energy Dispersive X-ray Spectroscopy (EDS) system). The samples were coated with a thin (5 - 10 nm) layer of Au/Pt prior to SEM imaging. Transmission electron microscopy (TEM) was performed on ZnO and ZnO/ZnS nanostructures using a JEOL-JEM 2100 TEM equipped with an EVEX EDS system. Thermogravimetric analysis (TGA) was used to investigate the thermal decomposition of cotton samples with microparticle coatings using a Q-50 Thermogravimetric Analyzer (TA instruments, New Castle, DE). Samples weighed about 15-20 mg and were heated in a Pt pan. Experiments were carried out in both an air and nitrogen atmosphere (50 mL/min) using a heating rate of 20 °C/min in a temperature range of 25°C to 700 °C. Diffraction patterns were taken on a Rigaku SmartLab X-ray diffractometer (Cu Kα radiation) with a scan rate of 1 degree/min.

The combustion behavior of the cotton samples was investigated with a cone calorimeter (ISO 5660-1, Fire Testing Technology) at a heat flux of 50 kW/m^2 in a horizontal configuration. An electric ignitor was utilized to ignite the cotton during tests. The calorimeter was equipped with a gas analyzer. Nine layers of cotton were placed in the aluminum holder of the cone calorimeter. A metallic grid was placed on top of these cotton layers to maintain the configuration and eliminate the space between layers in the retaining frame. A surface area of 100 mm × 100 mm was exposed to radiation from the conical heater. The following data were collected: time to ignition (TTI, s), total heat release (THR, kW/m^2), heat release rate (HRR, kW/m^2), peak heat release rate (PkHRR, kW/m^2), effective heat of combustion (EHC, MJ/kg), mass loss rate (MLR, g/s), total smoke release (TSR, m^2/m^2), specific extinction area (SEA, m^2/kg), and CO and CO_2 yield (kg/kg). The maximum average rate of heat emission (MARHE) was evaluated as a measure of the propensity for the development of fire under real scale conditions.[85] The fire growth rate (FIGRA) index was calculated as the ratio of PkHRR to time to PkHRR, which is a figure used to evaluate the fire spread rate and the size of the fire.[68, 85]

Vertical flame tests were performed on 12 x 3" strips of fabric to study the effectiveness of the flame retardant coatings on cotton. The cotton strips were fastened to a metal frame and hung inside a VC-2 vertical flame cabinet (Govmark, Farmingdale, NY). The samples were then exposed to a Bunsen burner flame for 12 s and the after-flame and after-glow times were recorded following ASTM D6413-08 protocol.

Results and Discussion

Characterization of Cotton Samples

ZnO and/or ZnS particles were coated onto cotton surfaces by physisorption. ZnO and ZnO/ZnS rods were grown on the cotton fibers through a seed-mediated, two-step hydrothermal process as described in the experimental section. Commercially available ZnO and ZnO + ZnS

microparticles were physisorbed onto a cotton surface by dip-coating in a suspension of ZnO (~10 μm) and ZnS microparticles (~10 μm), sequentially. Figures 2.1a & 2.1b show SEM images of the ZnO and ZnO + ZnS spherical microparticles adsorbed to the cotton mesh. Poor adhesion between the ZnO and ZnS microparticles with the cotton surface resulted in an uneven distribution of the particles and, hence, exhibited some clustering as can be seen from the elemental maps of Zn and S (Figures 2.1c & 2.1d). Figures 2.2a-d show representative SEM images of cotton fibers coated with ZnO and ZnO/ZnS core/shell rods generated by 24-hour reaction, which were fabricated using a hydrothermal process previously reported by Athauda *et. al.*[83] (see Experimental Section). ZnO rods were produced with an average length of 1300 ± 285 nm and width of 137 ± 39 nm (Figures 2.2a & 2.2c). A slight reduction in the average sizes of the ZnO/ZnS core/shell rods occurred during the sulfidation process (l = 1207 ± 323 nm, w = 234 ± 42 nm) (Figures 2.2a & 2.2c).[83] Figure 2e shows that single crystals of ZnO coated the entire cellulose fiber. The average thickness of the polycrystalline ZnS shell was 42.4 ± 7.5 nm as measured from TEM images (Figure 2.2f).[86] Figures 2.3a-b shows representative SEM images of cotton fibers coated with ZnO short rods (l = 201.1 ± 35.33 nm, w = 210.1 ± 14.6 nm) generated by a 5-hour reaction hydrothermal reaction. Short ZnO rods evenly grew on fibers surface and formed a thin uniform layer.

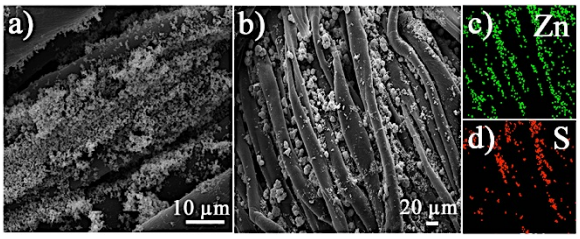

Figure 2.1. SEM images of cotton coated by (a) ZnO microparticles and (b) ZnO + ZnS microparticles. Elemental maps of (c) zinc and (d) sulfur show the uneven distribution of ZnO and ZnS microparticles adsorbed to the cotton surface.

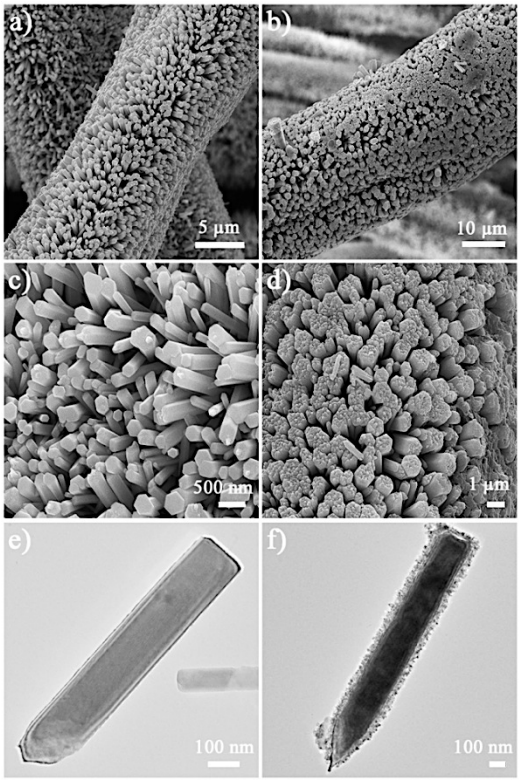

Figure 2.2. Electron microscopy images of ZnO and ZnO/ZnS rods grown on natural cotton. SEM images of (a) ZnO and (b) ZnO/ZnS rods on individual cellulose fibers. High magnification SEM images showing the hexagonal habit of the (c) ZnO rods and the rough texture of the polycrystalline (d) ZnS shell generated on the surface of the ZnO rod after sulfidation. Representative TEM images of (e) ZnO and (f) ZnO/ZnS core/shell rods detached from cotton surface.

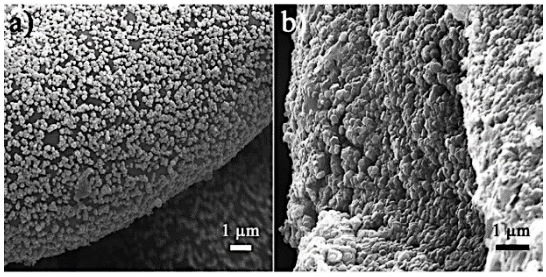

Figure 2.3. Electron microscopy images of ZnO short rods grown on natural cotton. SEM images of (a) ZnO on an individual cellulose fiber. (b) ZnO rods on fiber surface at high magnification.

Cone Calorimetry

The percent mass loading, A, of the coatings was calculated according to the following formula:

$$A = \frac{W_f - W_0}{W_0} \times 100\%,$$

where W_f is the weight of samples after treatment with particles and W_0 is the weight of the scoured cotton.[87-88] Table 2.1 shows the percent mass loading of the seven sets of cotton samples analysed. ZnO/ZnS core/shell rods had a higher mass loading percentage (85-92%) since they were chemically attached to the cotton fiber (Figures 2.1 & 2.2), unlike ZnO and ZnS microparticles. However, none of the coatings qualitatively changed the flexibility of folding and twisting significantly.

Table 2.1. Mass-loading of particles on cotton samples.

Sample	wt.%
Scoured cotton	0
ZnO microparticles	13.06
ZnO + ZnS microparticles	21.01
ZnO seeds	1.600
ZnO short rods (5 hours)	13.70
ZnO rods (24 hours)	85.24
ZnO/ZnS rods	92.55

Results of the combustion are presented in Table 2.2 from triplicate experiments. The data show similar trends. The various zinc coatings did not significantly or systematically improve time to ignition (TTI) of the cotton fabrics. However, total heat release (THR) was reduced by all of the coatings except for coatings bearing ZnO + ZnS microparticles. With the similar mass loading, ZnO short rod coatings had slightly better effect on reducing THR than ZnO microparticles. This is due to the more evenly formed protective short rod layers and stable chemical bonds. Cotton samples coated with ZnO and ZnO/ZnS rods released the least total amount of heat during combustion when compared to untreated cotton and cotton samples treated with microparticle

coatings (Table 2.2). Rod coatings exhibited the best reduction in THR as a result of their improved overall surface coverage on the cellulose fibers. ZnO/ZnS core/shell rod coatings were more efficient at reducing total heat release compared to ZnO rods. This is likely due to endothermic decomposition of the ZnS shell on the ZnO surface.[25, 26] The mass loading of ZnO short rod- coating was very similar and less than ZnO microparticles and ZnO + ZnS microparticles, but the ZnO short rod- coating was able to reduce total heat release more than ZnO microparticle and ZnO + ZnS microparticle coatings. The same trend was also observed for the effective heat of combustion (EHC) data (Table 2.2). All coatings reduced the EHC, but the effect was more pronounced for ZnO, ZnO/ZnS rod and ZnO short rod coatings. Figure 2.4a shows a graph of the heat release rate (HRR) of Zn coatings compared to untreated cotton. After ignition, the HRR of untreated cotton increased rapidly in the first 60 s and, subsequently, peak heat release rate (PkHRR) occurred at 60 s. PkHRR was reduced by the all of the coatings and, importantly, the time to reach PkHRR increased (Figure 2.4a). The HRR curves of ZnO seeds, ZnO short rods, ZnO microparticles, and ZnO + ZnS microparticles cotton samples had similar features but the peaks were shifted by 65-75 s compared to untreated cotton. Cotton samples coated with microparticles and ZnO seeds reduced the PkHRR by about 20-24%. The ZnO short rods coated cotton sample was able to reduce PkHRR by 33%, which was more effective than microparticles coated cotton samples with similar mass loading. This could be due to the better coverage and stronger bonding of ZnO short rods on the fiber surface, which provided a well distributed barrier between flame and fibers. The HRR of ZnO and ZnO/ZnS rod- coated cotton samples increased dramatically within the first 25 s, just like untreated cotton, but a slowdown was evident in the following 80 s, which indicates the flame retardant mechanism of the rod coatings was initiated at 25 s. ZnO and ZnO/ZnS core/shell rod coatings were more effective at retarding burning since PkHRR occurred at a much later time (95-110 s) and was reduced by 50%. This is mainly due to the uniform coverage of the ZnO and ZnO/ZnS rods on the fiber surface that provides a protective layer during combustion. The lower thermal conductivity of the

rod layer retards burning by slowing down heat transfer and spreading, and reduces the thermal pyrolysis rate of cotton.[89-91] These data suggest that more time would be available to escape, providing a better chance of survival, in case of an accidental fire.

Table 2.2. Combustion data.

	TTI (s)	THR (MJ/m^2)	EHC (MJ/kg)	Mean CO yield (kg/kg)	Mean CO_2 yield (kg/kg)	Mean MLR (g/m^2s)
Scoured cotton	15.0 (3.0)	16.0 (0.1)	14.53 (0.11)	0.0118 (0.0008)	1.38 (0.04)	9.30 (0.66)
ZnO microparticles	13.0 (1.7)	14.9 (1.2)	13.25 (0.52)	0.00853 (0.002)	1.29 (0.03)	8.25 (0.53)
ZnO + ZnS microparticles	14.7 (0.6)	16.7 (0.66)	13.81 (0.41)	0.0184 (0.002)	1.32 (0.04)	7.48 (0.76)
ZnO seeds	12.7 (2.0)	14.5 (0.53)	13.27 (0.68)	0.00950 (0.001)	1.29 (0.06)	9.11 (0.69)
ZnO short rods	9.33 (0.67)	14.3 (0.42)	12.74 (0.62)	0.00165 (0.0005)	1.29 (0.00)	6.84 (0.41)
ZnO rods	9.32 (0.6)	13.8 (1.1)	12.94 (0.42)	0.00743 (0.001)	1.27 (0.03)	5.78 (0.05)
ZnO/ZnS rods	13.3 (1.2)	12.1 (3.1)	12.27 (0.63)	0.0139 (0.001)	1.20 (0.06)	6.23 (0.37)

+ Data is from triplicate experiments. Values in parenthesis represent standard deviation ± σ.

Table 2.3. The smoke data of samples from cone calorimeter

	Mean SEA (m^2/kg)	Total Smoke Release (m^2/m^2)
Scoured cotton	13.76 (2.1)	16.06 (1.9)
ZnO microparticles	10.25 (0.44)	9.900 (2.1)
ZnO + ZnS microparticles	8.200 (1.1)	12.13 (0.32)
ZnO seeds	10.90 (2.5)	12.60 (2.1)
ZnO rods	6.583 (2.3)	7.433 (2.9)
ZnO/ZnS rods	6.756 (1.9)	7.867 (2.0)

CO_2 production rate curves from calorimetry experiments are represented in Figure 2.4b. Cotton samples with coatings had a lower average CO_2 yield and longer burning time. This indicates that the combustion was retarded by coatings as a result of the protective layer of the crystals on the surface of the fibers. Figure 4b reveals that the fire retardant mechanism occurs in the condensed

phase.[92] Specific excitation area (SEA) and CO and CO_2 yield are also shown in Table 2.2 and Table 2.3. SEA is a smoke measurement that represents the instantaneous amount of smoke released and the effective optical obscuring area generated per unit mass loss of specimen.[93] Untreated cotton produced an optical obscuring area of 14.66 m^2 per 1 kg mass loss during burning (Table 2.3). Zn coatings significantly reduced the SEA, which means coatings could provide improved visibility for escape in case of a real fire. This is consistent with work by others showing that Zn salts can act as smoke suppressant and reduce the SEA as well.[80-82] Compared to microparticle and seed coatings, rod coatings reduce the SEA more effectively. This trend correlates well with THR and EHC data, which also result from the protective insulation layer on the fiber surface that reduces the rate and intensity of combustion. ZnO microparticles, ZnO seeds, and ZnO rod and short rod coatings reduced CO yield, which results from slower and more complete combustion of the fabric. ZnO + ZnS microparticle and ZnO/ZnS rod- coated cotton samples release more CO than untreated cotton. This is because sulfur radicals produced from ZnS compete with other gas phase radical species for oxygen radicals to generate SO_2, which affects the combustion reactions in the flaming zone and leads to incomplete combustion (less CO_2 production). [94-96] The total smoke release (TSR) curve and data are shown in Figure 4c and Table 3. A similar trend was observed for untreated cotton samples and cotton samples coated with ZnO seeds, ZnO, ZnO + ZnS microparticles. Total smoke release curves generated by cone calorimeter tests are showed in Figure 4c. After ignition, the TSR increased rapidly within the first 15 to 20 s. After a slight reduction in the subsequent 20 to 25 s, the TSR then rapidly increased again until 100 s. This data is consistent with the PkHRR of the materials. At around 75 s, the TSR of untreated cotton samples surpasses all others. Cotton samples coated by ZnO and ZnO/ZnS rods had the lowest TSR. Additionally, the mean mass loss rate (MeanMLR) of the untreated cotton samples during combustion was 8.54 g/s, a value that was reduced by all of the coatings. ZnO and ZnO/ZnS rod coatings had the highest reduction, of about 32%, in MeanMLR. ZnO short rod coatings also had effect on reducing MeanMLR especially compared to ZnO

microparticle coatings with the similar mass loading. This result is consistent with ZnO and ZnO/ZnS rods forming a protective barrier to prevent burning and/or reduce the intensity of combustion compared to loosely adsorbed microparticles and small ZnO seeds crystals.

The fire growth rate (FIGRA) index and maximum average rate of heat emission (MARHE) are the two accepted evaluation parameters of a material's reaction to fire (Table 2.4). The FIGRA index is used to evaluate the fire spread rate and the size of the fire, and calculated as the ratio of PkHRR to time to PkHRR. MARHE is used to evaluate the propensity of fire development and calculated as a ratio of the accumulative heat emission to time. From the samples tested, coatings with ZnO/ZnS core/shell rods exhibited a lower FIGRA index and MARHE (0.990 kW/m^2s and 76.70 kW/m^2, respectively) and slightly out performed ZnO rod coatings (1.09 kW/m^2s and 77.30 kW/m^2, respectively). The nano-layer of ZnS on the core/shell rods is likely responsible for this improvement. At high temperatures, ZnS decomposes endothermically to release sulfur radicals, which react with oxygen to generate the non-flammable gas sulfur dioxide that further retards combustion. [95, 97-98]

Table 2.4. The fire growth rate (FIGRA) index and maximum average rate of heat emission (MARHE) values.

	FIGRA (kW/m^2s)	MARHE (kW/m^2)
Scoured cotton	2.86 (0.21)	140.4 (4.67)
ZnO microparticles	1.96 (0.11)	116.9 (7.05)
ZnO + ZnS microparticles	2.06 (0.045)	120.1 (8.24)
ZnO seeds	2.56 (0.41)	131.1 (9.50)
ZnO short rods	2.13 (0.29)	114.5 (2.18)
ZnO rods	1.19 (0.090)	86.40 (8.09)
ZnO/ZnS rods	1.19 (0.19)	85.90 (8.06)

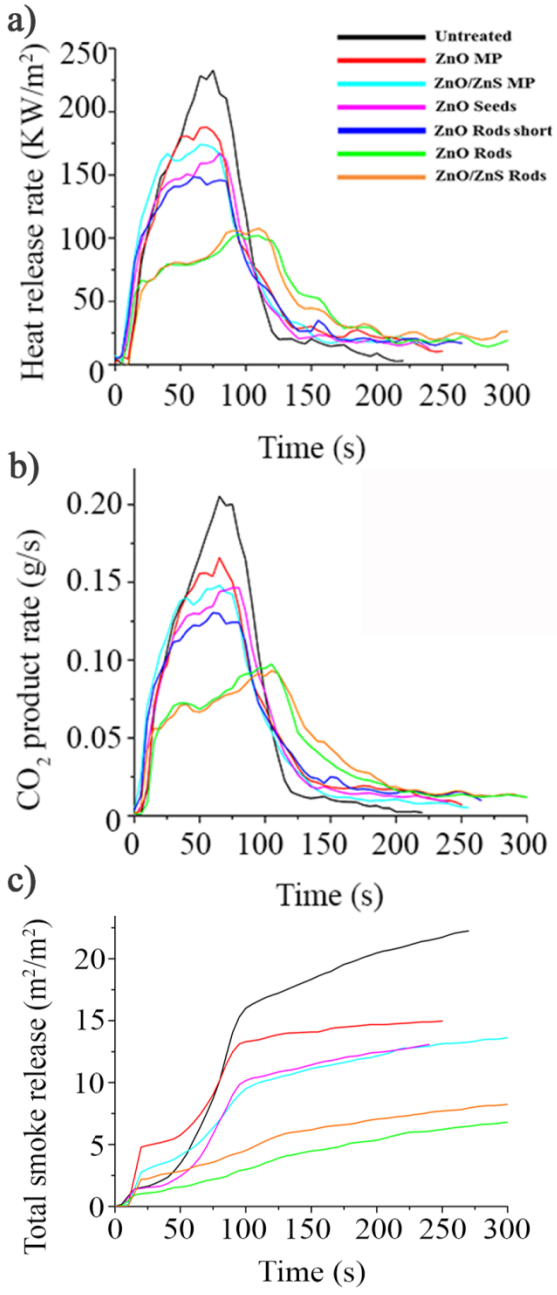

Figure 2.4. Graphs of combustion data of untreated and treated cotton fabrics showing (a) heat release rate (HRR), (b) CO_2 product rates, and (c) total smoke release (TSR). (MP = microparticle)

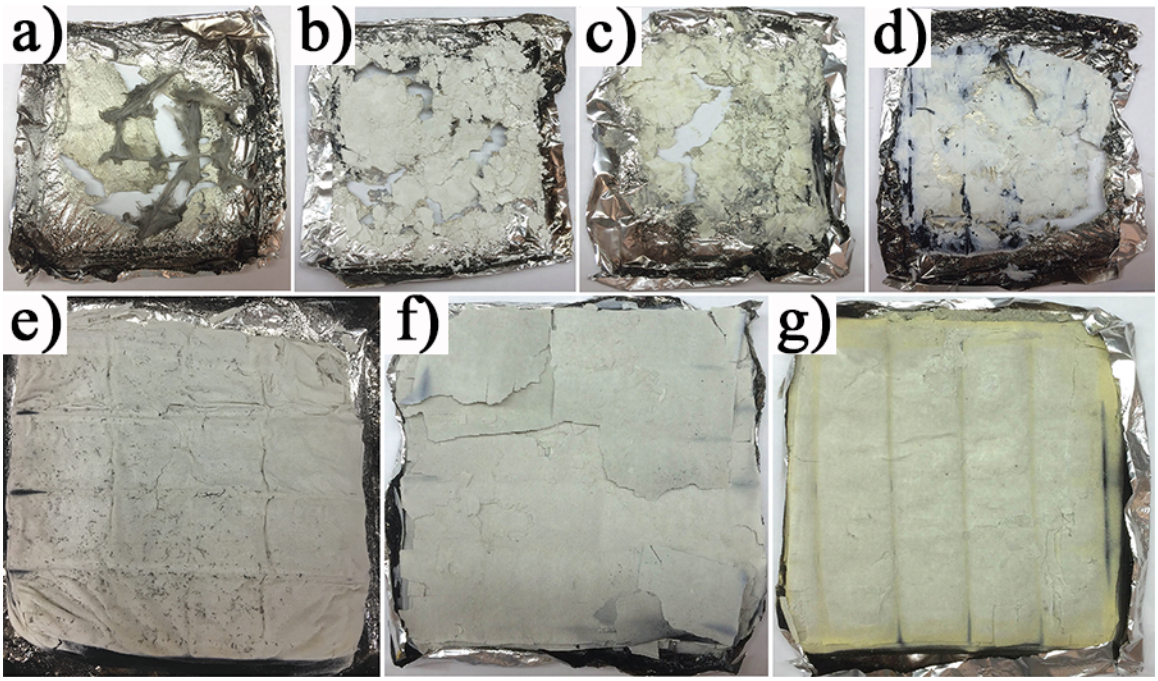

Figure 2.5. Pictures of (a) untreated cotton samples and cotton samples coated with (b) ZnO microparticles, (c) ZnO + ZnS microparticles, (d) ZnO seeds, (e) ZnO short rods (5 h), (f) ZnO rods (24 h), and (g) ZnO/ZnS rods after combustion tests.

Images of the cotton samples taken after the combustion tests are shown in Figure 2.5. After burning, the untreated cotton sheets were completely turned to ash as shown in Figure 5a. Cotton samples coated with ZnO microparticles, ZnO + ZnS microparticles, and ZnO seeds leave a white and/or light yellow solid residue that adheres to the aluminum holder (Figures 2.5a – 2.5d). The aluminum sample holders were burned through due to the high intensity of heat loading from combustion. ZnO short rod, ZnO rod and ZnO/ZnS rod-coated cotton samples maintain the original shape of the cotton fabric and, as a result, the aluminum holders survive intact after combustion (Figures 2.5e – 2.5g). SEM images of ZnO and ZnO/ZnS rod- coated cotton samples were taken after cone calorimetry experiments and are shown in Figure 2.6. ZnO and ZnO/ZnS rod coatings preserved the woven structure of the cotton fabric as seen in Figures 2.6a and 2.6b, respectively. This woven structure can also be observed in the cotton sample with the ZnO short

rod coating in Figure 2.6c. It appears to be loose due to the thinner short rod layers. Individual cotton fibers were completely consumed but a hollow shell of ZnO rods remained in place (Figures 2.6d and 2.6e). Figure 6f showed a similar hollow shell polycrystalline structure with porous and much thinner walls. High magnification SEM images of ZnO rods that form the protective layer around the cotton fibers are shown in Figures 2.6g and 2.6h. No damage or sintering of neighboring rods was observed after combustion. Decomposition of the ZnS shell on the ZnO/ZnS core/shell rods leaves behind ZnO rods with textured surfaces as shown in Figure 2.6h. Figure 2.6i represented a high magnification SEM image of ZnO short rods after burning. Compared with the morphology before burning, ZnO short rods appeared to have the same size and shape. This confirmed the excellent thermal stability of ZnO rods at high temperature regardless of size. Energy dispersive spectroscopy (EDS) and X-ray diffraction experiments confirm that the ZnS shell is no longer present on the surface of ZnO/ZnS core/shell rods after combustion (Figure 2.7 & 2.8). SEM data together with the cone calorimetry experiments suggest that the flame retardant mechanism at play is the formation of a protective layer of ZnO rods that acts as a barrier to slow down radiative heat and flames from penetrating the cotton surface. ZnO materials also exhibit size dependent thermal conductivity, *i. e.* reduced thermal conductivity with decreasing particle size.[90-91] This may be one reason why even ZnO seeds show good fire retardant properties and it also presents an opportunity to further tune or exploit this property to produce fire retardant products and textiles.

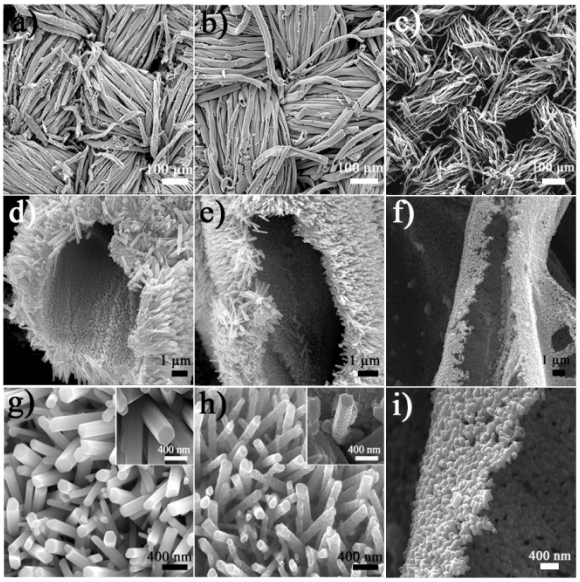

Figure 2.6. SEM images of ZnO and ZnO/ZnS rod- coated cotton samples after combustion. ZnO rods form woven structures from the combustion of cotton samples bearing (a) ZnO rods, (b) ZnO/ZnS core/shell rods, and (c) ZnO short rods. Hollow shells of ZnO rods are formed after cotton fibers were burned during calorimetry experiments of cotton samples decorated with (d) ZnO rods, (e) ZnO/ZnS core/shell rods, and (f) ZnO short rods. (f) The thickness of the formed hollow shell is much thinner for ZnO short rods than the other two samples, which is consistent with shorter length. Long (g) and short (i) ZnO rods retain their shape after combustion; whereas, the ZnS shell of the ZnO/ZnS core/shell rods decomposed to leave behind textured ZnO rods (f). Inset: Magnified images of a rod to show surface roughness.

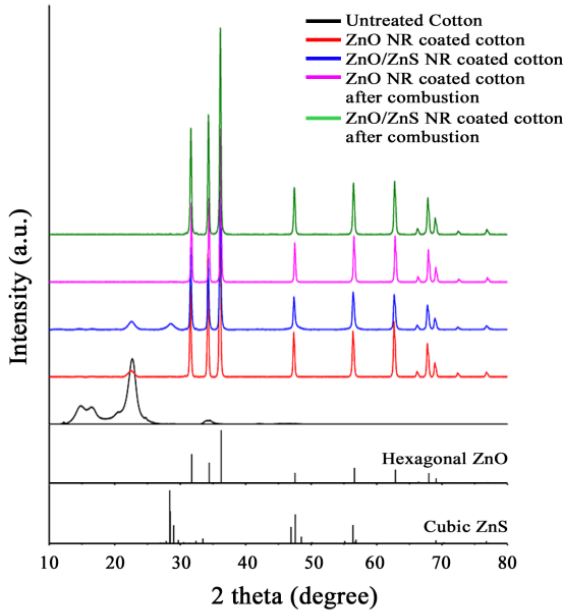

Figure 2.7. XRD pattern of ZnO and ZnO/ZnS nanorods coated samples before and after combustion.

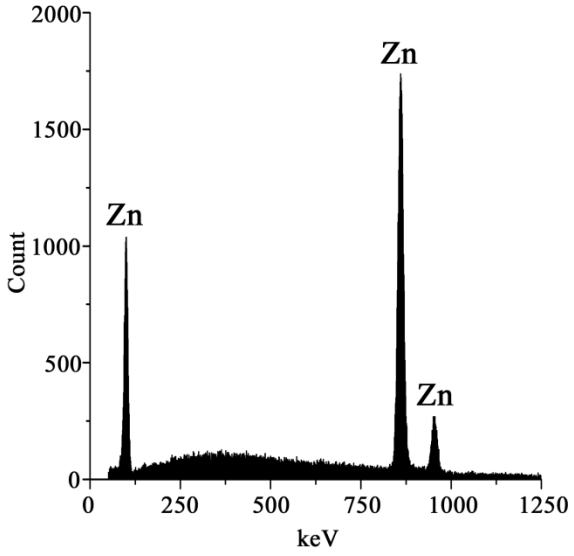

Figure 2.8. Energy-dispersive X-Ray spectrum of ZnO/ZnS rod coated cotton sample after combustion. Sulfur is converted to SO_2 gas, leaving no trace of sulfur behind.

Vertical flame tests

Table 2.5. Data of vertical flame tests

Samples	Residual Wt (%)	After-Flame Time (s)	After-Glow Time (s)	Burning Rate (in^2/s)
Untreated Cotton	0	11.4 ± 0.40	8.4 ± 0.60	3.16 ± 0.12
ZnO Microparticles	N/A	12.7 ± 0.90	9.5 ± 0.90	2.83 ± 0.21
ZnO + ZnS Microparticles	N/A	11.7 ± 0.50	8.5 ± 0.60	3.08 ± 0.12
ZnO Seeds	N/A	12.6 ± 1.9	9.5 ± 1.9	2.09 ± 0.41
ZnO short rods (5h)	N/A	9.90 ± 1.9	7.2 ± 1.4	3.72 ± 0.78
ZnO rods (24h)	40.5 ± 1.8	9.90 ± 1.5	3.3 ± 0.50	3.67 ± 0.50
ZnO/ZnS rods	43.2 ± 0.8	13.6 ± 2.0	3.8 ± 1.8	2.68 ± 0.41

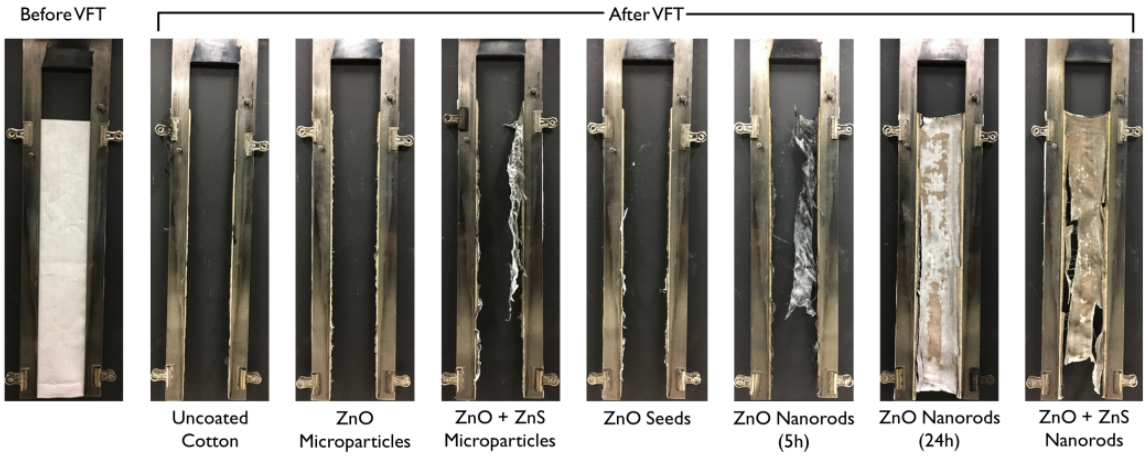

Figure 2.9. Pictures of untreated and treated cotton fabrics before and after vertical flame tests.

Flame tests were carried out on vertical orientations and the data were showed in Table 2.5. During the test, none of the samples were able to terminate burning, which indicates the absence of the self-extinguishing property. However, while burning, ZnO, ZnO + ZnS, ZnO seeds, and

ZnO short rods coated cotton became quite flaky and brittle, and eventually fell apart and detached from the frame due to the vertical configuration. This is due to the loose binding of particles on fiber surface and poor coverage of layers formed by particles. Light or no flakiness was observed for ZnO and ZnO/ZnS rods coatings. Residues of ZnO rods and ZnO/ZnS rods coated cotton samples maintained the original shape after burning and were able to stay in sample holders, while untreated cotton samples, cotton samples coated by ZnO, ZnO + ZnS microparticles, ZnO seeds and ZnO short rods were completely consumed and did not have residues left after the combustion (Figure 2.9). This result is consistent with cone calorimeter test results (Figure 2.5) and SEM images of samples after burning (Figure 2.6). The total burning time was increased when cotton samples were coated by ZnO microparticles, ZnO + ZnS micropartcles, ZnO seeds, and ZnO/ZnS rods. This indicates that the burning was slowed down due to the particle coatings on fiber surface. The rate of burning was calculated as the ratio of sample area to after-flame time, which represents how fast the samples are consumed by flame. Compared with untreated cotton, all coatings, except ZnO rods, more or less reduced the burning rate and slowed down the spread of flame. The after-glow time was reduced by ZnO and ZnO/ZnS rods, which might be due to the ceramic property of ZnO and ZnS thick coating layers on the fiber surface.

Thermal stability

Thermal decomposition was studied by thermogravimetric analysis (TGA) and differential thermal analysis (DTA) performed in air and nitrogen (Figure 2.10). The TGA curves collected in air (Figure 2.10a) shows that the onset temperature of degradation of untreated cotton was around 340 °C and peak decomposition rate appeared at 350 °C (Figure 2.10b), which matches with previously observed data.[99-101] The onset temperature of degradation of untreated cotton was found to be higher in nitrogen (Figure 2.10c) at around 350 °C. The peak decomposition rate occurred at 360 °C (Figure 2.10d), which is due to slower pyrolysis of cellulose under an inert

atmosphere.[101-102] Compared to untreated cotton, the onset temperature and peak decomposition rate were not significantly changed by ZnO microparticle coatings in air and nitrogen, which indicates the coating did not improve the thermal stability of cotton. The curve of ZnO + ZnS microparticle coatings shows a decomposition onset temperature of 290 °C and a steeper decrease in weight percentage from 290 to 340 °C, which is due to the catalytic effect of sulfur on decomposition of cellulose that causes mass loss at a lower temperature compared to untreated cotton.[99, 103-104] ZnO seed coated cotton samples show a similar trend with untreated cotton below 350 °C in both air and nitrogen. A significant weight loss event occurred during TG experiments of ZnO seed coated cotton performed in air observed at 370 °C in TGA curves (Figures 2.10a) and at 475 °C in DTA curves (Figure 2.10b). This is attributed to the collapse of the thin protective layers of ZnO seeds on the fiber surface and further oxidation and decomposition of the char residue of the cotton, which is missing in tests in nitrogen due to lack of oxygen (Figure 2.10c & 2.10d).[105] In both air and nitrogen, ZnO rod and short rod coatings had similar onset temperature of degradation and did not improve the thermal stability of cotton samples since the onset temperature of degradation occurred a similar temperature. Compared to cotton samples with other coatings, the onset temperature of mass loss is slightly increased by ZnO/ZnS rod coatings, which might result from the endothermic decomposition of ZnS shell.[106-107] The left over residue is ZnO (which does not decompose) and an oxidized char of cotton (0.54 mass %).[87, 108-109] The TGA data are consistent with the time to ignition (TTI) data and show good correlation with the residue mass results from the calorimetry experiments.

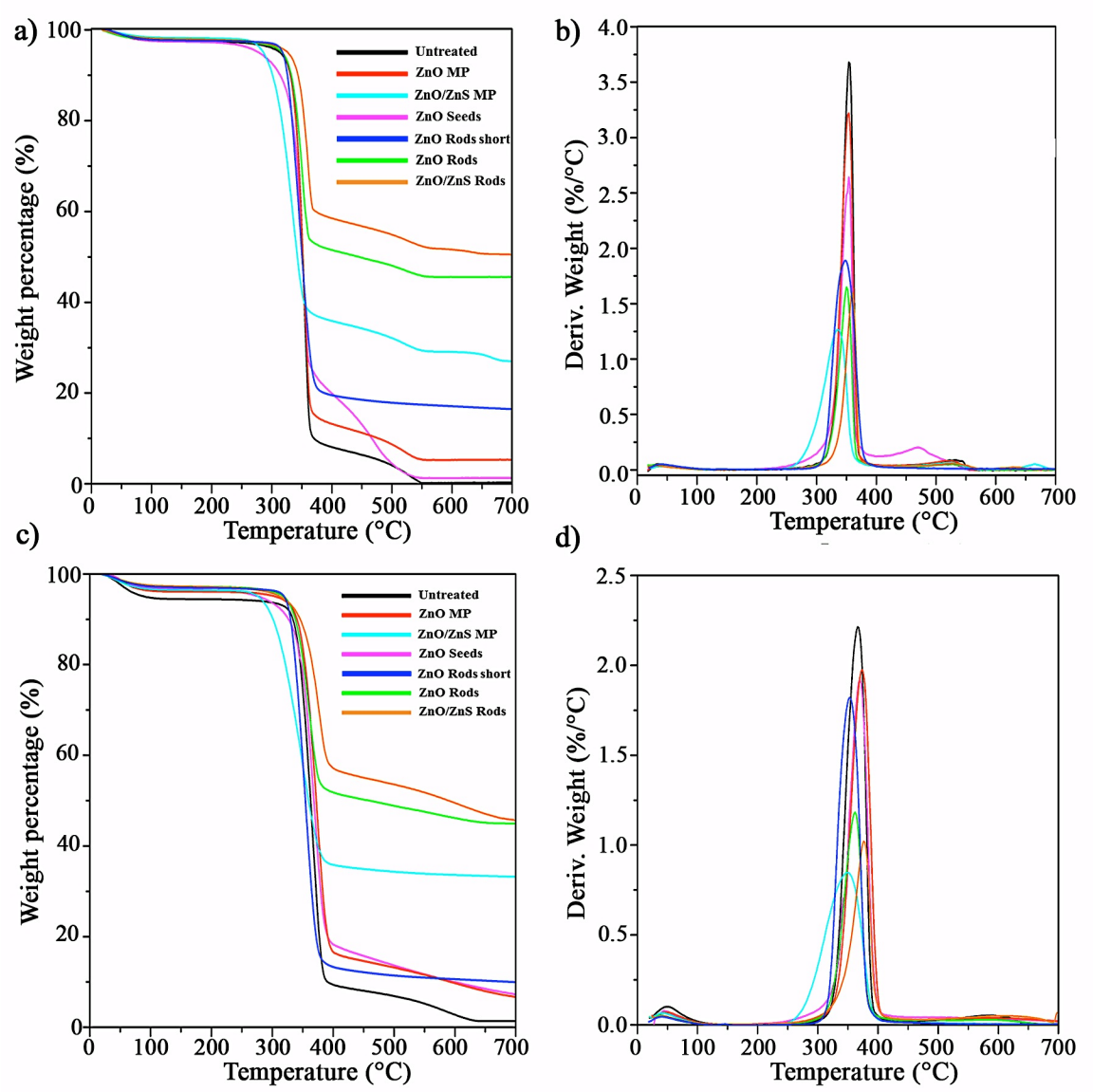

Figure 2.10. Thermogravimetric (TG) analysis and differential thermal analysis (DTA) curves of untreated cotton and cotton samples with coatings in air (a) and (b), respectively, in nitrogen (c) and (d), respectively. (MP = microparticles)

Conclusion

We show that ZnO materials, in general, are effective at reducing PkHRR even when unassisted by an organic fire retardant. Cotton samples with ZnO and ZnO/ZnS rod- coatings (85-90% mass loading) showed improved HRR when compared to untreated cotton. ZnO particles chemically

grown on cotton formed a uniform protective coating on the cotton surface resulting in lower peak heat release rate (PkHRR), lower fire growth rate index (FIGRA), and a lower maximum average rate of heat emission (MARHE) compared to cotton. ZnO/ZnS rods with a core/shell structure had a slightly better effect at retarding combustion likely from the release of sulfur radicals. However, the lack of self-extinguishing properties suggested that coupling with other chemical/molecular flame retardant materials, ZnO materials could show better flame retardancy. The functional properties of ZnO such as low thermal conductivity, high mechanical strength,[110] air permeability,[111] UV-absorption,[112] favourable whiteness index,[113] and biocompatibility[114] coupled with the combustion behaviour indicate that these materials have a promising future as eventual fire retardant coatings on cotton fabrics.

CHAPTER III

CONVERSION OF NANOSCALED ZINC PHOSPHIDE TO ZINC SULFIDE

Introduction

Semiconductor materials have conductivities falling between conductors and insulators and due to their special conductivities, they have been playing increasingly important roles in daily life as well as the development of sciences and technologies.[115-117] Compared with bulk materials, nanoscale semiconductors possess unique size- and shape- dependent optical and electrical properties.[118-120] In the 1980s, Brus introduced the concept of the "quantum confinement effect" to explain the correlation between the morphology of materials and their properties.[121-124] These properties make semiconductor nanomaterials excellent candidates for applications in various systems, such as catalysis,[120, 125] energy conversion systems,[126-127] and photoluminescence and optical devices.[128-129] In the last century, semiconductor nanomaterials have been investigated intensively and multitude synthetic methods have been developed to generate different semiconductors.[130-132]

The majority research focuses on II-VI semiconductor nanomaterials (ZnX, CdX, X=O, S, and Se) due to their prominent high-quality and crystalline particles.[122, 133-134] One of the most well studied II-VI semiconductors is ZnS nanocrystal that has the wide band gap (3.73 eV), the large bond energy (37 meV) and high photocatalytic activity.[118, 122, 135-136] ZnS nanocrystal is an ideal material and has been used extensively in photo- and electro- luminescence (PL & EL),

devices,[137-138] photocatalysts for the splitting of water,[139] and light emitting diodes (LEDs).[136] Moreover, the efficiency of ZnS nanomaterials can be affected by the particle morphology, crystal structure, and degree of crystallinity.[136, 140] Up to the present time, colloidal ZnS nanocrystals with different shapes and sizes have been successfully synthesized using various methods, such as chemical precipitation method,[141-142] hydrothermal method,[143-144] sol-gel method,[145] and chemical vapor deposition method,[146] etc. Among all synthetic methods, hydrothermal is one of the most widely used methods as it readily generates uniform and un-agglomerated nanoparticles with pure phases.[35] Zinc salts (zinc acetate, zinc nitrate, and zinc chloride) and organometallic compounds (zinc acetylacetonate) are typically adopted as zinc precursors while elemental sulfur, dodecanethiol (DDT), and thiourea are used as sulfur sources.[35, 124, 144, 147-148]

Compared to II-VI semiconductors, transition metal phosphides are relatively new semiconductors that have also attracted broad attention in recent years.[40, 149] Among the earth abundant transition metal phosphides, zinc phosphide (Zn_3P_2) exhibits an ideal band gap (1.5 eV) for solar energy conversion, large absorption coefficient ($>10^4$ cm^{-1}) and long minority carrier diffusion length (5-10 μm).[38, 150] Zn_3P_2 nanomaterials have great potential as photovoltaic materials.[151-152] However, as a fairly new semiconductor material, colloidal Zn_3P_2 nanoparticle has very limited synthetic methods available. In 2001, O'Brien and co-works successfully generated uniform Zn_3P_2 nanospheres using highly reactive and hazardous reagents such as dimethyl zinc, di-fert-butylphosphine (HP^tBu_2) and n-Trioctylphosphine (TOP).[153] In 2013, this method was slightly modified by Buriak group to generate Zn_3P_2 nanospheres with pure crystal phase and uniform size, which were applied on photovoltaic devices.[154-155]

Based on previously published methods and mechanisms of synthesizing ZnS and Zn_3P_2 in solution, we attempt to develop synthetic methods to produce a new semiconductor nanomaterial, zinc sulfophosphide ($Zn_2P_2S_6$ or $ZnPS_3$). $Zn_2P_2S_6$ bulk crystal was first generated in 1986s by

Brec.[156] The experiment was carried out by melting elemental Zn, P, and S in the 1:1:3 stoichiometric ratio at 500 °C for two months.[157] In 1987, Nevett and Foot claimed they synthesized $K_{0.30}Zn_{0.85}PS_3$ in solution phase via cation-exchange reaction and annealing at high temperature.[158] In 2017, Mayorga-Martinez and co-workers developed a synthetic procedure to generate various layered metal thiophosphite materials (MPS_3, M=Zn, Fe, Ni, Cr, Mn, Co, Cd, Ga, Sn, and Bi). [158,159] They also proved that certain materials have high efficiency and excellent performance for hydrogen and oxygen evolution reactions.[159] However, all systems mentioned above present drawbacks, such as requirements for severe reaction conditions, low surface area due to the large size of products, and difficulty when dispersing in solvents.

To the best of our knowledge, there is no study on synthesizing $ZnPS_3$ crystals at a nanoscale in solution phase with mild reaction conditions. In this project, we utilized pre-synthesized ZnS and Zn_3P_2 nanocrystals as templates to react with phosphorus or sulfur precursors.[40, 144, 147-148, 154-155] The experiments were categorized into two major strategies: 1) Reacting ZnS nanoparticles with phosphorus precursors and 2) reacting Zn_3P_2 nanoparticles with sulfur precursors. Under each strategy, several systematic studies on reaction time, temperature, size and shape of templates, and ratio of reactants were carried out in order to understand reaction mechanism and find appropriate conditions to generate $Zn_2P_2S_6$. During this process, we are also interested to investigate the behavior of chemical species (ions and organic compounds) in solutions and roles they play during the reaction.

Materials

Tri-n-octylphosphine oxide (98%), dimethyl zinc (96%), and tri-n-octylphosphine (tech, 90%) were purchased from Alfa-Aesar. Zinc chloride (≥98%), oleylamine (tech, 70%), elemental sulfur, tetramethylammonium hydroxide (≥95%), ethylene glycol, thiourea (≥99%), zinc sulfide microparticles (~10 μm), and zinc stearate (ZnO, 12.5-14%) were obtained from Sigma-Aldrich.

Ethanol, acetone, isopropanol and reagents mentioned above were used without further purification. Toluene was degassed and distilled before use.

Characterization

The crystal structure was characterized by X-ray diffraction (XRD) using a Rigaku SmartLab X-ray diffractometer (Cu Kα radiation, λ = 1.54059 nm). The XRD powder samples were prepared by either directly drying nanoparticle suspensions on previously cleaned glass slides or grinding vacuum-dried samples on glass slides. Differential scanning calorimetry (DSC) measurements were carried out on a TA Instruments Q2000 equipped with a liquid nitrogen cooling system, at a gas flow rate of 50 mL/min. Powder samples were sealed in "Tzero" aluminum pans. The morphology of particles was studied by using a JEOL-JEM transmission electron microscope (TEM) operating at an accelerating voltage of 200 kV. The TEM samples were made by casting a drop of the isopropanol dispersion of nanoparticles onto a carbon coated copper grid. Fourier-transform infrared (FTIR) spectra were taken on a Nicolet iS50 ATR-FTIR spectrometer to identify ligands on particles and possible organic molecules in the structures.

Experimental

Strategy 1: ZnS nanoparticles + phosphorus source (TOP)

1. *In situ* reactions:

A solution containing 2 mmol $ZnCl_2$ and 2.3 g trioctylphosphine oxide (TOPO) was prepared in 10 mL oleylamine with brief sonication in a 100-mL 3-neck flask. This solution was heated to 170 °C and appeared to be clear and colorless. A reddish orange sulfur-oleylamine solution was prepared by dissolving 6 mmol of elemental sulfur powder in 2.5 mL oleylamine with vigorous stirring and brief heating in oil bath (60-70 °C), which was then injected into the 3-neck flask at 170 °C. Right after the injection, the mixture in 3-neck flask was heated to 320 °C and kept at 320

°C for 1 h, during which the color of the mixture turned to lighter orange.[148, 160] Sequentially, the temperature of the mixture was brought up to 330 °C and specific amount of trioctylphosphine (TOP) as phosphorus source was injected, after which the solution was heated to 370 °C and kept at this temperature for specific amount of time (Table 3.1). After the reaction, the mixture was cooled and quenched with 5-8 mL of ethanol. The product was collected after separation and purification with ethanol.

Table 3.1. Reaction time and the amount of TOP of *in situ* reactions.

Volume of TOP (mL)	Reaction time (h)
2.0	0.5
2.0	1.0
2.0	1.5
0.5	1.0
1.5	1.0
2.5	1.0
3.0	1.0

2. *Ex situ* reaction:

2.1 Reactions of ZnS nanocrystals with TOP

Synthesis of ZnS nanocrystals[144] In a 100-mL 3-neck flask, 3.67 mmol of $ZnCl_2$ was mixed with 7.43 mmol tetramethylammonium hydroxide in 25 mL of ethylene glycol (EG) and heated in oil bath to 100 °C with vigorous stirring. A solution of 3.67 mmol thiourea in 25 mL EG was prepared and injected into the 3-neck flask at 100 °C. After the injection, the mixture was heated to 150 °C and kept at 150-160 °C for 2 h. White powder was obtained after washing with ethanol and acetone and drying in vacuum.

Reaction of ZnS nanocrystals with TOP: A ZnS nanocrystal-TOP dispersion was prepared by mixing 0.0220 g of as-prepared ZnS nanocrystals in 1.0 mL of TOP with brief sonication. In a 100 mL 3-neck flask, a solution of 2.000 g of TOPO in 2.0 mL TOP was heated to 120 °C under Ar for 1 h to remove low boiling point impurities, moisture and oxygen from the system. The solution was heated to 360 °C, at which point the ZnS nanocrystal-TOP dispersion was injected into the flask and the mixture was kept at 360 °C for specific times (Table 3.2). For the temperature study, after reaching 360 °C, the temperature was brought down to a specific temperature, followed by injecting the ZnS nanocrystal-TOP dispersion and kept at this injection temperature for 1 h (Table 3.2).

Table 3.2. Reaction temperatures and times for reactions of ZnS nanocrystals with TOP.

Reaction temperature (°C)	Reaction time (h)
150	1
200	1
300	1
320	1, 2, and 3
340	1, 2, and 3
360	1, 2, 3, 4, 5, and 6

2.2 Reactions of ZnS microparticles with TOP

Commercially available ZnS microparticles (≈10 μm) were adopted as the ZnS source in this experiment series. 0.0220 g of ZnS microparticles was measured and dispersed in 1 mL of TOP with brief sonication. In a 3-neck flask, a solution of 2.000 g TOPO in 2.0 mL TOP was heated to 120 °C and kept at this temperature for 1 h under an Ar flow to remove low boiling point impurities, moisture, and oxygen. The resulting solution was then heated to 360 °C and the ZnS microparticles-TOP dispersion was injected, after which the mixture was refluxed under Ar for 1

to 7 h. White and slightly dark powder products were collected after separation and purification with ethanol.

2.3 Reactions of ZnS nanorods and nanospheres with TOP:

Synthesis of ZnS nanorods and spheres:[147] In a typical reaction, zinc stearate was used as zinc source and reacted with elemental sulfur to generate ZnS nanorods and thiourea to generate nanospheres in oleylamine as solvent and ligand. A 6.0 mL oleylamine solution of 0.15 mmol zinc stearate and 0.75 mmol sulfur source (elemental sulfur or thiourea) was prepared in a 50 mL 3-neck flask by brief heating and vigorous stirring under an Ar flow. After the solids dissolved, the clear resultant solution was heated to 280 °C during a period of 2 h and kept at this temperature for 3 h. The product was separated by centrifugation and purified with ethanol. A powder product was obtained after drying under vacuum.

Reactions of ZnS nanorods and nanospheres with TOP: In a typical reaction, 0.0220 g as-prepared ZnS nanorods or nanospheres were dispersed in 1.0 mL TOP with brief sonication. In a 3-neck flask, 2.000 g TOPO was mixed with 2.0 mL of TOP and heated to 120 °C and kept at this temperature under an Ar flow for 1 h to remove low boiling point impurities, moisture, and oxygen. Sequentially, the solution was heated to 360 °C followed by injection of the ZnS nanorods or ZnS nanospheres-TOP dispersion. The mixture was kept at 360 °C under Ar for different amounts of time, then cooled and quenched by ethanol (Table 3.3). White or black powder products were collected after separation; purification was performed with ethanol, followed by drying under vacuum.

Table 3.3. Reaction time of reactions of ZnS nanorods/nanospheres with TOP

	Reaction time (h)
ZnS nanorods	1
	3
	5
	7
ZnS nanospheres	1
	3
	5
	7

Strategy 2: Zn_3P_2 nanoparticles + sulfur source

1. In the solid state:

Synthesis of Zn_3P_2 nanoparticles[40, 154-155]*:* In a typical synthetic reaction, dimethylzinc was used as a zinc precursor, which is highly reactive and explosive and can spontaneously ignite in the air. Thus, it is important and necessary to remove moisture and oxygen from the systems. Before the reaction, a 3-neck flask was connected to a condenser, gas and thermometer inlet adapter, and a rubber septum. A pear-shaped flask was sealed with a rubber septum. Both systems were degassed by heating the glassware setups under vacuum and purging Ar. The 3-neck flask was placed in a heating mantle. 8.0 mL and 2.0 mL TOP was injected into the 3-neck flask and pear-shaped flask, respectively, with a syringe. The 3-neck flask was heated to 320 °C under an Ar flow. 0.1 mL dimethylzinc was transferred to the pear-shaped flask to mix TOP solution, which was then transferred to the 3-neck flask with a syringe. Right after injection, the mixture in 3-neck flask turned grey indicating the formation zinc formation and was heated to 350 °C in a period of 2 h and kept at 350 °C for 3 h. After the reaction, the resultant mixture appeared to be

dark and was cooled to room temperature. 10.0 mL dry toluene was injected into the 3-neck flask to dilute the mixture and quench the reaction. The final solution was settled over night and filtered by a 0.45 μm syringe filter to remove large agglomerations, after which Zn_3P_2 nanoparticles were precipitated by adding 40.0 mL isopropanol to the filtration. The Zn_3P_2 nanoparticles were separated by centrifuge and washed three times with isopropanol.

DSC experiment of Zn_3P_2 nanoparticles and elemental sulfur powder: A mixture of 3.5 mg as-prepared Zn_3P_2 nanoparticles and 3.5 mg sulfur powder was placed in a DSC aluminum pan and sealed with a lid. The pan with sample was placed in the instrument. Three settings were applied to run samples: (1) the sample was heated to 350 °C at a rate of 10 °C/min and cooled to room temperature; (2) the sample was heated to 420 °C at a rate of 10 °C/min and cooled to room temperature; (3) the sample was heated at a rate of 10 °C/min to 420 °C and held for 20 min prior to quenching to room temperature. Samples were collected afterwards.

2. In the solution phases:

2.1 Zn_3P_2 nanoparticles with Na_2S in methanol

A 0.2 M Na_2S methanol solution was prepared by mixing Na_2S pellet in methanol with long time sonication. 0.0126 g of Zn_3P_2 nanoparticles was weighed and added to the Na_2S methanol solution. With vigorous stirring, part of Zn_3P_2 was not able to dissolve and precipitate in the bottom. The final mixture was centrifuged and washed several times with methanol.

2.2 Reactions of Zn_3P_2 nanoparticles with elemental sulfur in oleylamine[147-148, 160-161]

Variation of temperature: A 6 mL oleylamine solution containing 0.05 mmol Zn_3P_2 and 0.75 mmol sulfur powder was placed in a 50 mL 3-neck flask with brief sonication. The solution appeared to be reddish orange, clear solution. The flask was then heated to 50, 80, 110, 140, 170, and 200 °C under argon and refluxing at the same temperature for 1 h. After reactions were

cooled to room temperature, 6 mL of isopropanol was injected to the flask to quench the reaction as well as precipitate product. After centrifuge and purification with isopropanol, product was dried in vacuum and appeared to be white solid.

Table 3.4. Different temperatures used for 1-hour reaction of Zn_3P_2 and elemental sulfur.

Reaction time (h)	Temperature (°C)
1	Room temperature
1	50
1	80
1	110
1	140
1	170
1	200

Variation of time with temperature[161]*:* A 6 mL oleylamine solution containing 0.05 mmol Zn_3P_2 and 0.75 mmol sulfur powder was placed in a 50 mL 3-neck flask with brief sonication. The flask was heat to 110 °C, 120 °C, and 130 °C under Ar and kept at the same temperature for 1 or 2 h.

Variation of the ratio of Zn to S: In oleylamine, 0.014 mmol of as-prepared Zn_3P_2 nanoparticles (~4 nm) was mixed with specific amount of sulfur to yield ratio of Zn to P from 1:1 to 1:4. With brief sonication, the mixture appeared to be dark brown and turbid solution, which was heated to 140 °C under argon and kept at the same temperature for 1 h. Afterwards, the reaction was cooled to room temperature and quenched with isopropyl alcohol to yield a lighter reddish brown and clear solution.

Table 3.5. Different Zn to S ratio used for 1-hour reactions of Zn_3P_2 and elemental sulfur.

Reaction time (h)	Ratio of Zn:S
1	1:1
1	1:2
1	1:3
1	1:4
1	1:5
3	1:5
5	1:5

Table 3.6. Different Zn to S ratio used for 1-hour reactions of Zn_3P_2 and elemental sulfur.

Reaction time (h)	Ratio of Zn:S
1	1:6
1	1:8
1	1:10
1	1:12
1	1:14
1	1:16
1	1:18

Variation of the reaction temperature: In oleylamine, 0.025 mmol of as-prepared Zn_3P_2 nanoparticles were mixed with 0.375 mmol of sulfur. The mixture was heated under argon to 140 °C and kept at the same temperature for 1, 3, and 5 h.

Result and discussion

Strategy 1: ZnS nanoparticles + phosphorus source (TOP)

***In situ* reaction**

The *in situ* reactions had two major steps. In the first step, Zn precursors ($ZnCl_2$) were reacted with the S-oleylamine complex and formed ZnS nanospheres at 320 °C.[148] The next step was initiated by injecting TOP to the ZnS nanospheres mixture, which was subsequently heated and kept at 360 °C. Systematic studies on the amount of TOP were carried out by varying the injected

TOP volume while the remaining parameters were kept the same. The collected products were tested by XRD (Figure 3.1) and their patterns show that the product matches with the crystal structure of $Zn(NH_3)_2Cl_2$ (space group $P2_1/n$).[162] When the amount of TOP was increased from 1.5 mL to 2.5 mL, the same product, $Zn(NH_3)_2Cl_2$, was obtained. However, when 3 mL of TOP was used, the intensity of the pattern was relatively low compared to others and some peaks merged together as well. The $–NH_3$ in the formula is from the amine group in the oleylamine molecule. When oleylamine is heated above its boiling point (350 °C), the C-N bonds cleave and the long carbon chains dispersed in the solution while the NH_3 group incorporated into the products.[163] For the systematic study of reaction time, the mixture was heated to 360 °C and kept at the same temperature for 0.5 h, 1.0 h, or 1.5 h after injection of 2 mL of TOP. The XRD patterns of the collected products are shown in Figure 3.2. After 0.5 h and 1.0 h reactions, obtained crystals have the structure that matches with $Zn(NH_3)_2Cl_2$. When the time was extended to 1.5 h, the XRD pattern of the obtained crystal structure matches with NH_4Cl, instead of $Zn(NH_3)_2Cl_2$. The results of two systematic studies indicate that longer reaction time at high temperature may cause the decomposition of the $Zn(NH_3)_2Cl_2$ compound. This is likely due to the high temperature and corrosive chemical environment created by TOP.

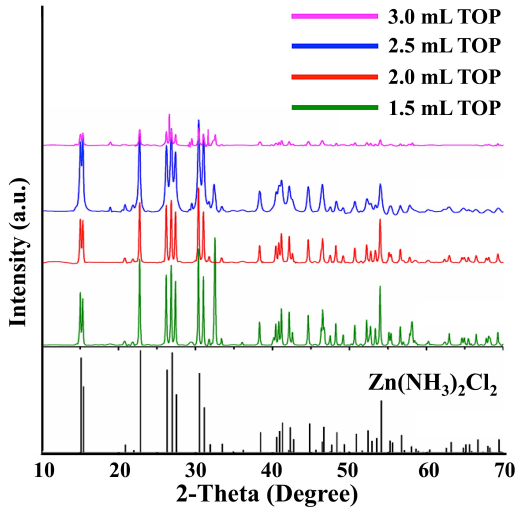

Figure 3.1. Powder XRD data for 1h *in situ* reactions with different amount of TOP.

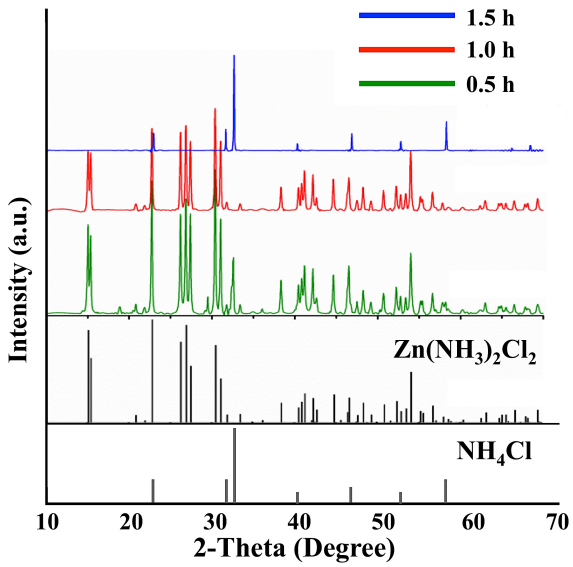

Figure 3.2. Powder XRD data for *in situ* reactions with 2 ml of TOP for different time.

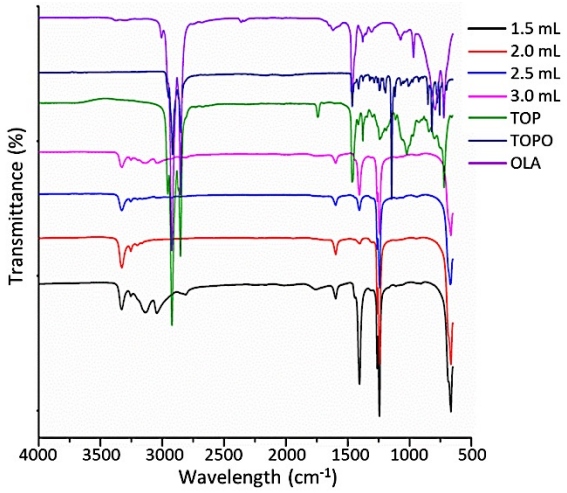

Figure 3.3. FTIR spectra for products from 1h *in situ* reaction with different amount of TOP.

The organic groups attached to nanoparticles are identified by FTIR and spectra are shown in Figure 3.3. The strong absorption peaks from 3000 to 2700 cm^{-1} in TOP, TOPO, and oleylamine, which due to the C-H stretching vibration, are not observed in any of the spectra of produced crystals.[164-166] This indicates that there may not be any ligands or organic surface stabilizers binding on crystals surface. Three peaks between 3400 and 3000 cm^{-1} from products spectra are

attributed to NH_3 stretching.[167] The peak located around 1600 cm^{-1} is from degenerate deformation and two peaks from 1370 and 1000 cm^{-1} are from symmetric deformation.[167] The peak at around 660 cm^{-1} is due to rocking vibration of NH_3.[167]

The TEM images of nanocrystals generated from 1-hour reactions with different amount of TOP are presented in Figure 3.4. Various interesting shapes and sizes were observed. TEM images for nanoparticles from 0.5 and 1.0-hour reaction with 2 mL TOP are shown in Figure 3.5(a) and (b). Nanoparticles presented multiple different shapes similar to nanoparticles from 1.0-hour reactions. Figure 3.5(c) shows the 1.5-hour reaction at 360 °C with 2 mL TOP. No nanoparticles were found under microscope. The reason could be that being heated in a corrosive solvent at high temperatures caused the decomposition of the crystalline products between 1.0 h and 1.5 h.

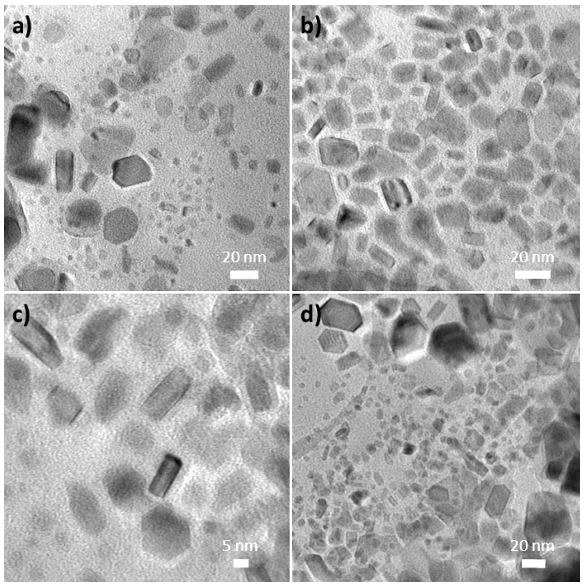

Figure 3.4. TEM images for nanoparticles from 1-hour *in situ* reactions with (a) 1.5 mL TOP b) 2.0 mL TOP c) 2.5 mL TOP and d) 3.0 mL TOP.

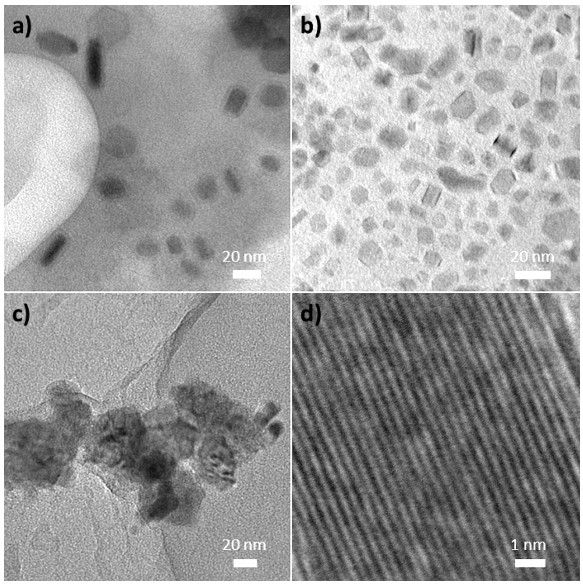

Figure 3.5. TEM images for nanoparticles from *in situ* reactions with 2 ml TOP for a) 0.5 h, b) 1 h and c) 1.5 h. (d) HRTEM image of (b).

***Ex situ* reaction**

Reactions of ZnS nanocrystals with TOP:

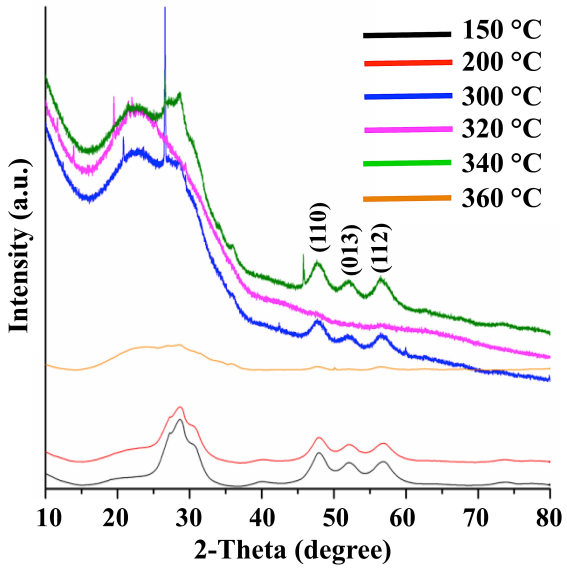

Figure 3.6. Powder XRD data for 1-hour reactions at different temperature.

XRD patterns of nanocrystals from reactions of ZnS with TOP are presented in Figure 3.6 for temperature study and Figure 3.7 for the time study. In Figure 3.6, with increasing temperature, the intensity of the reflections from the ZnS hexagonal structure were weak and new peaks begin to appear, some of which match with Zn_3P_2 structure. XRD patterns at the bottom came from products of reactions of ZnS and TOP at 150 and 200 °C. They are hexagonal structures with reflections at 26.9°, 28.5°, 30.5°, 39.7°, 47.6°, 51.8°, and 56.9° that result from planes (100), (002), (101), (102), (110), (103), and (112), respectively. The result indicated that ZnS did not react with phosphorus from TOP below 300 °C, which could be due to the requirement of high temperature to release phosphorus from TOP molecules. Hence, the temperature used in other experiments was increased. After ZnS reacting with TOP at 300 °C, 320 °C and 340 °C for 1 h, the products still showed a diffraction pattern of wurtzite type of zinc with reflections at 28.6°, 30.2°, 47.8°, 51.9°, and 56.5°, but intensities of these peaks were significantly reduced. For the product generated from the reaction of ZnS nanocrystals with TOP at 300 °C, three new peaks appeared at 20.8°, 26.6°, and 36.0°. After compared with the database, no match was found with the peak at 20.8°, but the peak at 26.6° and 36.0° matched with the most intense reflection plane (-120) in the ZnP_2 monoclinic structure (PDF No. 00-054-0208) and the plane (131) in the $ZnPS_3$ structure (PDF No. 03-065-4750). For the product from 320 °C reaction, there are three new peaks at 22.5°, 33.8°, and 35.9°, which matched with plane (200), (113), and (301) from $Zn_3(PS_4)_2$ structure (PDF No. 01-072-5951). Additionally, it is also possible that the peak at 35.9° was corresponding to the plane (131) in $ZnPS_3$ structure (PDF No. 03-065-4750). For the product from 340 °C reaction, five new peaks can be observed and attributed to two structures. Peaks at 26.6° and 45.8° might be from plane (202) and (400) in Zn_3P_2 tetragonal structure (PDF No. 1-074-1156). Peaks at 22.5°, 33.7°, and 36.0° might be corresponding to plane (200), (113), and (301), respectively, in $Zn_3(PS_4)_2$ structure (PDF No. 01-072-5951).

It is not likely that crystals with a mix structure of ZnS hexagonal and Zn_3P_2 were formed during reactions, since new peaks do not follow certain patterns. These new patterns seemed to match with some peaks in zinc sulfophosphide compounds, such $ZnPS_3$, $Zn_3(PS_4)_2$. When ZnS reacted with phosphorous atoms at high temperature, it is possible that ZnS crystal structure became loose and labile, some sulfur atoms were substituted by phosphide, and phosphide atoms were able to diffuse into zinc sulfide structure to form zinc sulfophosphide planes.

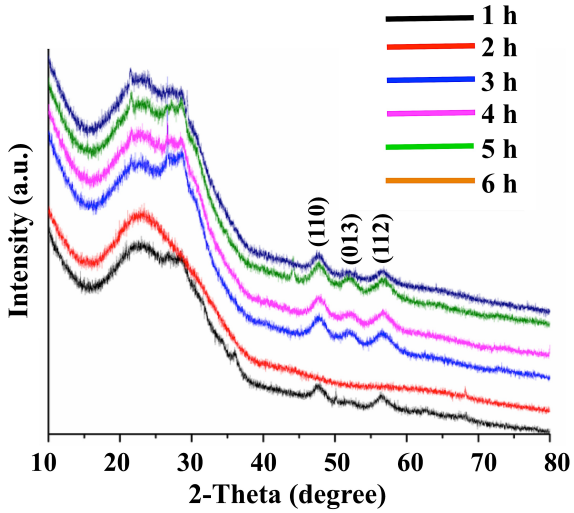

Figure 3.7. Powder XRD patterns for reactions at 360 °C with different time, from 1 h to 6 h.

Figure 3.7 shows the nanocrystals generated from 360 °C reactions with different reacting time. The original ZnS hexagonal crystal structure has been destroyed after reacting with TOP for 7 h since no features from ZnS can be observed in the XRD pattern. However, the only observable peak is at 36.5°, which matched with the plane (131) from $ZnPS_3$ (PDF No. 03-065-4750). This plane results in the most intense peak in this specific structure. All other peaks are characteristic of the ZnS hexagonal structure. Peaks at 28.4°, 30.4°, 47.6°, 51.7°, and 56.7° correspond to planes (002), (101), (110), (103), and (200). In addition, some of the products show new peaks. After 1-hour reaction of ZnS and TOP, there were three new peaks at 26.6°, 35.8°, and 50.1° on

the XRD pattern. The peak at 35.8° matched with the most intense peak in $ZnPS_3$ structure (PDF No. 03-065-4750), which is corresponding to the plane (130). The other two peaks matched with peaks from ZnP_2 monoclinic structure (PDF No. 00-054-0208), which come from plane ($\bar{1}$20) and (322). The peak at 26.6° was also observed in the XRD pattern of the 3-hour reaction product. In the XRD pattern of 5-hour reaction product, a new peak at 21.5° was observed but could not match with any possible compound, which might come from impurities. Another new peak located at 44.5°, which matched with the most intense peak (400) in Zn_3P_2 tetragonal structure (PDF No. 1-074-1156). In conclusion, during high temperature reaction with TOP, ZnS structure was eventually destroyed and a few new phases, including zinc phosphide and zinc sulfophosphide, were likely formed.

As analyzed with TEM images, one reason why the ZnS hexagonal structure can be easily damaged without forming new crystals could be that ZnS precursors used in these experiments are polycrystalline clusters, which are not as stable as single crystals and do not have a specific shape. In order to prevent the original template from being destroyed, either larger particles or single crystals should be used. Thus, we moved to microparticles as well as nanorods and nanospheres with ZnS single crystal structures.

Reactions of ZnS microparticles with TOP:

XRD patterns of particles after reacting with TOP for different time are presented in Figure 3.8. The crystal structures appeared to be the same as before. This might be due to the size of particles, which is around 10 μm. It is too difficult for the phosphorus released at high temperature to diffuse into the microparticles.

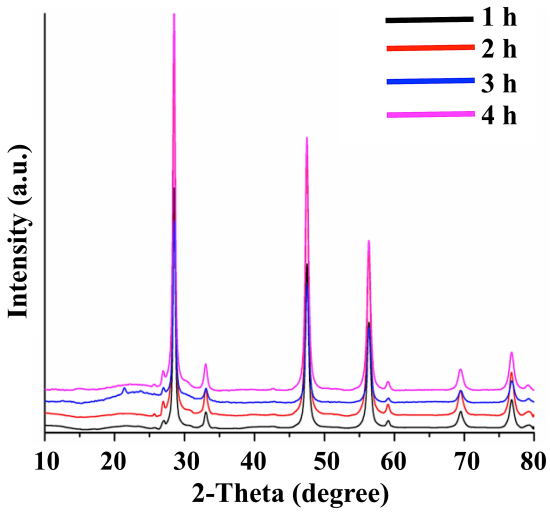

Figure 3.8. Powder XRD data of products from ZnS cubic microparticles and TOP reactions at 360 °C with different time.

Reactions of ZnS nanorods and nanospheres with TOP:

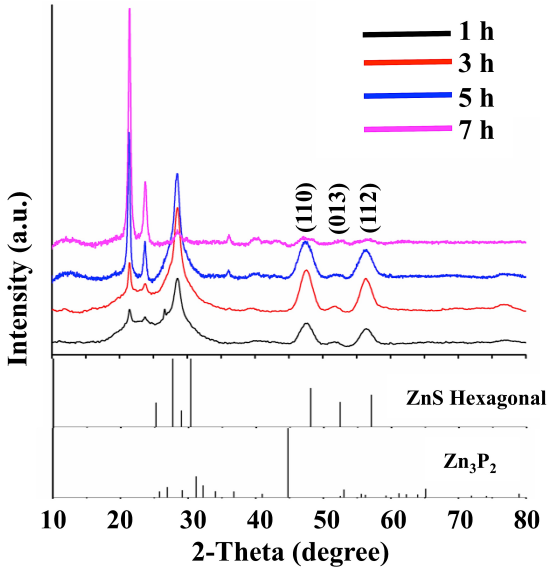

Figure 3.9. Powder XRD data of products from ZnS nanorods and TOP reactions at 360 °C with different reaction time.

The XRD patterns of nanoparticles from reactions of ZnS nanorods and TOP are shown in Figure 3.9. Four peaks at 47.4°, 51.7°, 56.4°, and 76.5° can be attributed to ZnS hexagonal structure, corresponding to the (110), (103), (112), and (210) planes, respectively. The intensities of these peaks were significantly reduced in the XRD pattern of product from 7-hour reaction suggesting smaller crystals. A small peak at 26.5° in the XRD pattern of the product from 1-hour reaction is from the plane (100) in the ZnS hexagonal structure, which can no longer be observed in other products from longer time reactions. A peak at 28.4° resulted from plane (002), which also belongs to ZnS hexagonal structure. The intensity of this peak decreases with increasing reaction time. These changes in peaks and intensities are indicating that when the reacting time was increased; ZnS structure was diminished due to the high temperature, corrosive reagent used in the reactions, and possible diffusion and exchange of anion happened during the reactions. Compared with the XRD pattern of the product generated by 1-hour reaction, in the XRD pattern of 7-hour reaction product, three characteristic peaks from 45° to 60° and the sharp peak at 28° are barely visible. However, two new sharp peaks at 21.3° and 23.7° appeared in all XRD patterns and the intensity increased with the increasing reaction time. These two peaks matched with the planes (111) and (210) in monoclinic ZnP_2 structure (PDF No. 00-054-0208). In addition, a small peak located at 37° appeared with increasing reacting time in XRD patterns of products from 5- and 7-hour reactions. It matched with plane (302) in tetragonal Zn_3P_2 (PDF No. 01-074-1156) structure. In this process, original structure was slowly converted to a new structure. In the product, it is possible that a mixture structure of zinc sulfide hexagonal and zinc phosphide monoclinic/tetragonal was formed.

The TEM images (Figure 3.10) of nanorods after reactions show that the long reaction time and high temperatures neither damaged the shape nor change the size of the particles. The high-resolution TEM images show lattice structure, which proved that resulting nanorods are still single crystals. The lattice spacing was measured to be 0.33 nm in the 1-hour reaction sample,

which is corresponding to the plane (100) in ZnS hexagonal structure and the peak at 26.5°. In the samples from 3- and 5-hour reactions, the lattice of 0.32 nm was measured, which could be attributed to plane (002) in ZnS hexagonal structure and the peak located at 28.4°. In the sample prepared from 7-hour reaction, the lattice spacing of 0.37 was measured and it is corresponding to the new peak at 23.7°. No lattice spacing of 0.32 or 0.33 were captured, which could be due to the destruction of plane (111) and (002) during the reaction. This result is consistent with the XRD pattern of the sample from 7-hour reaction, where peaks at 26.5° and 28.4° were not observed.

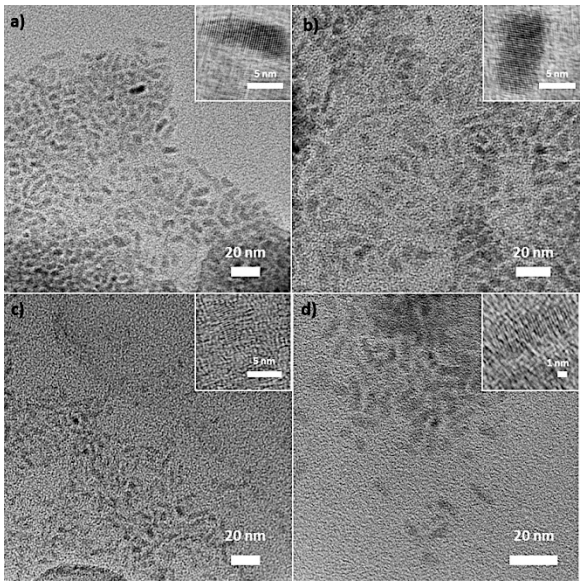

Figure 3.10. TEM images for nanorods from reactions of ZnS nanorods and TOP at 360 °C for (a) 1 h, b) 3 h, c) 5 h, and d) 7 h. Inset images are HRTEM images.

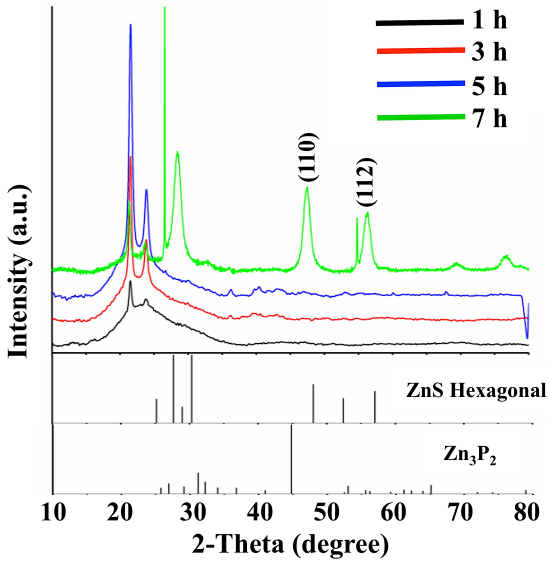

Figure 3.11. Powder XRD data of products from ZnS nanospheres and TOP reactions at 360 °C with different reaction time.

Figure 3.11 shows the XRD patterns of nanoparticles from ZnS nanospheres and TOP reactions. Unlike ZnS nanorods, after reacting with TOP, products generated from short time reactions did not maintain the ZnS hexagonal structure feature left. In 1-, 3- and 5-hour reactions, the collected products all had small peaks at around 30°, which is from plane (101) from ZnS hexagonal structure. Besides, a peak at 47.6° was observed after 1-hour reaction and peaks at 39.9° were observed after 3- and 5-hour reactions, which matched with plane (110) and (102) in ZnS hexagonal structure. For the sample from the 7-hour reaction, peaks at 26.6°, 28.4°, 47.5°, 56.4°, and 76° were observed and matched with plane (100), (111), (110), (112), and (210), respectively, in ZnS hexagonal structure. Similar to ZnS nanorods TOP reaction, three new peaks showed up after reacting with TOP, which could be from a new structure. In the XRD patterns of samples generated by short reaction times (1 h, 3 h, and 5 h), new peaks appeared at 21.4°, 23.8°, and 36.1°. These three peaks could be attributed to monoclinic and tetragonal Zn_3P_2 structures. This result is indicating that reactions with TOP might have caused a conversion from ZnS to Zn_3P_2 structure, so that the resulting products were mixture structure of both.

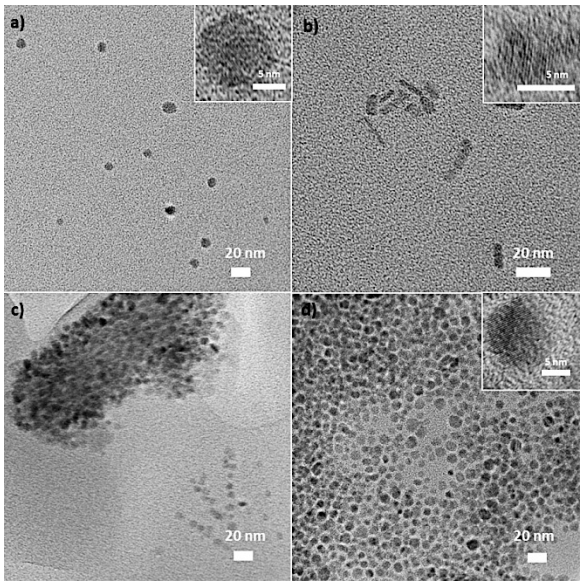

Figure 3.12. TEM images for nanoparticles from reactions of ZnS nanospheres and TOP at 360 °C for (a) 1 h, b) 3 h, c) 5 h, and d) 7 h. Inset images are HRTEM images.

TEM images show that nanoparticles were able to maintain the spherical shape after reacting with TOP (Figure 3.12 (a), (c), and (d)), except 3-hour reaction (Figure 3.12 (d)). A few particles grew to rod-shape during the reaction. Lattice spacing was measured to be 0.3 nm in the 3-hour reaction sample which was corresponding to plane (101) in ZnS hexagonal structure and a peak at around 30° was observed in XRD pattern. However, after 7-hour reaction, lattice spacing of 0.31 and 0.33 nm were captured in HRTEM, which are corresponding to plane (111) and (100) in ZnS hexagonal structure and sharp peaks at 26° and 28° were observed on XRD patterns.

Strategy 2: Zn_3P_2 nanoparticles + sulfur source

In the solid state

Figure 3.13 shows the XRD patterns of solids after DSC tests. After being heated to 350 °C and 420 °C, the several new peaks appeared on the XRD patterns. The peaks at 13.7°, 32.7°, and

55.1° matched with $ZnPS_3$ (PDF No. 03-065-4750) crystal structure and possibly resulted from plane (001), (131), and (330), respectively. Two peaks at 26.9° and 28.5° matched with ZnS hexagonal structure corresponding to plane (100) and (002). Additionally, the peaks at 30.5°, 47.6°, and 56.4° might be attributed to either ZnS hexagonal structure or $ZnPS_3$ (PDF No. 03-065-4750) crystal structure. They could be generated from plane (101), (110), and (103) in ZnS structure, or plane ($\bar{2}$01), (202), and ($\bar{3}$11) in $ZnPS_3$ structure. A peak matched with both Zn_3P_2 and $ZnPS_3$ appeared at 65.4°, which became more intense and clear with increasing temperature and time. It is likely to be a more crystallized plane in Zn_3P_2 due to calcination at high temperature or a newly formed plane from $ZnPS_3$ structure. The XRD results indicate that, upon mixing and melting together, elemental sulfur reacted with Zn_3P_2 and formed a new structure, which might be ZnS hexagonal the sulfophosphide crystal structure we have been aiming at. Therefore, the strategy 2 might be a right path to generate $ZnPS_3$ compounds.

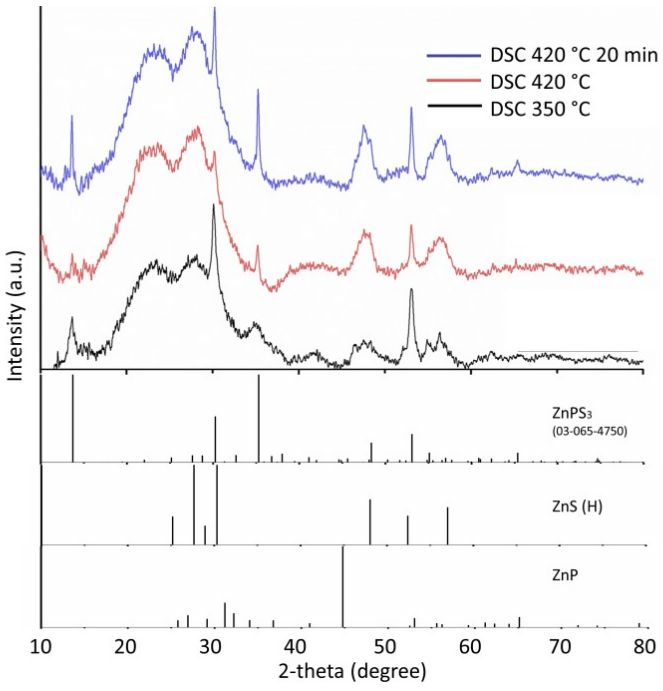

Figure 3.13. Powder XRD data of solids after DSC tests.

In the solution phases

Variation of the reaction temperature:

Figure 3.14 showed the XRD pattern of nanocrystals collected from 1-hour reactions of Zn_3P_2 and sulfur at 110 °C, 140 °C, 170 °C, and 200 °C, as no crystalline products were generated from reactions under 110 °C. It could be observed that the original Zn_3P_2 structure is no longer visible. Instead, with increasing temperature, a ZnS hexagonal structure becomes more intense and clear. The broad peak between 26° and 31° could be resulting from three peaks merging together. There three peaks are corresponding to plane (100), (002), and (101) in ZnS hexagonal structure. Moreover, another three peaks located at 47.4°, 51.6°, and 56.4° also match with characteristic peaks that generated by plane (110), (103), and (112), which are often considered as typical features of the ZnS hexagonal structure.

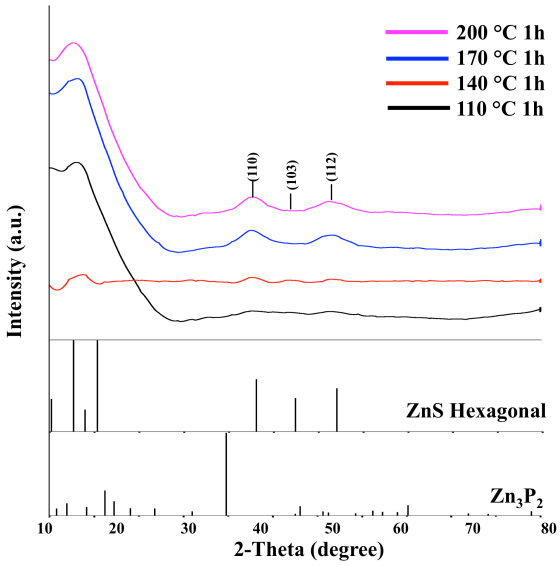

Figure 3.14. Powder XRD patterns of nanocrystals generated from 1-hour reactions at 110 °C, 140 °C, 170 °C, and 200 °C, comparing with ZnS hexagonal and Zn_3P_2 references.

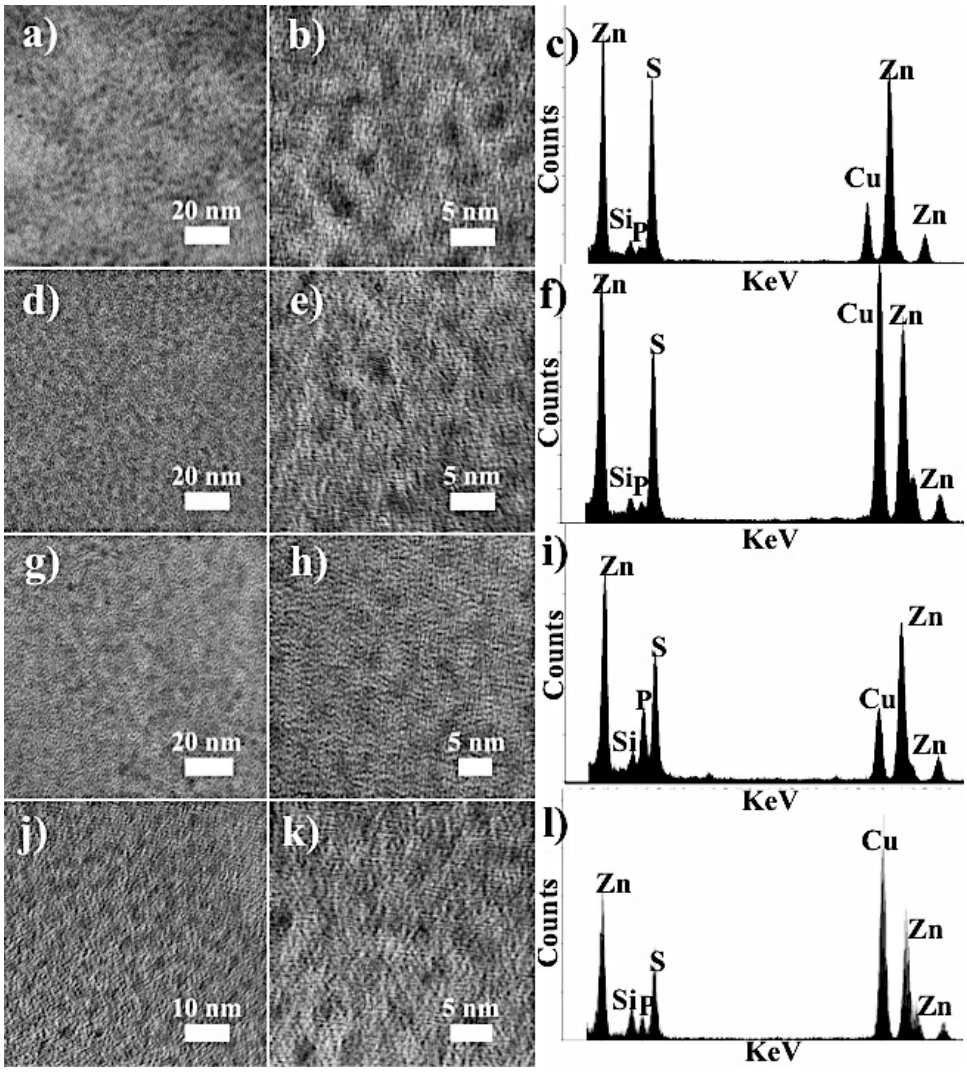

Figure 3.15. TEM images of nanocrystals generated from 1-hour reaction of Zn_3P_2 with elemental S in oleylamine at (a) and (b) 110 °C, (d) and (e) 140 °C, (g) and (h) 170 °C, and (j) and (k) 200 °C. Corresponding EDS spectra are presented on the right.

Figure 3.15 shows TEM images of the nanocrystals that were collected after 1-hour reactions of Zn_3P_2 and sulfur in oleylamine at 110 °C, 140 °C, 170 °C, and 200 °C. After the reaction, nanocrystals still maintain spherical shape and the average size is 4.2 ± 0.5 nm, as shown in low magnification images [Figure 3.15 (a), (d), (g), and (J)]. In TEM images with higher magnification [Figure 3.15 (b), (e), (h), and (k)], lattice fringes can be observed, which indicates the present of good crystalline structure in generated nanocrystals. Figure 3.15 (c), (f), (i), and (l)

show EDS spectra of nanocrystals generated from reactions under 110 °C, 140 °C, 170 °C, and 200 °C, respectively. According to the spectra, elements Zn, P, S, Si (from glassware), and Cu (from Cu TEM grids) present in the nanocrystals TEM grids.

FTIR spectra of products are shown in Figure 3.16. Three peaks from 3000 to 2750 cm^{-1} are stretching bands of $–CH_2–$ from oleylamine or TOP. The small peak at around 2350 cm^{-1} comes from P-H stretch. Two peaks at 1465 and 1377 cm^{-1} are attribute to bending of $–CH_2–$. Compared to Zn_3P_2, there is a new peak at around 720 cm^{-1} (denoted by green star), which could be $P^+ \rightarrow S^-$ band or $-CH_2-$ in plane deformation rocking. According to the crystal structural analysis from XRD, no phosphorous containing compounds were formed in any samples, so this peak most likely came from organic ligands with carbon long chain.

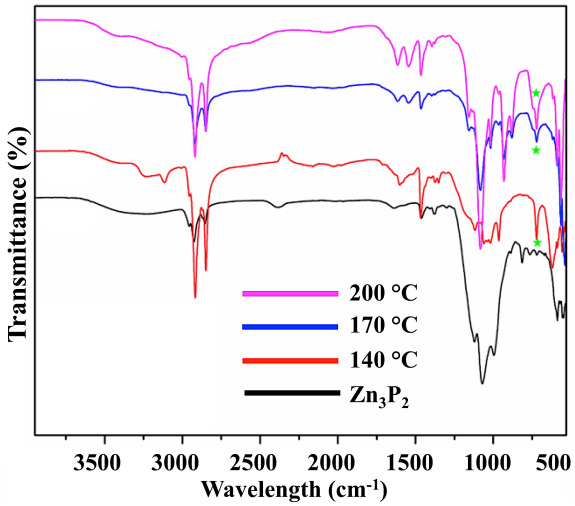

Figure 3.16. FTIR spectra of nanocrystals generated from 1-hour reactions of Zn_3P_2 and elemental sulfur at 140 °C, 170 °C, and 200 °C.

Variation of reaction time:

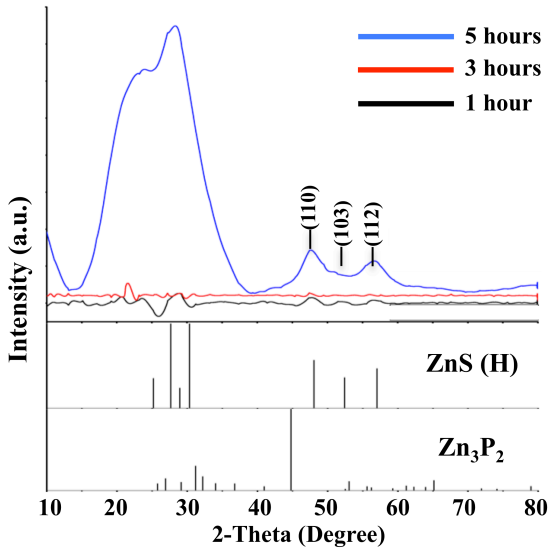

Figure 3.17. Powder XRD patterns of crystals generated from 1-hour, 3-hour, and 5-hour reaction of Zn_3P_2 and sulfur powder in oleylamine.

Zn_3P_2 nanoparticles and sulfur were mixed with a ratio of 1:5 in oleylamine and reacted at 140 °C for different amounts of time. Products were precipitated by isopropanol and separated by centrifugation. After purifying with isopropanol several times, the products were dried in the vacuum and grinded to powder for XRD. The patterns obtained were showed in Figure 3.18. As can be observed, no characteristic peaks from the Zn_3P_2 crystal structures are present in the patterns. However, three peaks at 47.4°, 51.6°, and 56.4° match with plane (110), (103), and (112) of the ZnS hexagonal structure. These three peaks became more intense with increasing reaction time. Besides, in the pattern of 5-hour reaction, a broad peak appeared at around 28°, which due to three peaks that matched with plane (100), (002), and (101) in ZnS hexagonal structure merging together. This peak only presents in the pattern of 5-hour reaction product. It indicates that longer reaction time allows a more complete conversion from phosphide to sulfide and better formation of the ZnS hexagonal structure.

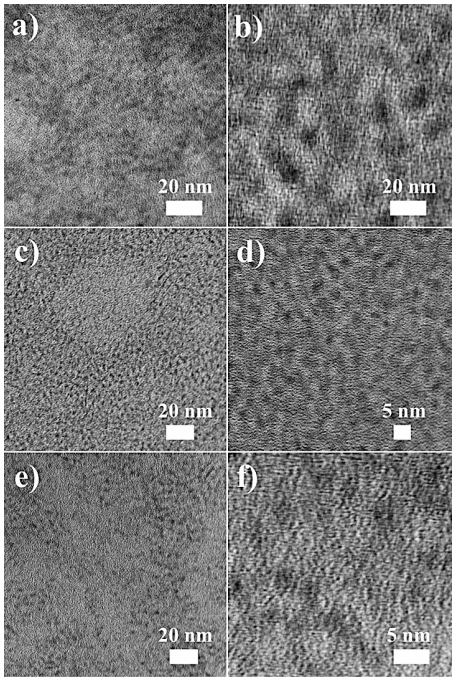

Figure 3.18. TEM images of nanocrystals collected from a), b) 1-hour, c), d) 3-hour, and e), f) 5-hour reactions of Zn_3P_2 nanoparticles and sulfur in oleylamine.

The products were also prepared to take TEM images and showed in Figure 3.18. The left column [(a), (c), and (e)] are low magnification TEM images of nanocrystals generated from 1-hour, 3-hour, and 5-hour reaction that show nanoparticles maintained spherical shape after the conversion reaction. The average size of the as-synthesized nanocrystals was measured to be 4-5 nm from high magnification TEM images [(b), (d), and (f)], which is the same as before the conversion reaction.

Variation of the ratio of zinc to sulfur (Zn:S):

In the systematic study on ratio of Zn to S, both Zn_3P_2 nanoparticles (~4 nm) and large agglomerated Zn_3P_2 clusters (~200 nm) were used as templates. The results indicated that the size of Zn_3P_2 nanoparticles significantly influenced the phosphide → sulfide conversion process.

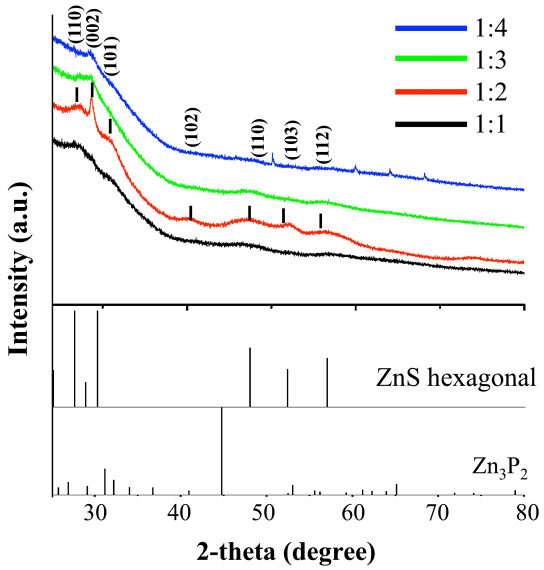

Figure 3.19. Powder XRD patterns of nanocrystals generated from 1-hour reactions with different Zn:S.

Zn_3P_2 nanoparticles were mixed with sulfur with ratio of 1:1, 1:2, 1:3, and 1:4 in oleylamine. After reactions, products were precipitated by isopropanol and collected by centrifugation. Purified products were re-dispersed in toluene to prepare TEM grids (Figure 3.20) and vacuum-dried samples were grinded to powder for XRD tests (Figure 3.19). Nanocrystals produced from reactions with Zn:S as 1:2, 1:3, and 1:4 all have three visible peaks located between 26° to 32° that match with ZnS hexagonal structure. In addition, nanocrystals from 1:1 and 1:2 also show three characteristic peaks that match with peaks corresponding to planes (110), (103), and (112) in ZnS hexagonal structure. TEM images (Figure 3.20) show that nanocrystals were still spherical as before reacting with sulfur.

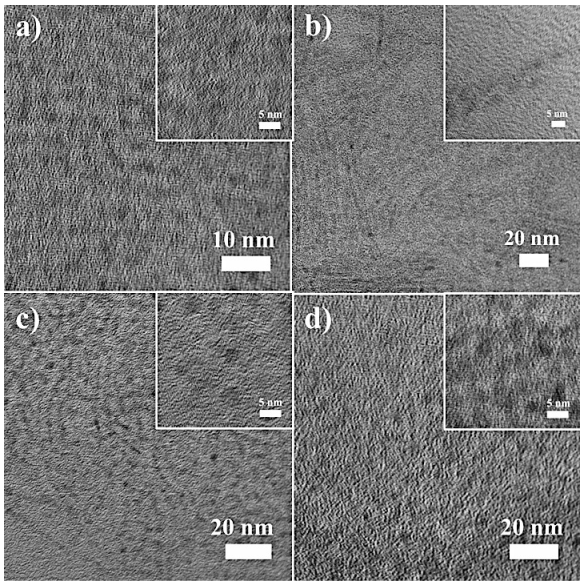

Figure 3.20. TEM images of nanocrystals generated from 1-hour reaction with Zn:S as a) 1:1, b) 1:2, c) 1:3, and d) 1:4. Insert images: high magnification TEM images.

Agglomerated Zn_3P_2 nanoparticle clusters were then used as templates and mixed with sulfur with ratio of 1:6 to 1:18 in oleylamine. After reacting at 140 °C for 1 h, the products were separated and purified. Powder XRD patterns were taken and presented in Figure 3.21. After reacting with low amount of sulfur (1:6 to 1:10), the products remained the majority of the Zn_3P_2 crystal structure. In the XRD pattern of the sample generated from the reaction with Zn:S of 1:6, peaks from 20° to 75° perfectly matched with the original Zn_3P_2 crystal structure. The XRD patterns of the sample from the reaction with Zn:S of 1:8 and 1:10 showed peaks at 27°, 29°, 31°, 32°, 34°, 37°, 41°, 45°, and 53°, which were corresponding to planes (202), (212), (004), (203), (301), (302), (105), (400), and (206) of the Zn_3P_2 crystal structure. At the same time, new peaks from new phases were observed in XRD patterns of these three samples, such as new peaks shown up lower than 25 ° in the XRD patterns of the product from 1:6 reactions including peaks at 7°, 9°, 11°, 14°, and 19°. The peaks below 10° seemed not to match with any structure of $ZnPS_3$ and probably came from polymers formed during the reactions, but peaks at 14° and 19° might come from planes (101) and (111) in $Zn_3(PS_4)_2$ structure (PDF No. 01-072-5951). When the ratio of

sulfur was increased to Zn:S of 1:12, 1:14, 1:16, and 1:18, the only characteristic peak left from Zn_3P_2 structure was located at 45 degree. In order to see features of newly appeared peaks more clear, XRD patterns of products from reactions with Zn:S ratio of 1:12, 1:16, and 1:18 were shown in a separate figure [Figure 21(b)] to compare with the PDF card of the ZnS hexagonal structure. Three broad peaks were located at 47°, 52°, and 57° that matched with ZnS hexagonal structure from planes (110), (103), and (112), respectively. It is possible that Zn_3P_2 was converted to ZnS during the reaction. The softness of Zinc, phosphorus and sulfur is 2~2.5, 0.5, and 2.5, respectively. Zn has more similar softness with sulfur than phosphorus, which could be the reason why Zn_3P_2 converted to ZnS in the presence of excess sulfur in reactions.

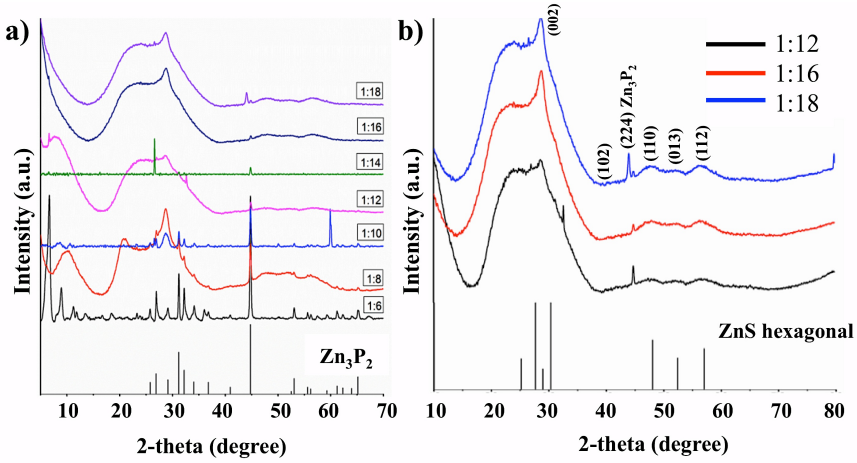

Figure 3.21. Powder XRD data of products collected from 1-hour reactions at 140 °C with Zn to S ratios ranging from (a) 1:6 to 1:18 and (b) 1:12, 1:16, and 1:18.

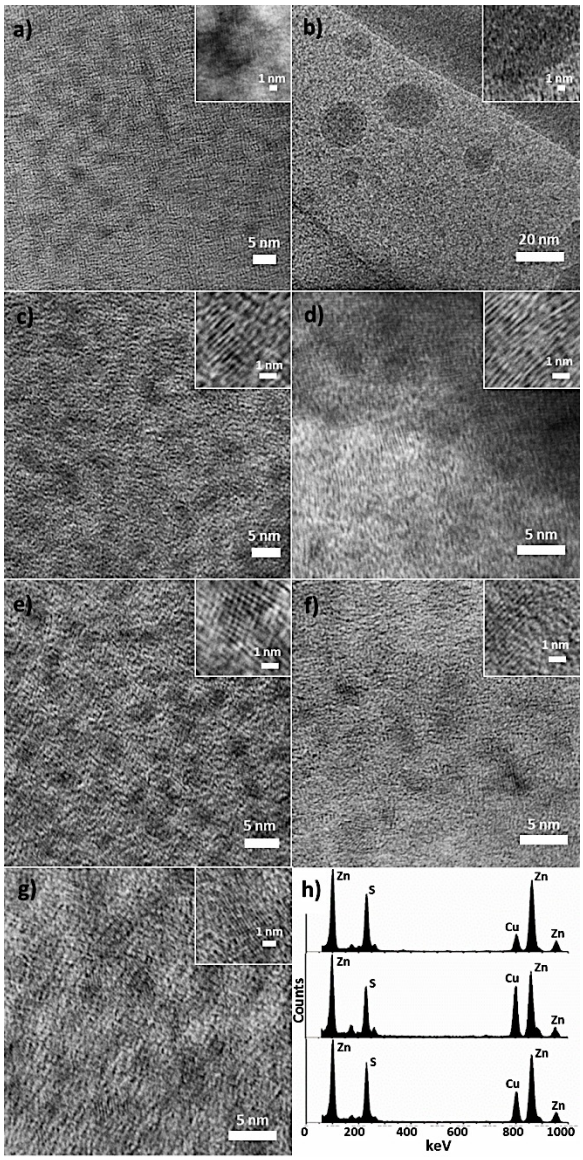

Figure 3.22. TEM images of products from 1-hour reaction at 140 °C with different Zn to S ratio: (a) 1:5, (b) 1:6, (c) 1:8, (d) 1:10, (e) 1:14, (f) 1:16, and (f) 1:18. Insets were HRTEM images. EDS spectra of (e), (f), and (g) were shown in (h) from top to bottom.

TEM images of nanocrystals generated from reactions with different ratio of Zn:S are presented in Figure 3.22. Nanoparticles were spherical in shape and ranged in size from 3 to 5 nm with an exception of in nanoparticles from reaction with Zn:S of 1:6 [Figure 3.22 (b)], which contains bigger particles (15 to 20 nm). The inset images show clear lattice fringes and indicate that all

products still have crystal structures. The lattice spacing was measured to be 0.34 nm from images of TEM from the Zn:S of 1:5 [Figure 3.22 (a)] and 1:8 [Figure 3.22 (c)] samples, which was from the plane (211) in Zn_3P_2 structure (PDF No. 01-074-1156). The lattice spacing was measured to be 0.28 nm from TEM images from the Zn:S 1:6 ratio reaction and it also matched with the plane (203) in Zn_3P_2 structure (PDF No. 01-074-1156). When the sulfur amount was increased to 14 times that of the Zn amount, the lattice spacing was measured to be 0.33 nm, which is corresponding to plane (100) in ZnS hexagonal structure. Both TEM lattice spacing and XRD patterns confirm the presence of ZnS. In samples from Zn:S of 1:16 and 1:18, lattice spacing of 0.31 nm was measured and matched with plane (002) in ZnS hexagonal structure. Figure 3.22 (h) shows EDS spectra of nanoparticles from reactions with Zn:S ratio of 1:14, 1:16, and 1:18. There was no trace of phosphorous. The small peak at 200 was identified as Si, which is attributed to leaching from the glassware during synthesis reaction of Zn_3P_2 from the high temperature and use of corrosive reagents.

Conclusions

Two strategies were utilized to attempt synthesizing zinc sulfophosphide. When ZnS nanocrystal was used as a template in the *in situ* reaction, the original ZnS structure was reacted with oleylamine and chlorine anions and resulted in the salt, $Zn(NH_3)Cl_2$. This revealed that it is necessary to eliminate unwanted ions from the system. Sequentially, ZnS nanocrystals with different sizes and shapes were adopted as templates and reacted with n-trioctylphosphine at different temperature and time. Unfortunately, ZnS templates were consumed in the reaction probably due to the highly corrosive solvent and high temperature, but no positive signs of zinc sulfophosphide were observed. In the other strategy, which starts with Zn_3P_2 nanocrystal as template, even though there was no formation of zinc sulfophosphide, a conversion from Zn_3P_2 to ZnS was observed. The conversion reaction did not affect the size or shape of the nanoparticles.

This inter-conversion between phosphide to sulfide was ever observed for the first time and is likely result from an uncommon anion exchange mechanism.

CHAPTER IV

SOLUTION-BASED EX-SITU SYNTHESIS OF GENERATING GOLD-NICKEL INTERMETALLIC NANORODS

Introduction

Among noble metal nanomaterials, gold nanoparticle is one of the most well studied materials due to their unique optical properties and has been used in various applications.[168] Upon interacting with photons, the electrons in the conduction band are excited to generate a series of oscillation that is called Localized Surface Plasmon Resonance (LSPR).[169] Rod-shaped gold nanoparticles have an anisotropic shape so that the oscillation may occur along the short axis resulting in transverse band as well as the long axis resulting in longitudinal band.[170] These two bands can be observed in the UV-Vis spectra. In the spectra, the transverse peaks normally located in visible region at 520 nm.[171] The longitudinal peak appears in near infrared (NIR, 600-1100 nm) region and the location can be effected by the size and the aspect ratio of nanorods.[172]

Up to the present time, gold nanorods have been synthesized by several methods, such as electrochemical method, chemical reduction, galvanic replacement, and the seed-mediated growth method.[173] The seed-mediated growth method was firstly reported in 1989 by Wiesner and Wokaun.[174] Their protocol started from preparing gold nucleus by reducing Au (III), followed by growing in $HAuCl_4$ solution with a couple drops of H_2O_2. In 2000s, Jana and Murphy further developed the seed-mediated method and successfully generating uniform nanospheres and

nanorods.[175] Since then, this method has become the most popular synthetic strategy due to the ease in controling the shape and size of gold nanoparticles, simplicity of the procedure and technique, and relatively low cost.[176] The resultant gold nanoparticles using this procedure are usually synthesized in aqueous media and stabilized by surface ligands, such as CTAB bi-layers.[177] However, the CTAB molecules have high cytotoxicity and are only stable in the aqueous phase, which greatly restricted the utilization.[178] Thus, it is crucial to replace the initial ligands and functionalize the surface of gold nanorods in order to fulfill certain multifunctional requirements.[179] The most widely used organic group is thiol group due to the strong covalent bond formed between Au and S that can efficiently stabilize gold nanorods and reduce cytotoxicity.[180] A common surface functionalization strategy is phase transfer ligand exchange, which involves both aqueous and organic phases. For example, dodecanethiol (DDT) is a hydrophobic compound that forms Au-S on gold nanorods surface and stabilizes gold nanorods in organic solution.

In the metallic material family, alloys, which contain two or more types of metal atoms, often possess a broad range of properties due to synergistic effects.[181] Alloys have drawn great attention and have been adopted in widespread applications in engineering, electronics, and catalysis.[182-183] In industry, the traditional alloying procedures involve melting two or more metals together, which requires high temperature and pressure as well as heavy-duty equipment.[184]

On the scale of nanometers, however, the superior phase miscibility enables the combining and mixing of different metal components at mild conditions to yield intermetallic or multimetallic alloys.[185-186] Moreover, the tunable structures and controllable morphology at the nanoscale allow the manipulation of properties.[187-188] Intermetallic nanoparticles are the most common alloy nanomaterials.[189] So far, many intermetallic nanomaterial systems with different metallic compositions have been produced.[190] For instance, gold-based intermetallic nanoparticles

(Au_xM_y, M = transition metals), including AuAg,[191] Au_3Pd,[192] Au_3Cu,[193] $AuCu_3$,[194] etc, are some of the most well studied intermetallic nanomaterial systems.

Here, we report a novel shape-controlled synthetic procedure of producing Au_3Ni intermetallic nanorods with the $L1_2$ superlattice structure. Instead of using conventional one-pot hot injection reactions, which make it difficult to control shape and size, we demonstrate a ligand exchange method that can evenly disperse pre-made gold nanorods in organic solvent as well as sustain the shape and size of particles.

Materials

Hexadecyltrimethylammonium bromide (CTAB, ≥ 99.0%), sodium borohydride ($NaBH_4$, 99.99%), gold chloride hydrate ($HAuCl_4 \cdot 3H_2O$, 99.995%), silver nitrate ($AgNO_3$, ≥ 99.0%), L-ascorbic acid (20-200 mesh, ≥ 98%), oleylamine (technical grade, 70%), dioctyl ether (99%), iron (III) acetylacetonate [$Fe(acac)_3$, 97%], nickel (II) acetylacetonate [$Ni(acac)_2$, 95%], and cobalt (III) acetylacetonate [$Co(acac)_3$, 99.99%] were purchased from Sigma. All chemicals were use as arrival without further purification.

Experimental

Preparation of gold nanorods (AuNRs)[175]: A previously published seed mediated method is used with slight modifications. All solutions were prepared in deionized water. The gold seed solution was prepared by mixing the CTAB solution (5 mL, 0.2 M), $HAuCl_4 \cdot 3H_2O$ solution (5 mL, 0.0005 M), and ice cold $NaBH_4$ solution (0.6 mL, 0.01M) followed by aging at 37-40 °C for 2 h. The seed solution appeared to be dark brown and clear. A growth solution was prepared by adding a freshly made ascorbic acid solution (0.0788M) to a mixture solution containing CTAB (0.2 M), $HAuCl_4 \cdot 3H_2O$ (0.001M), and $AgNO_3$ solution (0.004 M). The mixture turned from orange to colorless upon adding ascorbic acid, which indicated Au^{3+} ions were reduced to Au^{1+}. Sequentially, an appropriate amount of as-prepared seed solution was slowly added to the growth

solution. After aging at 37-40 °C for 24 h, the solution appeared to be blue and purified with deionized water.

Preparation of gold nanostars (AuNStars): The method employed to make gold nanostars was slightly modified from a previously published procedure. All solutions were prepared with deionized water. $HAuCl_4 \cdot 3H_2O$ solution (0.36 mL, 0.01M) was added to 10 ml deionized water in a 15-mL centrifuge tube, which was placed on a vortex. $AgNO_3$ solution (20 μL, 0.01M) was added drop-wise to the centrifuge tube while vortexing. After vortexing 15 s, ascorbic acid solution (60 μL, 0.1M) was added to the centrifuge tube while vortexing. After another 20 seconds, as a sign of AuNStars formation, the solution in the centrifuge tube turned to blue. Warm CTAB solution (5 mL, 0.1M) was quickly added to the centrifuge tube to stabilize the AuNStars. Afterwards, the particles were centrifuged and purified with deionized water.

Ligand exchange: After purification, gold nanoparticles (including nanorods and nanostars) were stabilized by CTAB bilayers, which could be replaced by oleylamine using a phase transfer ligand exchange method. In a glass vial, 4 mL of acetone was added to 1 mL of oleylamine to yield a 20% diluted oleylamine solution. Gold nanoparticle water dispersion was transfered to the oleylamine-acetone solution, which resulted in two visible layers immediately. After settling for 10-15 min, a bluish purple organic layer containing gold nanoparticles coated by oleylamine (denoted by “AuNRs@oleylamine” or “AuNStars@oleylamine) was on the top, while a white and cloudy aqueous layer was in the bottom (Figure 4.1). The oleylamine coated gold nanoparticles were separated by centrifuging the top layer and could be re-dispersed in dioctyl ether with brief sonication.

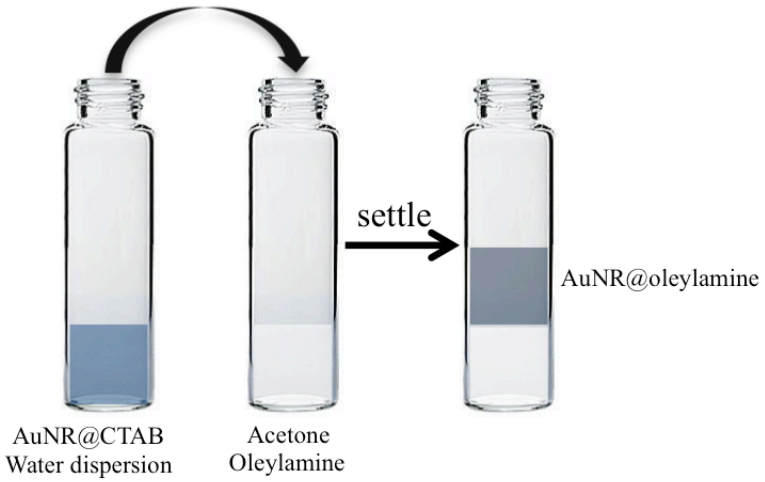

Figure 4.1. A scheme of phase transfer ligand exchange.

Diffusion reactions with 3d transition metals: Figure 4.2 shows the experimental setup of the reaction. In a 50 mL 3-neck flask, AuNRs@oleylamine and $Ni(acac)_2$ (or Fe, Co) were dispersed in dioctyl ether to form dark blue solution, which was heated to 100 °C under argon and kept at the same temperature for 1 h to remove moisture, oxygen, as well as low boiling point impurities. In a 100 mL 3-neck flask, dioctyl ether was heated to 100 °C and kept at the same temperature for 1 h, which was followed by injecting n-butyl lithium. Sequentially, inject the solution containing AuNRs and $Ni(acac)_2$ to the 100 mL flask. The mixture was heated to 250 °C and kept at the same temperature for different amount of time. The solution was cooled to room temperature after the reaction and the product was collected and washed with ethanol several times.

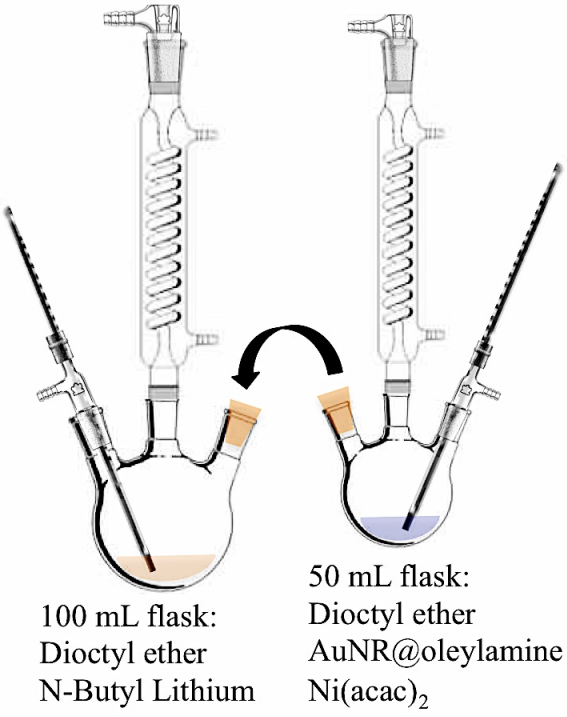

Figure 4.2. A diagrammatic image of the experimental setup.

Characterization

The crystal structure was characterized by X-ray diffraction (XRD) using a Rigaku SmartLab X-ray diffractometer (Cu Kα radiation). The samples were prepared by grinding vacuum-dried samples on glass slides. The morphology of particles was studied by using a JEOL-JEM transmission electron microscope (TEM) operating at an accelerating voltage of 200 kV. The TEM samples were prepared by casting ethanol nanoparticles dispersion onto carbon coated copper grids. The dimension of nanoparticles was measured by the ImageJ and the aspect ratio was calculated as the ratio of length to width. Fourier-transform infrared (FTIR) spectra were taken on a Nicolet iS50 ATR-FTIR spectrometer to identify ligands on particles. UV-Visible spectra were taken on a DU 530 Beckman Colter UV-Visible spectrophotometer.

Result and discussion

AuNRs were synthesized using a seed-mediated method that has been published elsewhere with slight modification. In the step of preparing seed solution, $NaBH_4$ was used as a strong reducing agent to reduce Au^{3+} ions to Au^0 ions, which formed gold nanospheres and were used as seeds. After the seeds were added to growth solution, Au^{1+} ions deposited onto the surface of gold nanospheres and started growing. At certain point, due to underpotential deposition,[195-196] Ag^+ ions gathered on Au [10] facet and resulted in a monolayer that inhibits the growth of these facets. Therefore, $AgNO_3$ acts as a shape-tuning agent during gold nanoparticle growing process. In addition, CTAB molecules acted as surface stabilizers and formed bilayers on the nanoparticle surface due to van de Waals interaction.

Characterization of gold nanoparticles and ligand exchange

Typically, due to the special rod-shape, AuNRs show two absorption bands in the ultraviolet-visible (UV-Vis) spectra because the electron oscillation may take place along two directions while interacting with light (photons). Figure 4.3 shows the UV-visible spectra of as-prepared AuNRs before and after purification with deionized water. Two peaks are present in the spectrum. The one located at 520 nm is attributed to transversal surface plasmon resonance (TSPR), which is due to the electron oscillations along short axis. While the other one is located between 660 to 680 nm, which resulted from electrons oscillating along the long axis, also known as longitudinal surface plasmon resonance (LSPR). Two curves overlapped, which means centrifuge and purification process did not change the shape, size of AuNRs, or cause any agglomerations.

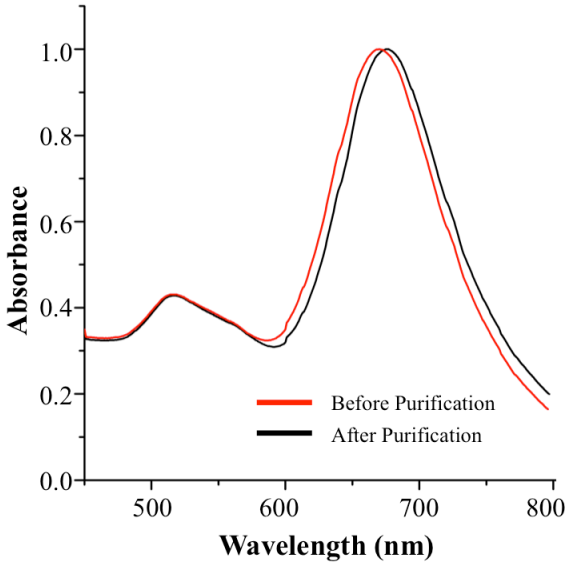

Figure 4.3. UV-visible spectra of AuNR before (red) and after (black) purification with deionized water.

After ligand exchange, UV-Vis spectra and TEM images were taken again to ensure there was no change in morphology or agglomerations. The samples for UV-Vis were prepared by re-dispersing purified AuNR@CTAB in deionized water or purified AuNR@oleylamine in acetone with brief sonication. Figure 4.4a presents the UV-Vis spectra of gold nanorods coated by CTAB and oleylamine. Compared with the spectrum of AuNR@CTAB, the LSPR peak was significantly broadened and shifted to lower wavelength (650 nm). This blue shift may be caused by using acetone, which has lower polarity than water, as a solvent to disperse AuNR@oleylamine. In the case of gold nanostars, there is only one peak in the spectrum of AuNR@CTAB (figure 4.4b). After ligand exchange, this peak was broadened, which is consistent with AuNR. However, a red shift could be observed, which is likely caused by the reduction of particle size.

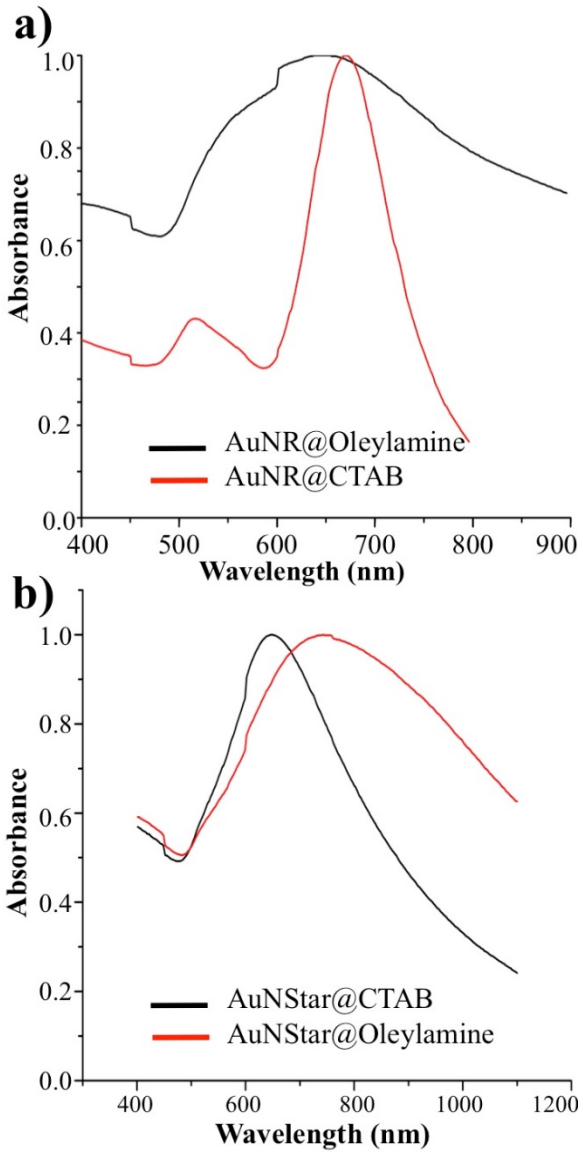

Figure 4.4. UV-Visible spectra of a) AuNR and b) AuNStars coated by CTAB in water and oleylamine in acetone.

Figure 4.5a and 4.5b show the TEM images of gold nanorods before and after ligand exchange. Before the ligand exchange, AuNR@CTAB was measured to be 50.8 ± 4.1 nm in length and 20.2 ± 2.4 nm in width. The aspect ratio of the AuNR@CATB is 2.43 - 2.60. After the ligand exchange, the AuNR@oleylamine has length of 49.8 ± 4.4 nm and width of 19.3 ± 2.9 nm. The aspect ratio the AuNR@oleylamine is 2.44 - 2.76. No change in size, shape or any

agglomerations seen in the images. For the gold nanostars (Figure 4.5c & d), size seems to be the same after the ligand exchange and the morphology does not pose any significant change. The shrinkage of the particles is likely what caused the red shift observed in UV-vis spectra.

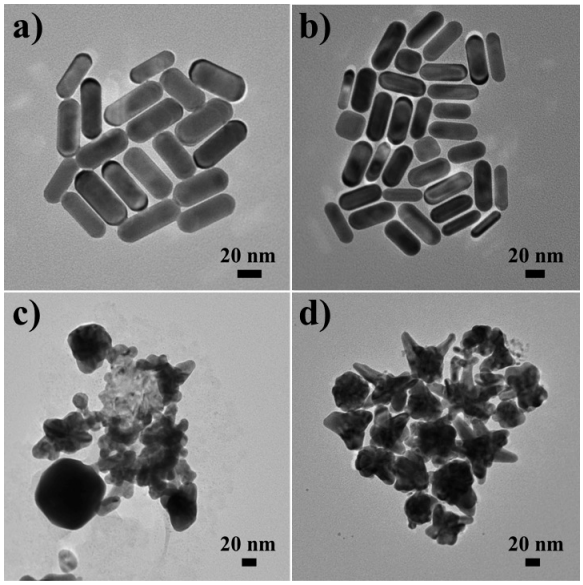

Figure 4.5. TEM images of AuNR coated by a) CTAB, b) oleylamine and AuNStar coated by c) CTAB, d) oleylamine.

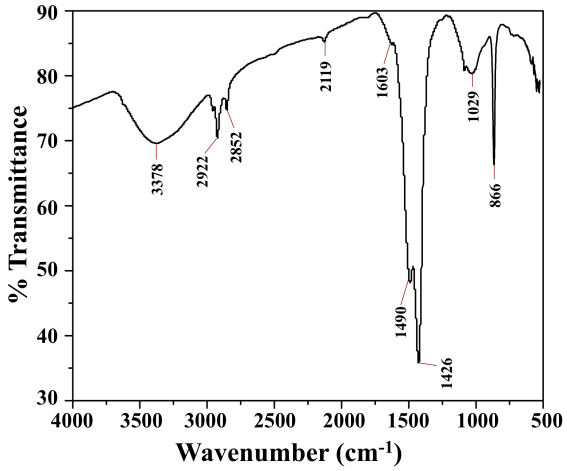

Figure 4.6. FTIR spectrum of oleylamine coated gold nanorods.

Fourier-transform infrared (FTIR) spectrum of gold nanorods after ligand exchange is presented in Figure 4.6. The spectrum shows a broad peak at 3378 cm^{-1} and a small peak at 1603 cm^{-1} that come from $–NH_2$ asymmetric stretching and scissoring modes. Two peaks at 2921.93 cm^{-1} and 2852 cm^{-1} are symmetric and asymmetric stretching vibrations bands of CH_2 and CH_3. Another peak at 1490 cm^{-1} is C-H bending mode. Two peaks at 1426 cm^{-1} and 1029 cm^{-1} can be attributed to C-N stretching and bending vibration modes. Compared to free amine (1000-1350 cm^{-1}), the blue shift is likely caused by the interaction of Au and N. Additionally; the alkene group in the oleylamine molecule also shows a band at 866 cm^{-1} in the spectrum. Moreover, it is worth noting that the N-H stretching band (3017 cm^{-1}) and halogen vibration band (500-700 cm^{-1}) were no longer present, which belong to the CTAB molecule. This indicates CTAB molecules have been completely removed during the ligand exchange process and the surface of gold nanorods stabilized by oleylamine.

To prepare TEM samples, the products were first purified by ethanol 2-3 times and re-dispersed in ethanol with brief sonication. A 0.4 μL dispersion was added onto a carbon coated filmed copper grid and dried under vacuum. Figure 4.7 (a) and (b), (d) and (e), (g) and (h), and (j) and (k) are TEM images for gold nanorods after reacting with $Ni(acac)_3$ for 0.5 h, 1.0 h, 1.5 h, and 2.0 h with Au:Ni=2:1, respectively. Compared with pure gold nanorods in Figure 4.5, all four samples are able to maintain the rod-shape, which indicates oleylamine molecules on gold nanorods surface acted as surface stabilizer and protected nanorods from being etched or collapsing. The sizes of nanorods did not change significantly and measured to range from 45 to 55 nm after reacting with $Ni(acac)_3$. The EDS spectra of nanorods collected after 0.5-, 1.0-, 1.5-, and 2.0-hour reactions can be seen in Figure 4.7 (c), (f), (i), and (l), respectively. Traces of Ni can be observed and with the increasing reaction time from (c) to (l), the amount of Ni in samples is also increasing. This results show that longer reaction times might be necessary to allow Ni atoms to diffuse into the gold.

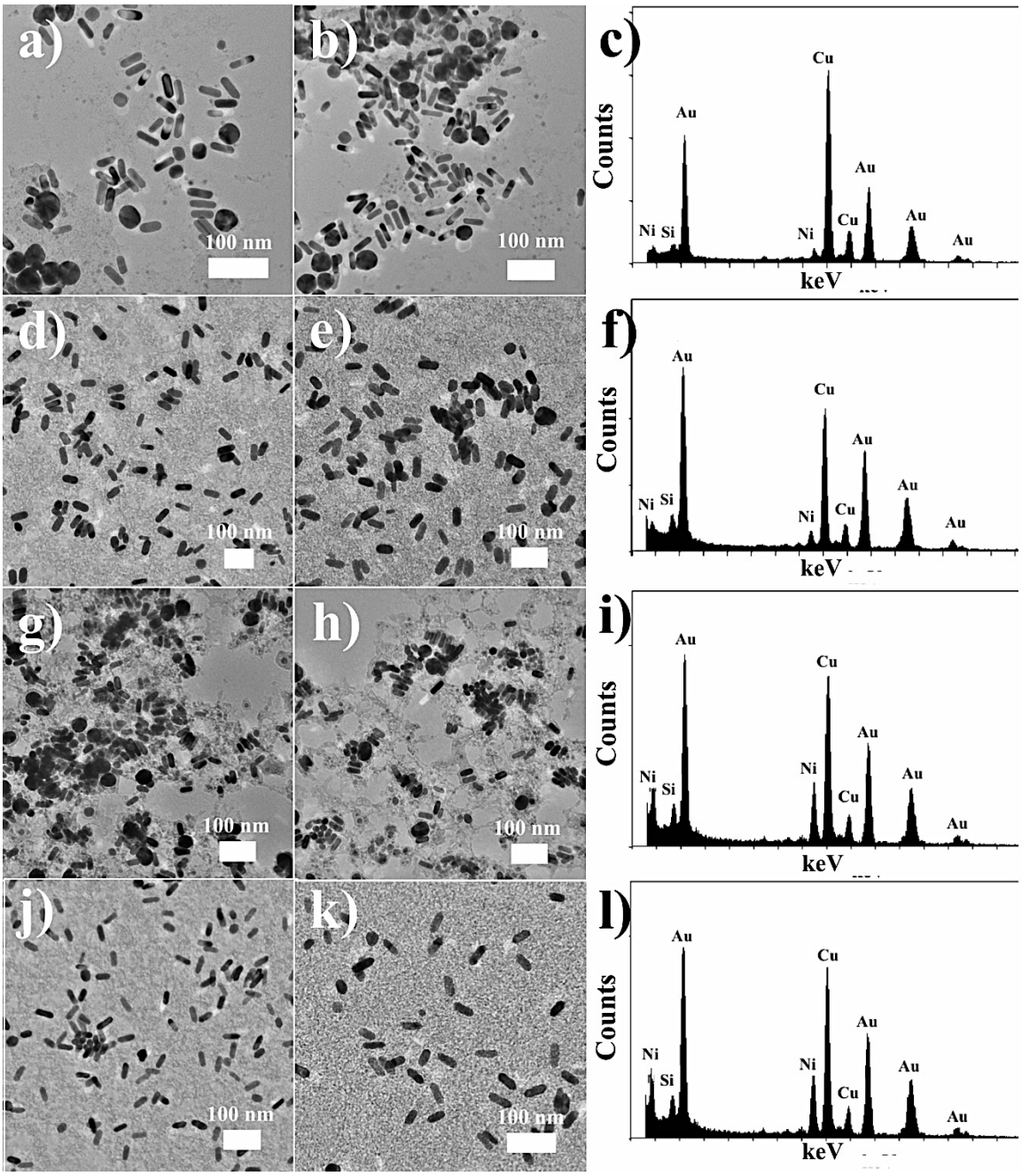

Figure 4.7. TEM images of AuNi nanorods after a) & b) 0.5 h, d) & c) 1 h, g) & h) 1.5 h, and j) & k) 1.75 h reactions. EDS spectra show elemental analysis of AuNi nanorods produced from c) 0.5 h, f) 1 h, i) 1.5 h, and l) 1.75 h reactions.

The products were also dried under vacuum for powder XRD experiments.

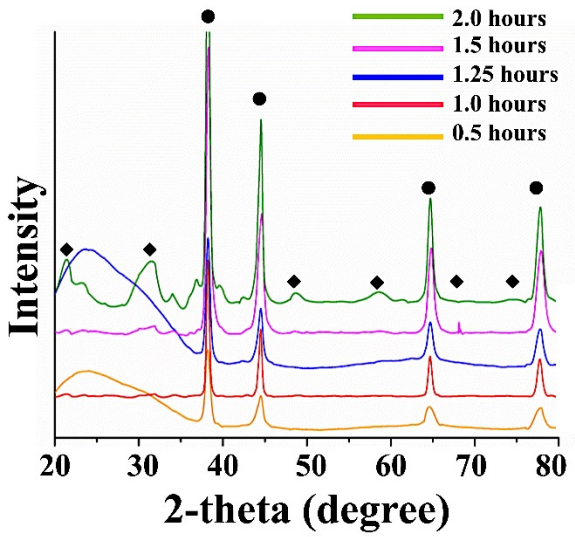

Figure 4.8. Powder XRD patterns of products collected from reactions with 2:1 Au to Ni mole ratio (Dots: diffracting peaks of gold face center cubic structure. Diamonds: $L1_2$ super lattice diffracting peaks)

After the reactions, the purified products were either directly dried on cleaned glass slides or dried in centrifuge tubes and grinded to powder to limit oriented attachment. The XRD patterns were shown in Figure 4.8. All of the samples exhibit distinct peaks at 38.1°, 44.3°, 64.5°, and 77.7° denoted by dots, which correspond to the planes (111), (200), (220), and (311) of the face center cubic structure. It is also worth noting that, with increasing reaction time, these four peaks are slightly shifted to the higher reflection angles by 1 to 2 degree. This shift is due to the lattice spacing shrinking that results from the substitution of the corner gold atoms of the face center cubic by smaller nickel atoms (Figure 4.9). The cubic structure on the right in Figure 4.9 shows the $L1_2$ cubic after Ni atoms replaced Au atoms on the corner. It can be calculated that there is 1 Ni atom ($8\times\frac{1}{8}$) and 3 Au atoms ($6\times\frac{1}{2}$) in each unit cell that leads to Au_3Ni formula. The inserted Ni atoms form new planes in the crystal structure and as a result, new peaks can be observed in the XRD patterns. In Figure 4.8, the XRD pattern of the nanocrystals generated from 2-hour reaction shows 6 new peaks denoted by diamonds are corresponding to plane (100), (110), (210),

(211), (221), and (310) of $L1_2$ cubic structure that resulted from the replacement of Au by Ni atoms. However, these peaks only started showing up after reacting for 1.5 to 2 h. This result agrees with the EDS spectra in Figure 4.7. Reacting for less than 1.5 h did not result in the formation of the $L1_2$ intermetallic nanorods. Compared with the reactions of synthesizing Au_3Ni nanoparticles, the requirement of longer reaction time might be due to the larger dimensions of the initial Au nanorods templates compared to the published procedure for Au_3Ni nanoparticles.[197]

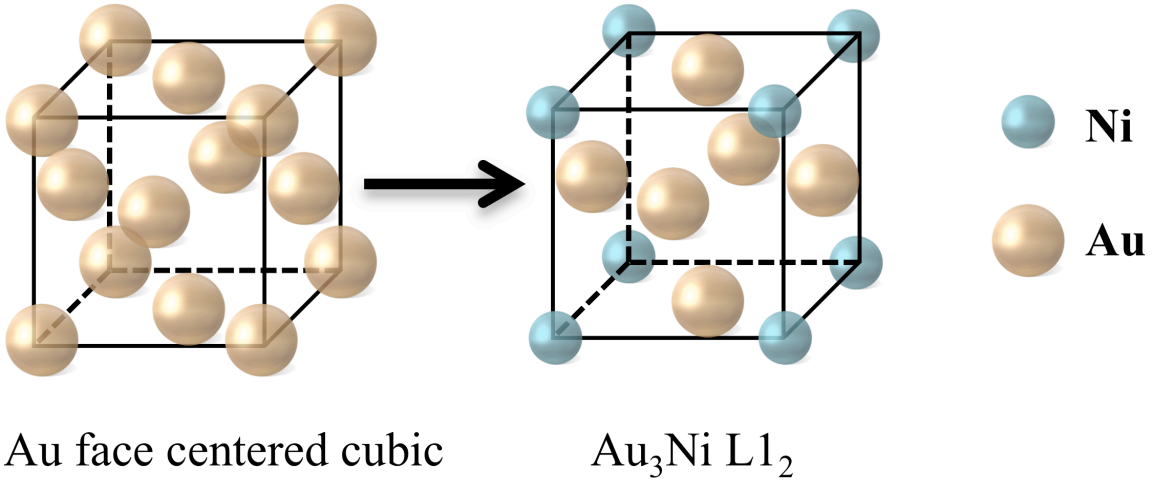

Figure 4.9. A scheme of conversion of Au face centered cubic to Au_3Ni $L1_2$ cubic structure. A unit cell of Au is on the left and yellow spheres represent Au atoms. the unit cell on the right, Ni atoms, which are blue spheres, replaced Au atoms on the corners and the resultant structure is $L1_2$ cubic.

After Au nanorods reacting with $Ni(acac)_3$ for different time with 1:1 mole ratio of Au/Ni, the purified products were tested by TEM. Figure 10 (a) to (e) represent TEM images of generated nanorods after 0.5 h, 1.0 h, 1.5 h, 2.0 h, and 3.0 h, respectively. Most particles still maintain the rod-shape with the same size and no agglomeration was formed even after being kept at high temperature for 3 h. This coincides well with Figure 7, due to the surface stabilizer oleylamine.

However, EDS spectra of samples from 1.0-, 2.0-, and 3.0- hour reactions in Figure 10 (f) show no signal of Ni. It is not likely that Ni atoms have successfully diffused into the Au nanorods. In order to further confirm this hypothesis, powder XRD patterns were taken to exam the crystal structure shown in Figure 4.11.

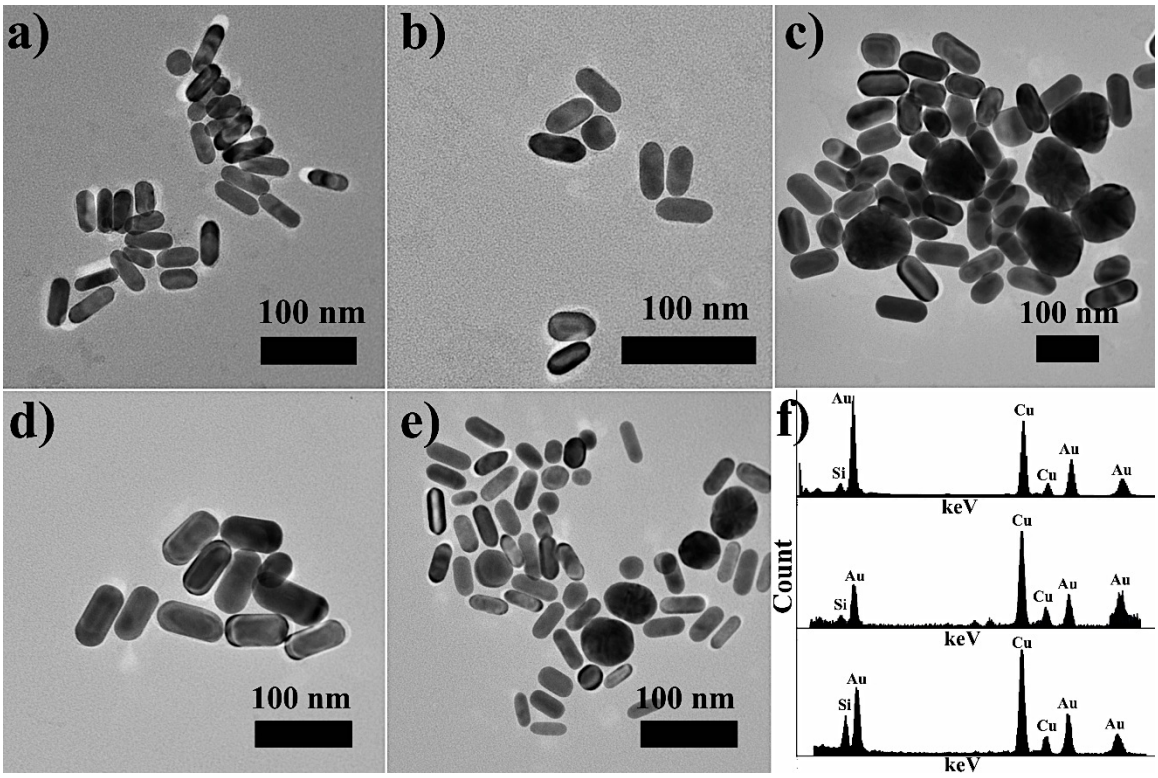

Figure 4.10. TEM images of nanorods produced from reaction with 1:1 mole ratio of Au/Ni for (a) 0.5 h, (b) 1.0 h, (c) 1.5 h, (d) 2.0 h, and (e) 3.0 h. (f) EDS spectra of sample from 1 hour- (top), 2 hour- (middle), and 3- hour (bottom) reactions.

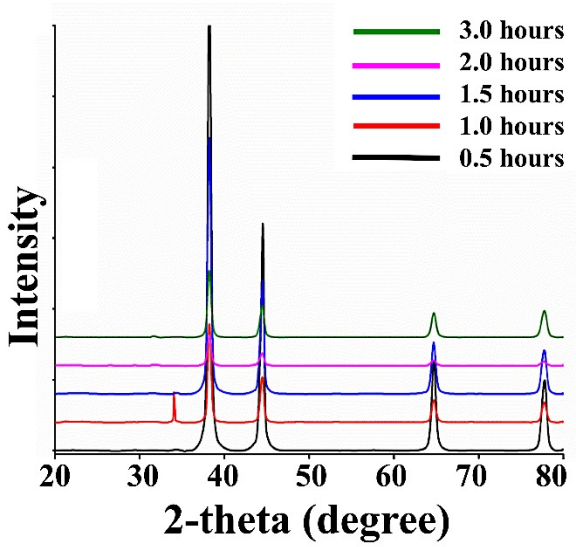

Figure 4.11. Powder XRD patterns nanorods produced by reactions with 1:1 mole ratio of Au/Ni.

In Figure 4.11, all patterns clearly match with face centered cubic structure of Au. Even after long reaction time, no sign of the formation of complete $L1_2$ cubic structure and it indicates that the majority was still pure Au nanorods. A sharp peak at around 33° appears in the pattern of sample from 1-hour reaction, which is more likely to be an impurity. There are two insignificant peaks can be observed at 31° that might be from the (110) plane of $L1_2$ structure.

Conclusions

In this study, Au nanorods were successfully generated using a seed mediated method in aqueous solution and stabilized by a bi-layer ligand, CTAB. UV-Vis spectroscopy can be used to characterize the optical property and the shape. The CTAB molecules on the nanorod surface can be problematic due to the low hydrophobicity and low thermal stability. Oleylamine can be used as an alternative stabilizer on Au nanorod surface to improve the stability and solubility in organic solvent. The replacement of CTAB with oleylamine can be achieved by a phase transfer ligand exchange method. Sequentially, the oleylamine coated Au nanorods reacted with Ni under

high temperature. The TEM images shown that oleylamine as a surface ligand was able to protect the rod-shape from crashing and prevent any agglomeration from forming.

According to the results of systematic studies on reaction time and Au/Ni mole ratio, the Au_3Ni $L1_2$ superlattice crystal structure was produced when the ratio of Au/Ni was 2:1 and the reaction was kept at high temperature for at least 1.5 h. It reveals that in diffusion reactions, it is important to find the appropriate mole ratio of metals as well as the best reacting temperature and time.

CHAPTER V

SUMMARY, CONCLUSIONS, AND FUTURE WORK

Chapter II focuses on fabrication of ZnO nanorods and ZnO/ZnS core/shell nanorods coated cotton fabrics and the application as potential flame retardant materials. ZnO nanorods were grown on the surface of pre-cleaned cotton fabrics using a multi-step hydrothermal procedure. The length of ZnO nanorods and the thickness of nanorod coatings can be controlled by altering the growing time. ZnO nanorods were partially converted to ZnS through a sulfidation process in Na_2S solution to yield ZnO/ZnS nanorods with the core/shell structure. Commercially available ZnO and ZnS microparticles coated cotton fabrics were prepared using a dip coating method as comparison. The flame retardant properties were tested by a cone calorimeter and a vertical flame test. The results show all nanorod and microparticle coatings were able to reduce the heat release rate and total smoke release of cotton fabrics during the combustion. In addition, ZnO and ZnO/ZnS nanorod coatings have better effect than microparticle coatings on improving the flame retardancy and slowing down the spreading of combustion. However, none of the coatings exhibit self-extinguishing properties, as demonstrated by the test results of vertical flame tests. Therefore, the coatings can be further modified by incorporating other flame retardant materials, in order to reinforce the self-extinguishing properties.

In Chapter III, our original goal was to explore synthetic strategies of generating a new semiconductor nanomaterial, zinc sulfophosphide ($Zn_2P_2S_6$). Two strategies were designed and

carried out. Firstly, ZnS nanoparticles with different size and shape were prepared using previously established protocols. The as-prepared ZnS nanoparticles were utilized as templates and reacted with a phosphorous source, trioctylphosphine. However, the reactions under various reaction temperature and time showed no sign of the formation of $Zn_2P_2S_6$. In the second strategy, Zn_3P_2 nanoparticles were generated and used as templates to react with sulfur sources. Systematical studies on reaction time, temperature, ratio of Zn to S, and size of Zn_3P_2 nanoparticles were carried out. The XRD results of the resultant products show no formation of $Zn_2P_2S_6$. Interestingly, a conversion of Zn_3P_2 to ZnS was observed. While reacting with sulfur source, Zn_3P_2 quantum dots can be readily converted to ZnS over 130°C for 1 h with a small amount of sulfur. When the large Zn_3P_2 particles were used as template, it required larger amount of sulfur in the reaction to result in a more complete conversion. In the future, the reaction condition can be further optimized to potentially generate Zn_3P_2@ZnS core/shell nanoparticles.

In Chapter IV, a synthetic procedure for preparing Au_3Ni intermetallic nanorods with controlled size and shape was reported. Gold nanorods were firstly synthesized by a previously published seed-mediated method with minor modification. The prepared gold nanorods were stabilized by CTAB bilayers and can only be dispersed in hydrophilic solvent. The surface of gold nanorods was functionalized by oleylamine using a phase-transfer ligand exchange method and dispersed in dioctylether, which sequentially reacted with Ni precursor. The XRD results of resultant products show no signal of Au_3Ni structure when 1:1 ratio of Au:Ni was used. However, when the ratio of Au to Ni was increased to 1:2, the products showed superlattice structure of Au_3Ni after reacting for 3 h. No significant change in size or shape was observed with TEM. In this project, the ex-situ reaction reported was able to maintain the size and shape of the original gold nanorods. This strategy can be applied on gold nanoparticles with other shape and size. Ni precursor may be replace by other transition metals to generate different gold-based intermetallic nanoparticles.

REFERENCES

1. Peterson, C. L., Nanotechnology: from Feynman to the grand challenge of molecular manufacturing. *IEEE Technol. Soc. Mag.* **2004,** *23* (4), 9-15.

2. Marcovich, A.; Shinn, T., Socio/intellectual patterns in nanoscale research: Feynman Nanotechnology Prize laureates, 1993—2007. *Soc. Sci. Inf.* **2010,** *49* (4), 615-638.

3. Hayat, M. A., *Principles and techniques of electron microscopy. Biological applications*. Edward Arnold.: London WC1B 3DQ, 1981; p xv + 522pp.

4. Roco, M. C., The long view of nanotechnology development: the National Nanotechnology Initiative at 10 years. *J. Nanoparticle Res.* **2011,** *13* (2), 427-445.

5. Dingley, D., Progressive steps in the development of electron backscatter diffraction and orientation imaging microscopy. *J. Microsc.* **2004,** *213* (3), 214-224.

6. Lee, J.; Mahendra, S.; Alvarez, P. J. J., Nanomaterials in the Construction Industry: A Review of Their Applications and Environmental Health and Safety Considerations. *ACS Nano* **2010,** *4* (7), 3580-3590.

7. Lee, K. P.; Arnot, T. C.; Mattia, D., A review of reverse osmosis membrane materials for desalination—Development to date and future potential. *J. Membr. Sci. Technol.* **2011,** *370* (1), 1-22.

8. Allison, R. R.; Mota, H. C.; Bagnato, V. S.; Sibata, C. H., Bio-nanotechnology and photodynamic therapy—State of the art review. *Photodiagnosis Photodyn Ther.* **2008,** *5* (1), 19-28.

9. Kuhlbusch, T. A.; Asbach, C.; Fissan, H.; Göhler, D.; Stintz, M., Nanoparticle exposure at nanotechnology workplaces: A review. *Part Fibre Toxicol.* **2011,** *8* (1), 22.

10. Cevc, G.; Vierl, U., Nanotechnology and the transdermal route: A state of the art review and critical appraisal. *J. Controlled Release* **2010,** *141* (3), 277-299.

11. Karn, B.; Kuiken, T.; Otto, M., Nanotechnology and *in Situ* Remediation: A Review of the Benefits and Potential Risks. *Environ. Health Perspect.* **2009,** *117* (12), 1813-1831.

12. Sanchez, F.; Sobolev, K., Nanotechnology in concrete – A review. *Constr. Build. Mater.* **2010,** *24* (11), 2060-2071.

13. Huang, Z.; Chen, H.; Yip, A.; Ng, G.; Guo, F.; Chen, Z.-K.; Roco, M. C., Longitudinal Patent Analysis for Nanoscale Science and Engineering: Country, Institution and Technology Field. *J. Nanopart. Res.* **2003,** *5* (3), 333-363.

14. Roco, M. C., Nanoscale Science and Engineering: Unifying and Transforming Tools. *AIChE Journal* **2004,** *50* (5), 890-897.

15. Roco, M. C., International strategy for Nanotechnology Research. *J. Nanoparticle Res.* **2001,** *3* (5), 353-360.

16. Broido, D. A.; Malorny, M.; Birner, G.; Mingo, N.; Stewart, D. A., Intrinsic lattice thermal conductivity of semiconductors from first principles. *Appl. Phys. Lett.* **2007,** *91* (23), 231922.

17. Lee, M.-J.; Kim, S. I.; Lee, C. B.; Yin, H.; Ahn, S.-E.; Kang, B. S.; Kim, K. H.; Park, J. C.; Kim, C. J.; Song, I.; Kim, S. W.; Stefanovich, G.; Lee, J. H.; Chung, S. J.; Kim, Y. H.; Park, Y., Low-Temperature-Grown Transition Metal Oxide Based Storage Materials and Oxide Transistors for High-Density Non-volatile Memory. *Adv. Funct. Mater.* **2009,** *19* (10), 1587-1593.

18. Jun, Y.-w.; Choi, J.-s.; Cheon, J., Shape Control of Semiconductor and Metal Oxide Nanocrystals through Nonhydrolytic Colloidal Routes. *Angew. Chem. Int. Ed.* **2006,** *45* (21), 3414-3439.

19. Jin, Z.; Fukumura, T.; Kawasaki, M.; Ando, K.; Saito, H.; Sekiguchi, T.; Yoo, Y. Z.; Murakami, M.; Matsumoto, Y.; Hasegawa, T.; Koinuma, H., High throughput fabrication of transition-metal-doped epitaxial ZnO thin films: A series of oxide-diluted magnetic semiconductors and their properties. *Appl. Phys. Lett.* **2001,** *78* (24), 3824-3826.

20. Alenezi, M. R.; Henley, S. J.; Emerson, N. G.; Silva, S. R. P., From 1D and 2D ZnO nanostructures to 3D hierarchical structures with enhanced gas sensing properties. *Nanoscale* **2014,** *6* (1), 235-247.

21. Kołodziejczak-Radzimska, A.; Jesionowski, T., Zinc Oxide—From Synthesis to Application: A Review. *Mater.* **2014,** *7* (4), 2833.

22. Lee, J.-H.; Ko, K.-H.; Park, B.-O., Electrical and optical properties of ZnO transparent conducting films by the sol–gel method. *J. Cryst. Growth* **2003,** *247* (1), 119-125.

23. Liu, B.; Zeng, H. C., Hydrothermal Synthesis of ZnO Nanorods in the Diameter Regime of 50 nm. *J. Am. Chem. Soc.* **2003,** *125* (15), 4430-4431.

24. Ong, C. B.; Ng, L. Y.; Mohammad, A. W., A review of ZnO nanoparticles as solar photocatalysts: Synthesis, mechanisms and applications. *J. Renew. Sustain. Energy* **2018,** *81*, 536-551.

25. Kaur, M.; Kaur, P.; Kaur, G.; Dev, K.; Negi, P.; Sharma, R., Structural, morphological and optical properties of Eu-N co-doped zinc oxide nanoparticles synthesized using co-precipitation technique. *Vacuum* **2018,** *155*, 689-695.

26. Tso, S.; Li, W.-S.; Wu, B.-H.; Chen, L.-J., Enhanced H_2 production in water splitting with CdS-ZnO core-shell nanowires. *Nano Energy* **2018,** *43*, 270-277.

27. Weiwei, X.; Lingzhi, G.; Xianghua, Z.; Jinpeng, Y.; Hui, H.; Yunqing, C., Improved visible-light photocurrent based on ZnO/ZnS core–shell nanorods via interfacial engineering. *J. Phys. D* **2019,** *52* (3), 035501.

28. Wang, J. X.; Sun, X. W.; Yang, Y.; Huang, H.; Lee, Y. C.; Tan, O. K.; Vayssieres, L., Hydrothermally grown oriented ZnO nanorod arrays for gas sensing applications. *Nanotechnol.* **2006,** *17* (19), 4995.

29. Djurišić, A. B.; Ng, A. M. C.; Chen, X. Y., ZnO nanostructures for optoelectronics: Material properties and device applications. *Prog. Quantum. Electron.* **2010,** *34* (4), 191-259.

30. Gyu-Chul, Y.; Chunrui, W.; Won Il, P., ZnO nanorods: synthesis, characterization and applications. *Semicond. Sci. Techno* **2005,** *20* (4), S22.

31. Yuan, Q.; Hein, S.; Misra, R. D. K., New generation of chitosan-encapsulated ZnO quantum dots loaded with drug: Synthesis, characterization and in vitro drug delivery response. *Acta Biomaterialia* **2010,** *6* (7), 2732-2739.

32. Gao, M.-R.; Jiang, J.; Yu, S.-H., Solution-Based Synthesis and Design of Late Transition Metal Chalcogenide Materials for Oxygen Reduction Reaction (ORR). *Small.* **2012,** *8* (1), 13-27.

33. Hong, Y.; Zhang, J.; Wang, X.; Wang, Y.; Lin, Z.; Yu, J.; Huang, F., Influence of lattice integrity and phase composition on the photocatalytic hydrogen production efficiency of ZnS nanomaterials. *Nanoscale* **2012,** *4* (9), 2859-2862.

34. Fang, X.; Bando, Y.; Liao, M.; Gautam, U. K.; Zhi, C.; Dierre, B.; Liu, B.; Zhai, T.; Sekiguchi, T.; Koide, Y.; Golberg, D., Single-Crystalline ZnS Nanobelts as Ultraviolet-Light Sensors. *Adv. Mater.* **2009,** *21* (20), 2034-2039.

35. Ummartyotin, S.; Infahsaeng, Y., A comprehensive review on ZnS: From synthesis to an approach on solar cell. *Renew. Sust. Energ. Rev.* **2016,** *55*, 17-24.

36. Oyama, S. T., Novel catalysts for advanced hydroprocessing: transition metal phosphides. *J. Catal.* **2003,** *216* (1), 343-352.

37. Zhang, G.; Wang, G.; Liu, Y.; Liu, H.; Qu, J.; Li, J., Highly Active and Stable Catalysts of Phytic Acid-Derivative Transition Metal Phosphides for Full Water Splitting. *J. Am. Chem. Soc.* **2016,** *138* (44), 14686-14693.

38. Bouzara, C.; Kaci, S.; Boukezzata, A.; Kezzoula, F.; Bozetine, I.; Keffous, A.; Trari, M.; Manseri, A.; Menari, H.; Azzouz, R.; Leitgeb, M.; Ouadfel, M.-A.; Talbi, L.; Benfadel, K.; Ouadah, Y., Study of Optical Properties of Nanocrystalline Zinc Phosphide Thin films. *Silicon* **2018**.

39. Glassy, B. A.; Cossairt, B. M., Ternary synthesis of colloidal Zn_3P_2 quantum dots. *Chem. Commun.* **2015,** *51* (25), 5283-5286.

40. Henkes, A. E.; Schaak, R. E., Trioctylphosphine: A General Phosphorus Source for the Low-Temperature Conversion of Metals into Metal Phosphides. *Chem. Mater.* **2007,** *19* (17), 4234-4242.

41. Cortie, M. B.; McDonagh, A. M., Synthesis and Optical Properties of Hybrid and Alloy Plasmonic Nanoparticles. *Chem. Rev.* **2011,** *111* (6), 3713-3735.

42. Homola, J., Present and future of surface plasmon resonance biosensors. *Anal. Bioanal. Chem.* **2003,** *377* (3), 528-539.

43. Eustis, S.; El-Sayed, M. A., Why gold nanoparticles are more precious than pretty gold: Noble metal surface plasmon resonance and its enhancement of the radiative and nonradiative properties of nanocrystals of different shapes. *Chem. Soc. Rev.* **2006,** *35* (3), 209-217.

44. Link, S.; El-Sayed, M. A., Size and Temperature Dependence of the Plasmon Absorption of Colloidal Gold Nanoparticles. *J. Phys. Chem. B* **1999,** *103* (21), 4212-4217.

45. El-Shafei, A.; ElShemy, M.; Abou-Okeil, A., Eco-friendly finishing agent for cotton fabrics to improve flame retardant and antibacterial properties. *Carbohydr. Polym.* **2015,** *118*, 83-90.

46. Poon, C.-k.; Kan, C.-w., Effects of TiO_2 and curing temperatures on flame retardant finishing of cotton. *Carbohydr. Polym.* **2015,** *121*, 457-467.

47. El-Hady, M. M. A.; Farouk, A.; Sharaf, S., Flame retardancy and UV protection of cotton based fabrics using nano ZnO and polycarboxylic acids. *Carbohydr. Polym.* **2013,** *92* (1), 400-406.

48. Cheng, X.; Yang, C. Q., Flame retardant finishing of cotton fleece fabric: Part V. Phosphorus-containing maleic acid oligomers. *Fire Mater.* **2009,** *33* (8), 365-375.

49. Dong, C.; Lu, Z.; Zhang, F.; Zhu, P.; Zhang, L.; Sui, S., Preparation and properties of cotton fabrics treated with a novel polysiloxane water repellent and flame retardant. *Mater. Lett.* **2015,** *152*, 276-279.

50. Neisius, M.; Stelzig, T.; Liang, S.; Gaan, S., 14 - Flame retardant finishes for textiles A2 - Paul, Roshan. In *Functional Finishes for Textiles*, Woodhead Publishing: 2015; pp 429-461.

51. Shafizadeh, F.; Fu, Y. L., Pyrolysis of cellulose. *Carbohydr. Res.* **1973,** *29* (1), 113-122.

52. Haynes, H. J., *Fire loss in the United States during 2014*. National Fire Protection Association. Fire Analysis and Research Division: 2015.

53. Alongi, J.; Bosco, F.; Carosio, F.; Di Blasio, A.; Malucelli, G., A new era for flame retardant materials? *Mater. Today* **2014,** *17* (4), 152-153.

54. Alongi, J.; Camino, G.; Malucelli, G., Heating rate effect on char yield from cotton, poly(ethylene terephthalate) and blend fabrics. *Carbohydr. Polym.* **2013,** *92* (2), 1327-1334.

55. Alongi, J.; Malucelli, G., State of the art and perspectives on sol–gel derived hybrid architectures for flame retardancy of textiles. *J. Mater. Chem.* **2012,** *22* (41), 21805-21809.

56. Brancatelli, G.; Colleoni, C.; Massafra, M. R.; Rosace, G., Effect of hybrid phosphorus-doped silica thin films produced by sol-gel method on the thermal behavior of cotton fabrics. *Polym. Degrad. Stab.* **2011,** *96* (4), 483-490.

57. Alongi, J.; Ciobanu, M.; Malucelli, G., Cotton fabrics treated with hybrid organic–inorganic coatings obtained through dual-cure processes. *Cellulose* **2011,** *18* (5), 1335-1348.

58. Bayramoğlu, G.; Kahraman, M. V.; Kayaman-Apohan, N.; Güngör, A., Synthesis and characterization of UV-curable dual hybrid oligomers based on epoxy acrylate containing pendant alkoxysilane groups. *Prog. Org. Coat.* **2006,** *57* (1), 50-55.

59. Malucelli, G.; Carosio, F.; Alongi, J.; Fina, A.; Frache, A.; Camino, G., Materials engineering for surface-confined flame retardancy. *Mater. Sci. Eng. R-Rep* **2014,** *84*, 1-20.

60. Carosio, F.; Alongi, J., Few durable layers suppress cotton combustion due to the joint combination of layer by layer assembly and UV-curing. *RSC Adv.* **2015,** *5* (87), 71482-71490.

61. Kemmlein, S.; Herzke, D.; Law, R. J., Brominated flame retardants in the European chemicals policy of REACH—Regulation and determination in materials. *J. Chromatogr. A* **2009,** *1216* (3), 320-333.

62. Alaee, M.; Arias, P.; Sjödin, A.; Bergman, Å., An overview of commercially used brominated flame retardants, their applications, their use patterns in different countries/regions and possible modes of release. *Environ. Int* **2003,** *29* (6), 683-689.

63. Salamova, A.; Hermanson, M. H.; Hites, R. A., Organophosphate and halogenated flame retardants in atmospheric particles from a European Arctic site. *Environ. Sci. Technol.* **2014,** *48* (11), 6133-6140.

64. Morgan, A. B.; Gilman, J. W., An overview of flame retardancy of polymeric materials: application, technology, and future directions. *Fire and Mater.* **2013,** *37* (4), 259-279.

65. Horrocks, A. R., Flame retardant challenges for textiles and fibres: new chemistry versus innovatory solutions. *Polym. Degrad. Stab.* **2011,** *96* (3), 377-392.

66. Weil, E. D.; Levchik, S. V., Flame retardants in commercial use or development for textiles. *J. Fire Sci.* **2008,** *26* (3), 243-281.

67. Camino, G.; Costa, L., Performance and mechanisms of fire retardants in polymers—a review. *Polym. Degrad. Stab.* **1988,** *20* (3-4), 271-294.

68. Alongi, J.; Ciobanu, M.; Malucelli, G., Novel flame retardant finishing systems for cotton fabrics based on phosphorus-containing compounds and silica derived from sol–gel processes. *Carbohydr. Polym.* **2011,** *85* (3), 599-608.

69. Kandola, B. K.; Horrocks, A. R., Complex char formation in flame-retarded fibre-intumescent combinations—II. Thermal analytical studies. *Polym. Degrad. Stab.* **1996,** *54* (2-3), 289-303.

70. Horrocks, A. R.; Kandola, B. K.; Davies, P. J.; Zhang, S.; Padbury, S. A., Developments in flame retardant textiles – a review. *Polym. Degrad. Stab.* **2005,** *88* (1), 3-12.

71. Carignan, C. C.; Heiger-Bernays, W.; McClean, M. D.; Roberts, S. C.; Stapleton, H. M.; Sjödin, A.; Webster, T. F., Flame retardant exposure among collegiate United States gymnasts. *Earth Planet. Sci. Lett.* **2013,** *47* (23), 13848-13856.

72. Prival, M. J.; McCoy, E. C.; Gutter, B.; Rosendranz, H. S., Tris(2,3-dibromopropyl) phosphate: mutagenicity of a widely used flame retardant. *Science* **1977,** *195* (4273), 76.

73. van der Veen, I.; de Boer, J., Phosphorus flame retardants: Properties, production, environmental occurrence, toxicity and analysis. *Chemosphere* **2012,** *88* (10), 1119-1153.

74. Xu, L.; Wang, W.; Yu, D., Durable flame retardant finishing of cotton fabrics with halogen-free organophosphonate by UV photoinitiated thiol-ene click chemistry. *Carbohydr. Polym.* **2017,** *172*, 275-283.

75. Alongi, J.; Malucelli, G., Cotton flame retardancy: state of the art and future perspectives. *RSC Adv.* **2015,** *5* (31), 24239-24263.

76. Lam, Y.; Kan, C.; Yuen, C., Effect of zinc oxide on flame retardant finishing of plasma pre-treated cotton fabric. *Cellulose* **2011,** *18* (1), 151-165.

77. Lam, Y.; Kan, C.; Yuen, C., Flame‐retardant finishing in cotton fabrics using zinc oxide co‐catalyst. *J. Appl. Polym. Sci.* **2011,** *121* (1), 612-621.

78. Athauda, T. J.; LePage, W. S.; Chalker, J. M.; Ozer, R. R., High density growth of ZnO nanorods on cotton fabric enables access to a flame resistant composite. *RSC Adv.* **2014,** *4* (28), 14582-14585.

79. Naveed Ul Haq, A.; Nadhman, A.; Ullah, I.; Mustafa, G.; Yasinzai, M.; Khan, I., Synthesis Approaches of Zinc Oxide Nanoparticles: The Dilemma of Ecotoxicity. *J Nanomater.* **2017,** *2017*.

80. Pearce, E., *Flame-retardant polymeric materials*. Springer Science & Business Media: 2012.

81. Ning, Y.; Guo, S., Flame‐retardant and smoke‐suppressant properties of zinc borate and aluminum trihydrate‐filled rigid PVC. *J. Appl. Polym. Sci.* **2000,** *77* (14), 3119-3127.

82. Thomas, N. L., Zinc compounds as flame retardants and smoke suppressants for rigid PVC. *Plast Rubber Compos* **2003,** *32* (8-9), 413-419.

83. Athauda, T. J.; Madduma-Bandarage, U. S.; Vasquez, Y., Integration of ZnO/ZnS nanostructured materials into a cotton fabric platform. *RSC Adv.* **2014,** *4* (106), 61327-61332.

84. Zhao, G.; Guo, Q.; Yi, J.; Cai, X., Synergistic effect of zinc oxide on the flame retardant and thermal properties of acrylonitrile–butadiene–styrene/poly(ethylene terephthalate)/ammonium polyphosphate systems. *J Appl Polym Sci.* **2011,** *122* (4), 2338-2344.

85. Sacristán, M.; Hull, T. R.; Stec, A. A.; Ronda, J. C.; Galià, M.; Cádiz, V., Cone calorimetry studies of fire retardant soybean-oil-based copolymers containing silicon or boron: Comparison of additive and reactive approaches. *Polym. Degrad. Stab.* **2010,** *95* (7), 1269-1274.

86. Nam, W. H.; Lim, Y. S.; Seo, W.-S.; Cho, H. K.; Lee, J. Y., Control of the shell structure of ZnO–ZnS core-shell structure. *J. Nanopart. Res.* **2011,** *13* (11), 5825-5831.

87. Brancatelli, G.; Colleoni, C.; Massafra, M.; Rosace, G., Effect of hybrid phosphorus-doped silica thin films produced by sol-gel method on the thermal behavior of cotton fabrics. *Polym. Degrad. Stab.* **2011,** *96* (4), 483-490.

88. Shariatinia, Z.; Javeri, N.; Shekarriz, S., Flame retardant cotton fibers produced using novel synthesized halogen-free phosphoramide nanoparticles. *Carbohydr. Polym.* **2015,** *118*, 183-198.

89. Torvi, D. A.; Eng, P.; Threlfall, T. G., Heat transfer model of flame resistant fabrics during cooling after exposure to fire. *Fire Technol.* **2006,** *42* (1), 27-48.

90. Volz, S. G.; Chen, G., Molecular dynamics simulation of thermal conductivity of silicon nanowires. *Appl. Phys. Lett.* **1999,** *75* (14), 2056-2058.

91. Wang, Z. L., Zinc oxide nanostructures: growth, properties and applications. *J. Phys. Condens. Matter* **2004,** *16* (25), R829.

92. Weil, E. D.; Levchik, S. V.; Ravey, M.; Zhu, W., A survey of recent progress in phosphorus-based flame retardants and some mode of action studies. *Phosphorus Sulfur* **1999,** *144* (1), 17-20.

93. Mouritz, A.; Mathys, Z.; Gibson, A., Heat release of polymer composites in fire. *Compos. Part A: Appl. Sci. Manuf.* **2006,** *37* (7), 1040-1054.

94. Karaivanona, M.; Gjurova, K., Non‐halogen‐containing flame‐retardant ethylene‐propylene copolymer compositions for cable insulation with nitrogen‐and sulfur‐containing fire retardants. *J. Appl. Polym. Sci.* **1997,** *63* (5), 581-588.

95. Pawelec, W.; Holappa, A.; Tirri, T.; Aubert, M.; Hoppe, H.; Pfaendner, R.; Wilén, C.-E., Disulfides–Effective radical generators for flame retardancy of polypropylene. *Polym. Degrad. Stab.* **2014,** *110*, 447-456.

96. Viczian, I., Földvári, Mária: Handbook of the thermogravimetric system of minerals and its use in geological practice: Occasional Papers of the Geological Institute of Hungary, vol. 213, Budapest, 2011, 180 p. Akadémiai Kiadó, co-published with Springer Science+ Business Media BV, Formerly Kluwer Academic Publishers BV: 2013.

97. Laoutid, F.; Bonnaud, L.; Alexandre, M.; Lopez-Cuesta, J.-M.; Dubois, P., New prospects in flame retardant polymer materials: from fundamentals to nanocomposites. *Mater. Sci. Eng. R Rep.* **2009,** *63* (3), 100-125.

98. Morgan, A. B.; Gilman, J. W., An overview of flame retardancy of polymeric materials: application, technology, and future directions. *Fire Mater.* **2013,** *37* (4), 259-279.

99. Jin, W.; Singh, K.; Zondlo, J., Pyrolysis kinetics of physical components of wood and wood-polymers using isoconversion method. *Agriculture* **2013,** *3* (1), 12-32.

100. Mikkola, J.-P.; Kirilin, A.; Tuuf, J.-C.; Pranovich, A.; Holmbom, B.; Kustov, L. M.; Murzin, D. Y.; Salmi, T., Ultrasound enhancement of cellulose processing in ionic liquids: from dissolution towards functionalization. *Green Chem.* **2007,** *9* (11), 1229-1237.

101. Horrocks, A.; Smart, G.; Hörold, S.; Wanzke, W.; Schlosser, E.; Williams, J., The combined effects of zinc stannate and aluminium diethyl phosphinate on the burning behaviour of glass fibre-reinforced, high temperature polyamide (HTPA). *Polym. Degrad. Stab.* **2014,** *104*, 95-103.

102. Wilkie, C. A.; Morgan, A. B., *Fire retardancy of polymeric materials*. CRC press: 2009.

103. Radlein, D.; Piskorz, J.; Scott, D., Fast pyrolysis of natural polysaccharides as a potential industrial process. *J. Anal. Appl. Pyrolysis* **1991,** *19*, 41-63.

104. Saeman, J. F., Kinetics of wood saccharification-hydrolysis of cellulose and decomposition of sugars in dilute acid at high temperature. *Ind. Eng. Chem. Res.* **1945,** *37* (1), 43-52.

105. Shafizadeh, F.; Bradbury, A. G., Smoldering combustion of cellulosic materials. *J. Build. Phys.* **1979,** *2* (3), 141-152.

106. Cheng, Y.; Lü, C.; Lin, Z.; Liu, Y.; Guan, C.; Lü, H.; Yang, B., Preparation and properties of transparent bulk polymer nanocomposites with high nanophase contents. *J. Mater. Chem.* **2008,** *18* (34), 4062-4068.

107. Zhang, G.; Zhang, J.; Yang, B., Fabrication of polymerizable ZnS nanoparticles in N, N ′ -dimethylacrylamide and the resulting high refractive index optical materials. *Polym. Chem.* **2013,** *4* (14), 3963-3967.

108. Andre, R. S.; Pavinatto, A.; Mercante, L. A.; Paris, E. C.; Mattoso, L. H.; Correa, D. S., Improving the electrochemical properties of polyamide 6/polyaniline electrospun nanofibers by surface modification with ZnO nanoparticles. *RSC Adv.* **2015,** *5* (90), 73875-73881.

109. Feng, Y.; Feng, N.; Wei, Y.; Zhang, G., An *in situ* gelatin-assisted hydrothermal synthesis of ZnO–reduced graphene oxide composites with enhanced photocatalytic performance under ultraviolet and visible light. *RSC Adv.* **2014,** *4* (16), 7933-7943.

110. Yadav, A.; Prasad, V.; Kathe, A. A.; Raj, S.; Yadav, D.; Sundaramoorthy, C.; Vigneshwaran, N., Functional finishing in cotton fabrics using zinc oxide nanoparticles. *Bull. Mater. Sci.* **2006,** *29* (6), 641-645.

111. Zhong, Z.; Xu, Z.; Sheng, T.; Yao, J.; Xing, W.; Wang, Y., Unusual air filters with ultrahigh efficiency and antibacterial functionality enabled by ZnO nanorods. *ACS Appl. Mater. Inter.* **2015,** *7* (38), 21538-21544.

112. Goh, E.; Xu, X.; McCormick, P., Effect of particle size on the UV absorbance of zinc oxide nanoparticles. *Scripta Mater.* **2014,** *78*, 49-52.

113. Uğur, Ş. S.; Sarıışık, M.; Aktaş, A. H.; Uçar, M. Ç.; Erden, E., Modifying of cotton fabric surface with nano-ZnO multilayer films by layer-by-layer deposition method. *Nanoscale Res. Lett.* **2010,** *5* (7), 1204.

114. Li, Z.; Yang, R.; Yu, M.; Bai, F.; Li, C.; Wang, Z. L., Cellular level biocompatibility and biosafety of ZnO nanowires. *J. Phys. Chem. C* **2008,** *112* (51), 20114-20117.

115. Lu, H.; Brutchey, R. L., Tunable Room-Temperature Synthesis of Coinage Metal Chalcogenide Nanocrystals from N-Heterocyclic Carbene Synthons. *Chem. Mater.* **2017,** *29* (3), 1396-1403.

116. Yu, L.; Liu, H., The progress of photoluminescent properties of rare-earth-ions-doped phosphate one-dimensional nanocrystals. *J. Nanomater.* **2010,** *2010*, 1-6.

117. Feng, L.; Xue, H., Advances in Transition-Metal Phosphide Applications in Electrochemical Energy Storage and Catalysis. *Chem. Electro. Chem.* **2017,** *4* (1), 20-34.

118. Shahid, R.; Toprak, M. S.; Soliman, H. M. A.; Muhammed, M., Low temperature synthesis of cubic phase zinc sulfide quantum dots. *Cent Eur J Chem* **2012,** *10* (1), 54-58.

119. Onwudiwe, D. C.; Hrubaru, M.; Ebenso, E. E., Synthesis, structural and optical properties of TOPO and HDA capped cadmium sulphide nanocrystals, and the effect of capping ligand concentration. *J. Nanomater.* **2016,** *16* (1), 305-305.

120. Bhattacharjee, U.; Men, L.; Rosales, B. A.; Alvarado, S. R.; Vela, J.; Petrich, J. W., Using ATTO Dyes To Probe the Photocatalytic Activity of Au–CdS Nanoparticles. *J. Phys. Chem. C* **2017,** *121* (1), 676-683.

121. Niu, J.; Xu, W.; Shen, H.; Li, S.; Wang, H.; Li, L. S., Synthesis of CdS, ZnS, and CdS/ZnS Core/Shell Nanocrystals Using Dodecanethiol. *KCS.* **2012,** *33* (2), 393-397.

122. Kuzuya, T.; Tai, Y.; Yamamuro, S.; Hihara, T.; Peng, D. L.; Sumiyama, K., Synthesis of Zinc Sulfide Nanocrystals and Fabrication of Nanocrystal Superlattice. *Mater. Trans.,* **2004,** *45* (8), 2650-2652.

123. Brus, L., Electronic wave functions in semiconductor clusters: experiment and theory. *J. Phys. Chem.* **1986,** *90* (12), 2555-2560.

124. Li, Y.; Li, X.; Yang, C.; Li, Y., Ligand-Controlling Synthesis and Ordered Assembly of ZnS Nanorods and Nanodots. *J. Phys. Chem. B* **2004,** *108* (41), 16002-16011.

125. Han, Z.; Qiu, F.; Eisenberg, R.; Holland, P. L.; Krauss, T. D., Robust Photogeneration of H_2 in Water Using Semiconductor Nanocrystals and a Nickel Catalyst. *Science* **2012,** *338* (6112), 1321-1324.

126. Kamat, P. V., Semiconductor Nanostructures for Energy Conversion. *ACS Energy Lett.* **2017,** *2* (5), 1128-1129.

127. Pathakoti, K.; Manubolu, M.; Hwang, H.-M., Nanostructures: Current uses and future applications in food science. *J Food Drug Anal.* **2017,** *25* (2), 245-253.

128. Todescato, F.; Fortunati, I.; Minotto, A.; Signorini, R.; Jasieniak, J.; Bozio, R., Engineering of Semiconductor Nanocrystals for Light Emitting Applications. *Mater.* **2016,** *9* (8), 672.

129. Morozov, Y. V.; Draguta, S.; Zhang, S.; Cadranel, A.; Wang, Y.; Janko, B.; Kuno, M., Defect-Mediated CdS Nanobelt Photoluminescence Up-Conversion. *J. Phys. Chem. C.* **2017,** *121* (30), 16607-16616.

130. Nedelcu, G.; Protesescu, L.; Yakunin, S.; Bodnarchuk, M. I.; Grotevent, M. J.; Kovalenko, M. V., Fast Anion-Exchange in Highly Luminescent Nanocrystals of Cesium Lead Halide Perovskites ($CsPbX_3$, X = Cl, Br, I). *Nano Lett.* **2015,** *15* (8), 5635-5640.

131. Razgoniaeva, N.; Carrillo, L.; Burchfield, D.; Moroz, P.; Adhikari, P.; Yadav, P.; Khon, D.; Zamkov, M., Colloidal Synthesis of Monodisperse Semiconductor Nanocrystals through Saturated Ionic Layer Adsorption. *Chem. Mater.* **2016,** *28* (8), 2823-2833.

132. Chen, B.; Pradhan, N.; Zhong, H., From Large-Scale Synthesis to Lighting Device Applications of Ternary I–III–VI Semiconductor Nanocrystals: Inspiring Greener Material Emitters. *J. Phys. Chem. Lett* **2018,** *9* (2), 435-445.

133. Alivisatos, A. P., Semiconductor Clusters, Nanocrystals, and Quantum Dots. *Science* **1996,** *271* (5251), 933-937.

134. Houtepen, A. J.; Hens, Z.; Owen, J. S.; Infante, I., On the Origin of Surface Traps in Colloidal II–VI Semiconductor Nanocrystals. *Chem. Mater.* **2017,** *29* (2), 752-761.

135. Ramalingam, G.; Saravanan, K. V.; Vizhi, T. K.; Rajkumar, M.; Baskar, K., Synthesis of water-soluble and bio-taggable CdSe@ZnS quantum dots. *RSC Adv.* **2018,** *8* (16), 8516-8527.

136. Lee, G.-J.; Wu, J. J., Recent developments in ZnS photocatalysts from synthesis to photocatalytic applications — A review. *Powder Technol.* **2017,** *318*, 8-22.

137. Huang, J.; Yang, Y.; Xue, S.; Yang, B.; Liu, S.; Shen, J., Photoluminescence and electroluminescence of ZnS:Cu nanocrystals in polymeric networks. *Appl. Phys. Lett.* **1997,** *70* (18), 2335-2337.

138. Kobosko, S. M.; Jara, D. H.; Kamat, P. V., AgInS2–ZnS Quantum Dots: Excited State Interactions with TiO_2 and Photovoltaic Performance. *ACS Appl. Mater. Interfaces* **2017,** *9* (39), 33379-33388.

139. Zhang, X.; Zhou, Y.-Z.; Wu, D.-Y.; Liu, X.-H.; Zhang, R.; Liu, H.; Dong, C.-K.; Yang, J.; Kulinich, S. A.; Du, X.-W., ZnO nanosheets with atomically thin ZnS overlayers for photocatalytic water splitting. *J. Mater. Chem. A* **2018,** *6* (19), 9057-9063.

140. Siahmardan, B.; Soleimanian, V.; Varnamkhasti, M. G., Effect of size and shape of crystallites on the optical properties of nanostructured ZnS films. *Mat Sci Semicon Proc* **2017,** *71*, 76-83.

141. Sharma, H. K.; Shukla, P. K.; Agrawal, S. L., Effect of sulphur concentration on the structural and electronic properties of ZnS nanoparticles synthesized using chemical precipitation method. *J. Mater. Sci. Mater. Electron.* **2017,** *28* (8), 6226-6232.

142. Kaur, P.; Kumar, S.; Chen, C.-L.; Yang, K.-S.; Wei, D.-H.; Dong, C.-L.; Srivastava, C.; Rao, S. M., Gd doping induced weak ferromagnetic ordering in ZnS nanoparticles synthesized by low temperature co-precipitation technique. *Mater. Chem. Phys.* **2017,** *186*, 124-130.

143. Sabaghi, V.; Davar, F.; Fereshteh, Z., ZnS nanoparticles prepared via simple reflux and hydrothermal method: Optical and photocatalytic properties. *Ceram Int* **2018,** *44* (7), 7545-7556.

144. Zhao, Y.; Zhang, Y.; Zhu, H.; Hadjipanayis, G. C.; Xiao, J. Q., Low-Temperature Synthesis of Hexagonal (Wurtzite) ZnS Nanocrystals. *J. Am. Chem. Soc.* **2004,** *126* (22), 6874-6875.

145. Li, Z.; Kong, L.; Sun, H.; Huang, S.; Li, L., Effect of the Electronic Structure on the Stability of CdSe/CdS and CdSe/CdS/ZnS Quantum-Dot Phosphors Incorporated into a Silica/Alumina Monolith. *ACS Appl Nano Mater.* **2018,** *1* (7), 3086-3090.

146. Cai, Z.; Liu, B.; Zou, X.; Cheng, H.-M., Chemical Vapor Deposition Growth and Applications of Two-Dimensional Materials and Their Heterostructures. *Chem. Rev.* **2018,** *118* (13), 6091-6133.

147. Zhai, X.; Zhang, X.; Chen, S.; Yang, W.; Gong, Z., Oleylamine as solvent and stabilizer to synthesize shape-controlled ZnS nanocrystals with good optical properties. *Colloids Surf. A* **2012,** *409*, 126-129.

148. Joo, J.; Na, H. B.; Yu, T.; Yu, J. H.; Kim, Y. W.; Wu, F.; Zhang, J. Z.; Hyeon, T., Generalized and Facile Synthesis of Semiconducting Metal Sulfide Nanocrystals. *J. Am. Chem. Soc.* **2003,** *125* (36), 11100-11105.

149. Liu, J.; Meyns, M.; Zhang, T.; Arbiol, J.; Cabot, A.; Shavel, A., Triphenyl Phosphite as the Phosphorus Source for the Scalable and Cost-Effective Production of Transition Metal Phosphides. *Chem. Mater.* **2018,** *30* (5), 1799-1807.

150. Beddoe, S. V. F.; Cosham, S. D.; Kulak, A. N.; Jupp, A. R.; Goicoechea, J. M.; Hyett, G., Phosphinecarboxamide as an unexpected phosphorus precursor in the chemical vapour deposition of zinc phosphide thin films. *Dalton Trans.* **2018,** *47* (28), 9221-9225.

151. Vance, C. C.; Vaddiraju, S.; Karthikeyan, R., Water disinfection using zinc phosphide nanowires under visible light conditions. *J Environ Chem Eng* **2018,** *6* (1), 568-573.

152. Katsube, R.; Kazumi, K.; Tadokoro, T.; Nose, Y., Reactive Epitaxial Formation of a Mg–P–Zn Ternary Semiconductor in Mg/Zn3P2 Solar Cells. *ACS Appl. Mater. Interfaces* **2018,** *10* (42), 36102-36107.

153. Green, M.; O'Brien, P., *A novel metalorganic route for the direct and rapid synthesis of monodispersed quantum dots of indium phosphide*. 1998; Vol. 22, p 2459-2460.

154. Luber, E. J.; Mobarok, M. H.; Buriak, J. M., Solution-Processed Zinc Phosphide (α-Zn3P2) Colloidal Semiconducting Nanocrystals for Thin Film Photovoltaic Applications. *ACS Nano* **2013,** *7* (9), 8136-8146.

155. Mobarok, M. H.; Luber, E. J.; Bernard, G. M.; Peng, L.; Wasylishen, R. E.; Buriak, J. M., Phase-Pure Crystalline Zinc Phosphide Nanoparticles: Synthetic Approaches and Characterization. *Chemi. Mater.* **2014,** *26* (5), 1925-1935.

156. Brec, R., Review on structural and chemical properties of transition metal phosphorous trisulfides MPS3. *Solid State Ionics* **1986,** *22* (1), 3-30.

157. Prouzet, E.; Ouvrard, G.; Brec, R., Structure determination of $ZnPS_3$. *Mater. Res. Bull.* **1986,** *21* (2), 195-200.

158. Foot, P. J. S.; Nevett, B. A., Properties of NiPS3 and ZnPS3 prepared at ambient temperature. *J. Chem. Soc., Chem. Commun.* **1987,** (5), 380-381.

159. Mayorga-Martinez, C. C.; Sofer, Z.; Sedmidubský, D.; Huber, Š.; Eng, A. Y. S.; Pumera, M., Layered Metal Thiophosphite Materials: Magnetic, Electrochemical, and Electronic Properties. *ACS Appl. Mater. Interfaces* **2017,** *9* (14), 12563-12573.

160. Davis, R. E.; Nakshbendi, H. F., Sulfur in Amine Solvents. *J. Am. Chem. Soc.* **1962,** *84* (11), 2085-2090.

161. Thomson, J. W.; Nagashima, K.; Macdonald, P. M.; Ozin, G. A., From Sulfur−Amine Solutions to Metal Sulfide Nanocrystals: Peering into the Oleylamine−Sulfur Black Box. *J. Am. Chem. Soc.* **2011,** *133* (13), 5036-5041.

162. Ketchum, D. R.; Schimek, G. L.; Pennington, W. T.; Kolis, J. W., Synthesis of new Group III fluoride–ammonia adducts in supercritical ammonia: structures of $AlF_3(NH_3)_2$ and $InF_2(NH_2)(NH_3)$. *Inorganica Chimica Acta* **1999,** *294* (2), 200-206.

163. Mourdikoudis, S.; Liz-Marzán, L. M., Oleylamine in Nanoparticle Synthesis. *Chem. Mater.* **2013,** *25* (9), 1465-1476.

164. Sharma, S. N.; Sharma, H.; Singh, G.; Shivaprasad, S. M., Studies of interaction of amines with TOPO/TOP capped CdSe quantum dots: Role of crystallite size and oxidation potential. *Mater. Chem. Phys.* **2008,** *110* (2), 471-480.

165. Sharma, S. N.; Vats, T.; Dhenadhayalan, N.; Ramamurthy, P.; Narula, A. K., Ligand-dependent transient absorption studies of hybrid polymer:CdSe quantum dot composites. *Sol. Energy Mater. Sol. Cells* **2012,** *100*, 6-15.

166. Moon, H. R.; Urban, J. J.; Milliron, D. J., Size-Controlled Synthesis and Optical Properties of Monodisperse Colloidal Magnesium Oxide Nanocrystals. *Angew. Chem. Int. Ed.* **2009,** *121* (34), 6396-6399.

167. Bojar, H.-P.; Walter, F.; Baumgartner, J.; Färber, G., AMMINEITE, CuCl2(NH3)2, A NEW SPECIES CONTAINING AN AMMINE COMPLEX: MINERAL DATA AND CRYSTAL STRUCTURE. *Can. Mineral.* **2010,** *48* (6), 1359-1371.

168. Priyadarshini, E.; Pradhan, N., Gold nanoparticles as efficient sensors in colorimetric detection of toxic metal ions: A review. *Ensor. Actuat. B Chem.* **2017,** *238*, 888-902.

169. Mayer, K. M.; Lee, S.; Liao, H.; Rostro, B. C.; Fuentes, A.; Scully, P. T.; Nehl, C. L.; Hafner, J. H., A Label-Free Immunoassay Based Upon Localized Surface Plasmon Resonance of Gold Nanorods. *ACS Nano* **2008,** *2* (4), 687-692.

170. Zijlstra, P.; Paulo, P. M. R.; Orrit, M., Optical detection of single non-absorbing molecules using the surface plasmon resonance of a gold nanorod. *Nat. Nanotechnol.* **2012,** *7*, 379.

171. Elim, H. I.; Yang, J.; Lee, J.-Y.; Mi, J.; Ji, W., Observation of saturable and reverse-saturable absorption at longitudinal surface plasmon resonance in gold nanorods. *Appl. Phys. Lett.* **2006,** *88* (8), 083107.

172. Niidome, T.; Yamagata, M.; Okamoto, Y.; Akiyama, Y.; Takahashi, H.; Kawano, T.; Katayama, Y.; Niidome, Y., PEG-modified gold nanorods with a stealth character for in vivo applications. *J. Control. Release* **2006,** *114* (3), 343-347.

173. Huang, X.; Neretina, S.; El-Sayed, M. A., Gold Nanorods: From Synthesis and Properties to Biological and Biomedical Applications. *Adv. Mater.* **2009,** *21* (48), 4880-4910.

174. Wiesner, J.; Wokaun, A., Anisometric gold colloids. Preparation, characterization, and optical properties. *Chem. Phys. Lett.* **1989,** *157* (6), 569-575.

175. Jana, N. R.; Gearheart, L.; Murphy, C. J., Wet Chemical Synthesis of High Aspect Ratio Cylindrical Gold Nanorods. *J. Nanopart. Res.* **2001,** *105* (19), 4065-4067.

176. Murphy, C. J.; Thompson, L. B.; Chernak, D. J.; Yang, J. A.; Sivapalan, S. T.; Boulos, S. P.; Huang, J.; Alkilany, A. M.; Sisco, P. N., Gold nanorod crystal growth: From seed-mediated synthesis to nanoscale sculpting. *Curr. Opin. Colloid Interface Sci.* **2011,** *16* (2), 128-134.

177. Grzelczak, M.; Pérez-Juste, J.; Mulvaney, P.; Liz-Marzán, L. M., Shape control in gold nanoparticle synthesis. *Chem. Soc. Rev.* **2008,** *37* (9), 1783-1791.

178. Alkilany, A. M.; Nagaria, P. K.; Hexel, C. R.; Shaw, T. J.; Murphy, C. J.; Wyatt, M. D., Cellular Uptake and Cytotoxicity of Gold Nanorods: Molecular Origin of Cytotoxicity and Surface Effects. *Small* **2009,** *5* (6), 701-708.

179. Warner, M. G.; Reed, S. M.; Hutchison, J. E., Small, Water-Soluble, Ligand-Stabilized Gold Nanoparticles Synthesized by Interfacial Ligand Exchange Reactions. *Chem. Mater.* **2000,** *12* (11), 3316-3320.

180. Jadzinsky, P. D.; Calero, G.; Ackerson, C. J.; Bushnell, D. A.; Kornberg, R. D., Structure of a Thiol Monolayer-Protected Gold Nanoparticle at 1.1 Å Resolution. *Science* **2007,** *318* (5849), 430.

181. Bhargava, A. K.; Banerjee, M. K., 2.2 Hardenability of Steel. In *Comprehensive Materials Finishing*, Hashmi, M. S. J., Ed. Elsevier: Oxford, 2017; pp 50-70.

182. Gregson, P. J., Aluminium alloys: physical metallurgy, processing and properties. In *High Performance Materials in Aerospace*, Flower, H. M., Ed. Springer Netherlands: Dordrecht, 1995; pp 49-84.

183. Frazier, W. E.; Lee, E. W.; Donnellan, M. E.; Thompson, J. J., Advanced lightweight alloys for aerospace applications. *JOM* **1989,** *41* (5), 22-26.

184. 6 - Production and casting of aerospace metals. In *Introduction to Aerospace Materials*, Mouritz, A. P., Ed. Woodhead Publishing: 2012; pp 128-153.

185. Zhang, R. F.; Kong, X. F.; Wang, H. T.; Zhang, S. H.; Legut, D.; Sheng, S. H.; Srinivasan, S.; Rajan, K.; Germann, T. C., An informatics guided classification of miscible and immiscible binary alloy systems. *Sci. Rep.* **2017,** *7* (1), 9577.

186. Kusada, K.; Kobayashi, H.; Ikeda, R.; Kubota, Y.; Takata, M.; Toh, S.; Yamamoto, T.; Matsumura, S.; Sumi, N.; Sato, K.; Nagaoka, K.; Kitagawa, H., Solid Solution Alloy Nanoparticles of Immiscible Pd and Ru Elements Neighboring on Rh: Changeover of the Thermodynamic Behavior for Hydrogen Storage and Enhanced CO-Oxidizing Ability. *J. Am. Chem. Soc.* **2014,** *136* (5), 1864-1871.

187. Ma, Q.; Zhan, Y.; Hong, W., Tunable Metamaterial with Gold and Graphene Split-Ring Resonators and Plasmonically Induced Transparency. *Nanomater.* **2018,** *9* (1), 7.

188. Byers, C. P.; Zhang, H.; Swearer, D. F.; Yorulmaz, M.; Hoener, B. S.; Huang, D.; Hoggard, A.; Chang, W.-S.; Mulvaney, P.; Ringe, E.; Halas, N. J.; Nordlander, P.; Link, S.; Landes, C. F., From tunable core-shell nanoparticles to plasmonic drawbridges: Active control of nanoparticle optical properties. *Sci. Adv* **2015,** *1* (11), e1500988.

189. Gamler, J. T. L.; Ashberry, H. M.; Skrabalak, S. E.; Koczkur, K. M., Random Alloyed versus Intermetallic Nanoparticles: A Comparison of Electrocatalytic Performance. *Adv. Mater.* **2018,** *30* (40), 1801563.

190. Ferrando, R.; Jellinek, J.; Johnston, R. L., Nanoalloys: From Theory to Applications of Alloy Clusters and Nanoparticles. *Chem. Rev.* **2008,** *108* (3), 845-910.

191. Furukawa, S.; Komatsu, T., Intermetallic Compounds: Promising Inorganic Materials for Well-Structured and Electronically Modified Reaction Environments for Efficient Catalysis. *ACS Cat.* **2017,** *7* (1), 735-765.

192. Dehghan Banadaki, A.; Kajbafvala, A., Recent Advances in Facile Synthesis of Bimetallic Nanostructures: An Overview. *J Nanomater.* **2014,** *2014*, 28.

193. Thota, S.; Wang, Y.; Zhao, J., Colloidal Au–Cu alloy nanoparticles: synthesis, optical properties and applications. *Mater. Chem. Front* **2018,** *2* (6), 1074-1089.

194. Sra, A. K.; Schaak, R. E., Synthesis of Atomically Ordered AuCu and AuCu3 Nanocrystals from Bimetallic Nanoparticle Precursors. *J. Am. Chem. Soc.* **2004,** *126* (21), 6667-6672.

195. Zhang, D.; Diao, P.; Zhang, Q., Potential-Induced Shape Evolution of Gold Nanoparticles Prepared on ITO Substrate. *J Phys. Chem. C.* **2009,** *113* (36), 15796-15800.

196. Wang, Y.; Laborda, E.; Salter, C.; Crossley, A.; Compton, R. G., Facile *in situ* characterization of gold nanoparticles on electrode surfaces by electrochemical techniques: average size, number density and morphology determination. *Analyst* **2012,** *137* (20), 4693-4697.

197. Vasquez, Y.; Luo, Z.; Schaak, R. E., Low-Temperature Solution Synthesis of the Non-Equilibrium Ordered Intermetallic Compounds Au_3Fe, Au_3Co, and Au_3Ni as Nanocrystals. *J. Am. Chem. Soc.* **2008,** *130* (36), 11866-11867

VITA

Yi-Wei Wang

Candidate for the Degree of

Doctor of Philosophy

Thesis: SOLUTION-BASED SYNTHETIC STRATEGIES, CHARACTERIZATIONS, AND APPLICATIONS OF NANOPARTICLES

Major Field: Chemistry

Biographical:

Education:

Completed the requirements for the Doctor of Philosophy in Chemistry at Oklahoma State University, Stillwater, Oklahoma in May 2019.

Completed the requirements for the Bachelor of Science in Chemistry at Sun Yat-sen University, Guangzhou, China in 2013.

Experience:

Graduate Research/ Teaching Assistant (Year 2013- 2019)
Oklahoma State University, Stillwater, Oklahoma, USA.

Research Intern **(**Year 2011- 2013)
Physical Chemistry Research Institution, Sun Yat-sen University, China.